UNITED NATIONS EDUCATIONAL, SCIENTIFIC AND CULTURAL ORGANIZATION
INTERNATIONAL ATOMIC ENERGY AGENCY
INTERNATIONAL CENTRE FOR THEORETICAL PHYSICS
I.C.T.P., P.O. BOX 586, 34100 TRIESTE, ITALY, CABLE: CENTRATOM TRIESTE

H4.SMR/1013-35

SCHOOL ON THE USE OF SYNCHROTRON RADIATION
IN SCIENCE AND TECHNOLOGY:
"John Fuggle Memorial"

3 November - 5 December 1997

Miramare - Trieste, Italy

Small Angle X-ray Scattering (SAXS) by Heterogenous Materials

A. Craievich
Universidade de Sao Paulo
Sao Paulo, Brazil

III) Small Angle X-ray Scattering (SAXS) by heterogeneous materials

- Basic theory
- Guinier's Law. Porod's Law. Invariant
- Crystalization in glasses
- Aggregation and gelation (fractal structures)
- Phase-separation in glasses
- Application of anomalous scattering
- SAXS instrumentation

SAXS

General case:

$$A(\vec{q}) = A_e \int \rho(\vec{r})\, e^{-i\vec{q}\vec{r}}\, d\vec{r}$$

$$\rho(\vec{r}) = \int \frac{A(s)}{A_e}\, e^{i\vec{q}\vec{r}}\, d\vec{q}$$

$$I(\vec{s}) = |A(\vec{s})|^2 = A_e^2 \left| \int \rho(\vec{r})\, e^{-i\vec{q}\vec{r}}\, d\vec{r} \right|^2$$

$$(= AA^*)$$

$$I(\vec{q}) = \int\int \rho(\vec{u}')\, \rho(\vec{u})\, e^{-i\vec{q}(u'-u)}\, du'\, du$$

$$\vec{u}' - \vec{u} = \vec{r} \therefore \vec{u}' = \vec{u} + \vec{r}$$

$$I(\vec{q}) = \int\int \rho(u+\vec{r})\,\rho(\vec{u})\,e^{-i\vec{q}\vec{r}}\,d\vec{r}\,du$$

$$= \int \underbrace{\left[\int \rho(\vec{u}+\vec{r})\,\rho(\vec{u})\,d\vec{u}\right]}_{P(\vec{r})} e^{-i\vec{q}\vec{r}}\,dr$$

$$I(\vec{q}) = \int P(\vec{r})\,e^{-i\vec{q}\vec{r}}\,d\vec{r}$$

$$P(\vec{r}) = \int I(\vec{q})\,e^{i\vec{q}\vec{r}}\,d\vec{q}$$

Princípio de Babinet

$$A(q) = \int \rho(\vec{r})\,e^{-i\vec{q}\vec{r}}\,d\vec{r}$$

$$A(q) = \int \left[\rho_o + n(\vec{r})\right] e^{-i\vec{q}\vec{r}}\,d\vec{r}$$

$$= \int \underbrace{\rho_o\,e^{-i\vec{q}\vec{r}}\,d\vec{r}}_{\|\ 0} + \int n(\vec{r})\,e^{-i\vec{q}\vec{r}}\,d\vec{r}$$

$$I(\vec{q}) = \int \left[n(\vec{u})\,n(\vec{u}+\vec{r})\,d\vec{u}\right] e^{-i\vec{q}\vec{r}}\,d\vec{r}$$

For q -> 0

$$I(0) = v\,\overline{n^2}$$

Defining:

$$\gamma(\vec{r}) = \frac{1}{v\,\overline{n^2}} \int n(\vec{u})\, n(\vec{u}+\vec{r})\, d\vec{u}$$

$$\rightarrow I(\vec{q}) = \overline{n^2}\, v \int \gamma(\vec{r})\, e^{-i\vec{q}\vec{r}}\, d\vec{r}$$

For isotropic systems:

$$I(q) = \overline{n^2}\, v \int \gamma(r) \frac{\sin qr}{qr} 4\pi r^2\, dr$$

Assymptotic behaviors:

a) q -> 0 (Guinier's law)

$$I(q) = I(0)\, e^{-\frac{1}{3} R_G\, q^2}$$ (isotropic systems)

$$I(\vec{q}) = I(0)\, e^{-(\vec{q}.\vec{R}_D)^2}$$

$$R_D^2 = \frac{\int r_D^2\, \rho(\vec{r})\, d\vec{r}}{\int \rho(\vec{r})\, d\vec{r}}$$

b) q -> 0

$$I(0) = N\, n^2 = N(\rho - \rho_o)^2\, v^2$$

General case:

$$I(0) = n^2\, \overline{N} \frac{kT}{v} \beta\,; \beta = -\frac{1}{V}\left(\frac{\partial V}{dP}\right)_T$$

c) q -> 0 (Porod's law)

$$I(q) = 2\pi(n - n_o)^2 \frac{S}{q^4}$$ (leading term)

$$I(q) = \frac{A}{q^4} + \frac{B}{q^6} + \ldots +$$

(include oscillation contribution)

$$+ \frac{f_1(u_1 q)\cos u}{h^3} + \frac{f_2(u_1 q)\sin u}{h^3}\,;\, u = qR_1 \quad .$$

Integral parameters

$$\int q^2\, I(q)\, dq = 2\pi^2\ \ Nn^2\, v \qquad \text{(dilute system)}$$

$$\int q^2\, I(q)\, dq = 2\pi^2\, n^2 V\, c(1-c)$$

c: volume fraction

V: irradiated volume

N: number of particles per unit volume

υ: particle volume

$$\ell_c = \frac{2}{4\pi\, V\, n^2\, c(1-c)} \int_o^\infty q\, I(q)\, dq$$

Dense system of identical particles:

I(h) = ϕ P(q) S(q)

$$A(\vec{q}) = \sum_k \left[\sum_\ell f_{k\ell}\, e^{-iq(\vec{R}_k + \vec{r}_{k\ell})} \right]$$

For particles with center of simmetry:

$$A(\vec{q}) = \sum_k e^{-i\vec{q}\vec{r}} \sum_\ell f_{k\ell} \cos(\vec{q}\vec{r}_{k\ell})$$

$$I(q) = \Phi\, P(q)\, S(q)$$

$$q = \frac{4\pi}{\lambda} \sin \varepsilon/2$$

$$P(q) = V^2(\rho - \rho_\circ)^2 \left[3\sin(qr_\circ) - qr_\circ \cos(qr_\circ) / (qr_\circ)^3\right]^2$$

$$P(q) = 2\pi(\rho - \rho_\circ)\, S / q^4$$

$$q \to \infty$$

Guinier: $$\frac{P = P(0)\, e^{-R_G^2 q^2/3}}{q \to 0}$$

Porod: $$\frac{P = K\, S / q^4}{q \to \infty}$$

9. Rectangular function:

$$f(x) \begin{cases} = 1 & \text{for } |x| < a/2, \\ = 0 & \text{for } |x| > a/2. \end{cases}$$

$$F(s) = a \frac{\sin \pi a s}{\pi a s}.$$

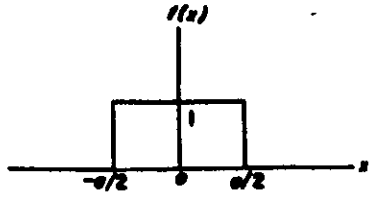

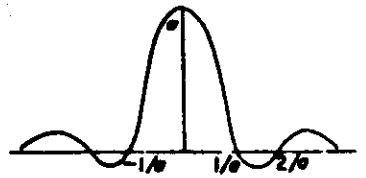

10. Triangular function:

$$f(x) \begin{cases} = a\left(1 - \frac{|x|}{a}\right) & \text{for } |x| < a, \\ = 0 & \text{for } |x| > a. \end{cases}$$

$$F(s) = a^2 \frac{\sin^2 \pi a s}{(\pi a s)^2}$$

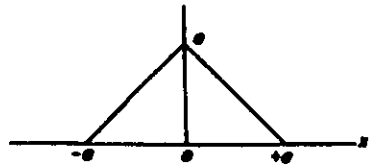

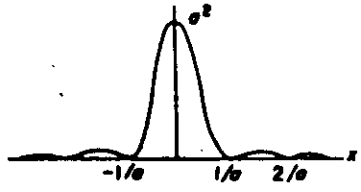

11. Exponential function:

$$f(x) = \exp(-\gamma |x|)$$

$$F(s) = \frac{2\gamma}{\gamma^2 + (2\pi s)^2}$$ (Cauchy function)

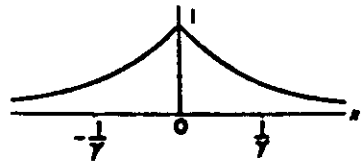

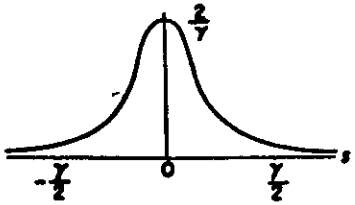

12. Form factor of a sphere:

$$f(x) \begin{cases} = 1 & \text{for } |x| < R, \\ = 0 & \text{for } |x| > R. \end{cases}$$

$F(s)$ has spherical symmetry

$$F(s) = \frac{4}{3}\pi R^3 \Phi(2\pi s R),$$

$$\text{with } \Phi(u) = 3\frac{(\sin u - u \cos u)}{u^3}$$

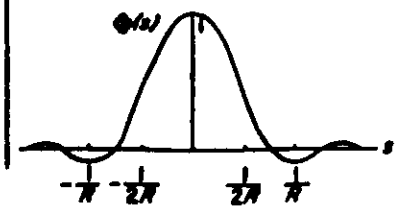

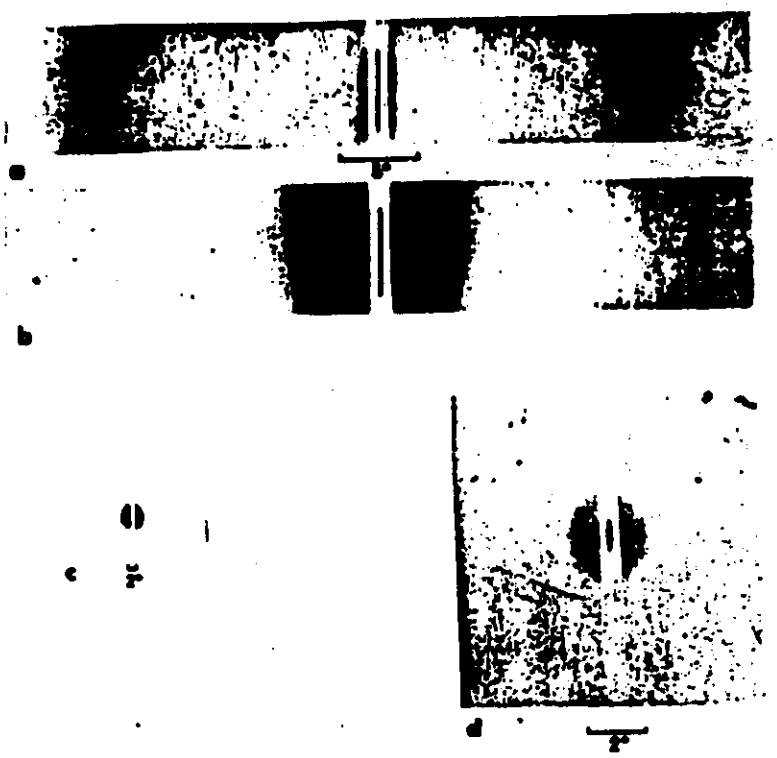

SAXS

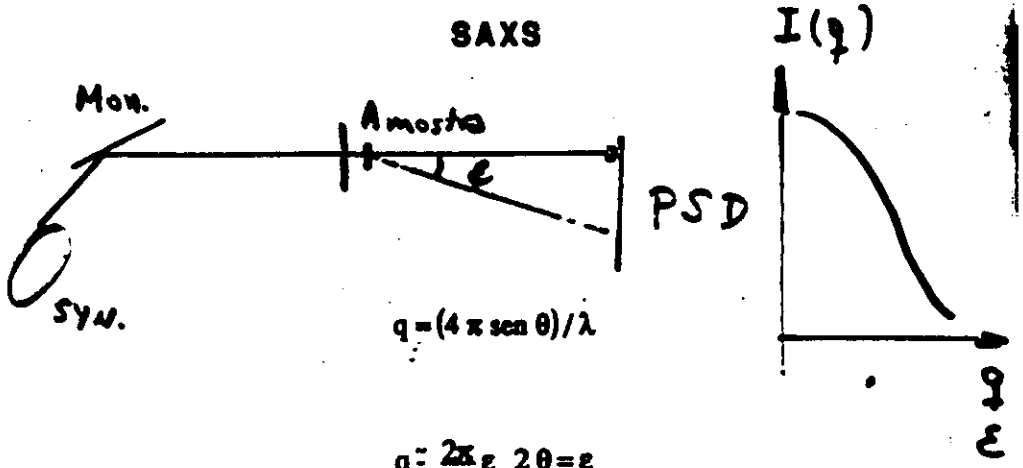

$$q = (4\pi \operatorname{sen}\theta)/\lambda$$

$$q \simeq \frac{2\pi}{\lambda}\varepsilon \quad 2\theta = \varepsilon$$

$$I(0) = (\rho_1 - \rho_2)^2 N v^2$$

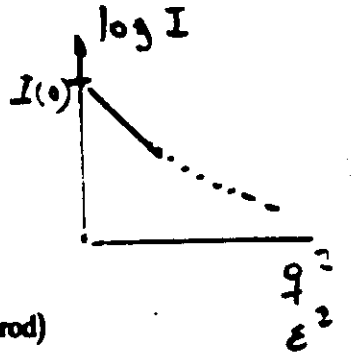

$$I(q) = I(0)\, e^{-\frac{1}{3}R_g^2 q^2} \quad \text{(Guinier)}$$

$$\lim Iq^4 = \alpha + \beta q^4 \quad (q \to \infty) \text{(Porod)}$$

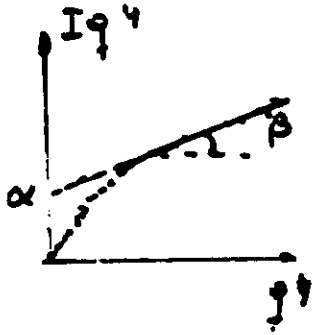

$$Q = \int_0^\infty I(q)\, q^2\, dq$$

$$Q = (\rho_1 - \rho_2)^2 N v$$

Diagram of the small-angle X-ray scattering installation at L.U.R.E.

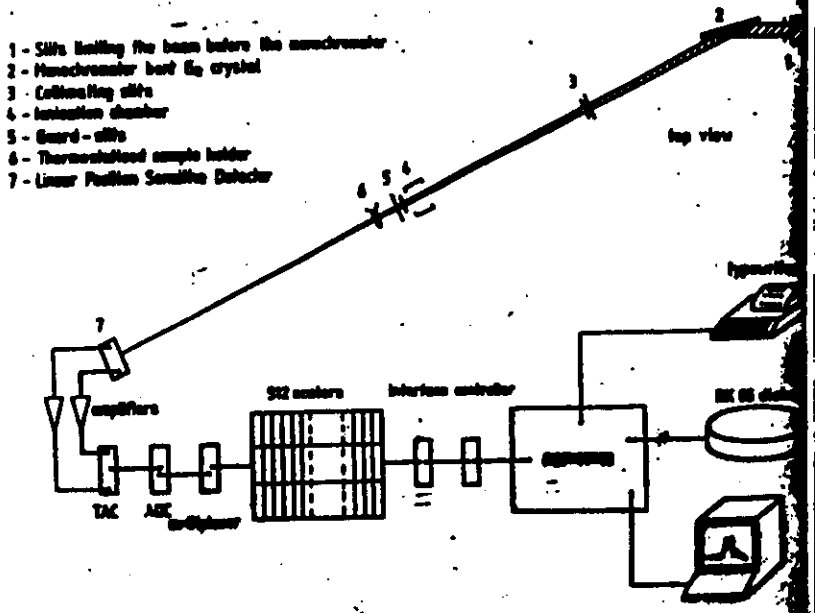

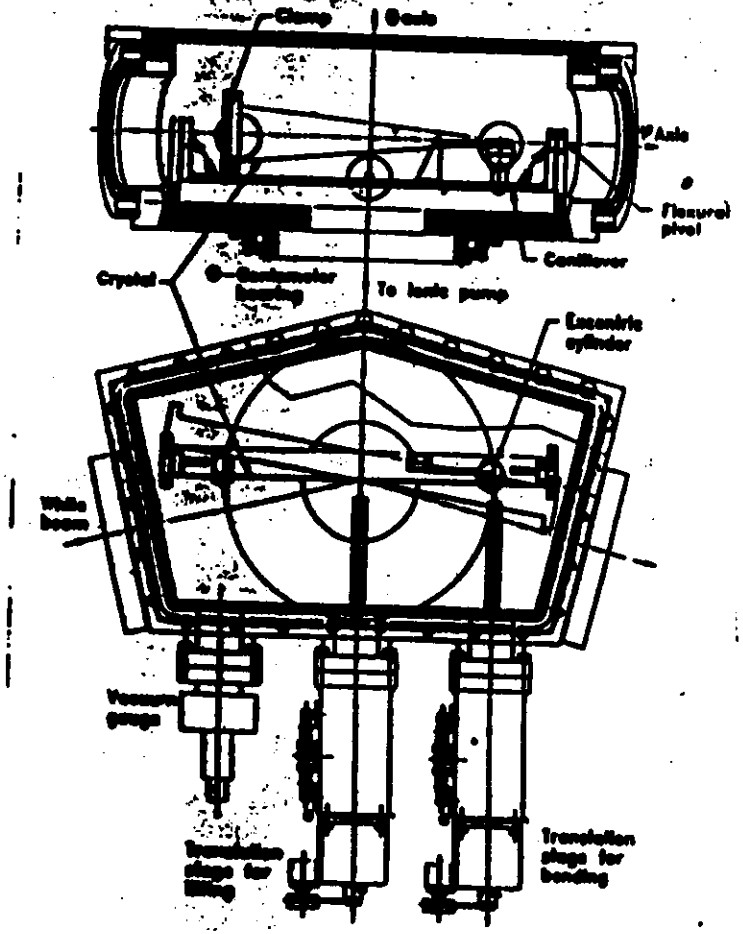

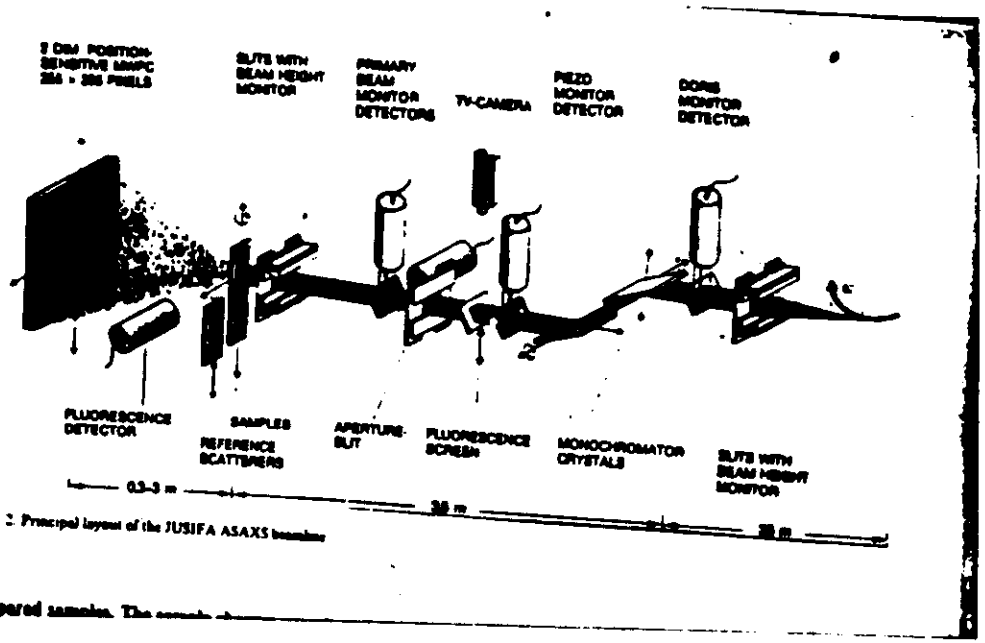

Fig. 2. Principal layout of the JUSIFA ASAXS beamline

prepared samples. The

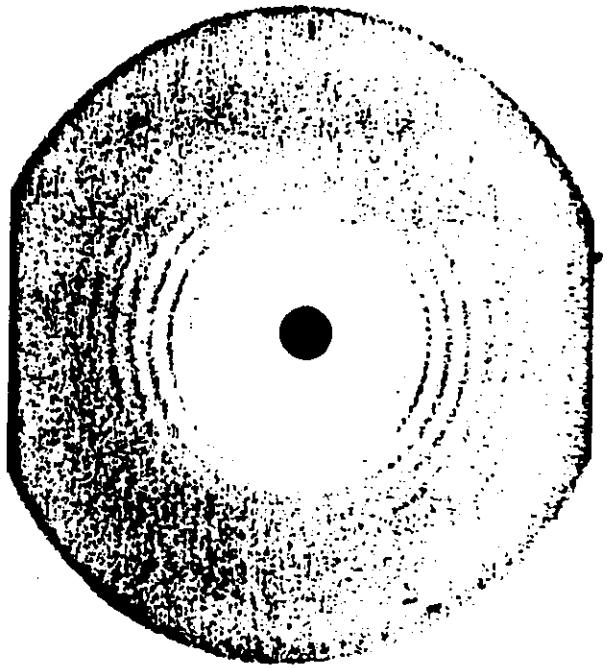

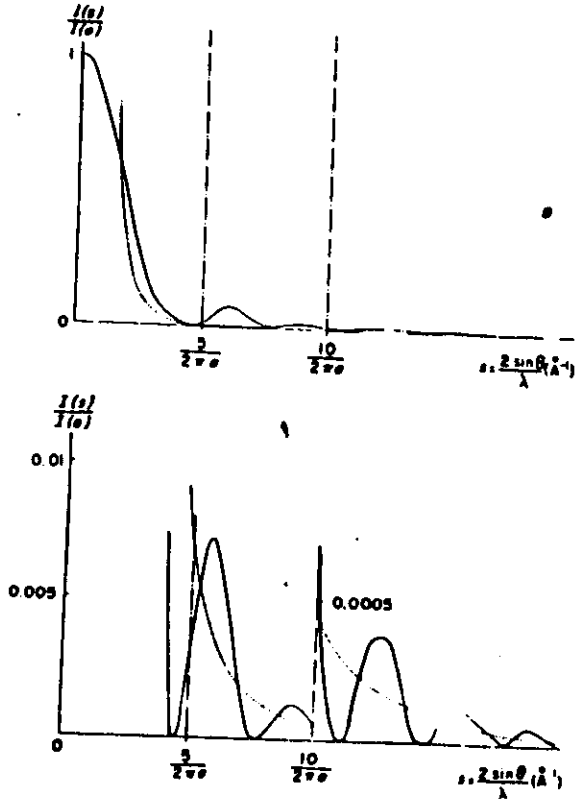

maxima clearly defined. In figure 2 these maxima seemed to be present but they could hardly be defined. A typical 100 second scan is shown in figure 3-A, where it is being compared with the average of four 200 second scans (curve B) in order to evaluate possible radiation damage to the protein.

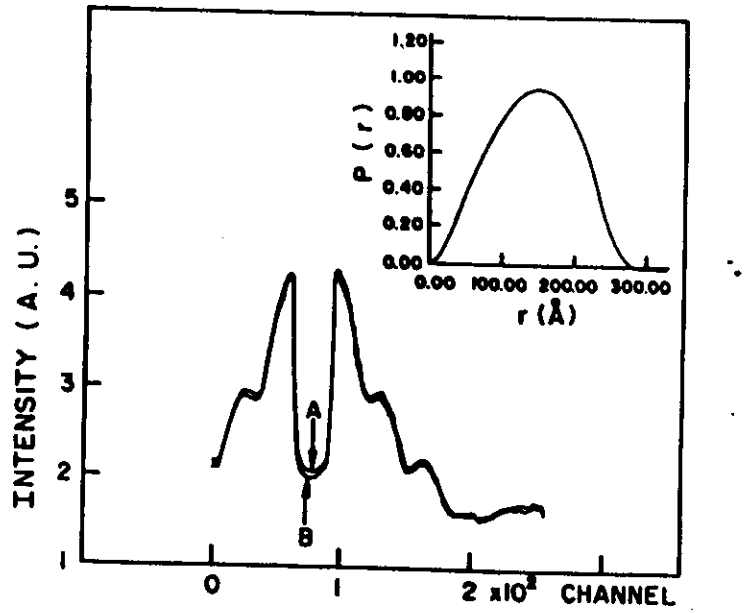

Figure 3. Experimental X-ray scattering curves from G.paulistus erythrocruorin obtained with synchrotron radiation. (A) One 100 second scan. (B) Average of four 200 second scans. The loss of intensity seems to be due to radiation damage suffered by the protein. Zero angle corresponds to channel 80, channel width = 0.000264 A^{-1}. The inset shows the distance distribution function calculated for a less concentrated sample (c/20).

Guinier plot calculations from the low concentration scattering curves (c/20 and c/40) resulted in values for the radius of giration in very good agreement with our previous calculations: 116 A. Data

FABRICATION

Melt (1350 °C, 40 min.) < Low melting point glass - (borosilicate)

Semiconductor elements.

fast cool down

AFTER MELTING

supersaturated solid solution ⇒ glass + semiconductor elements

NO QUANTUM DOTS

Heat treatment (500 - 600 °C)

Quantum dots development

Size controlled by temperature and time.

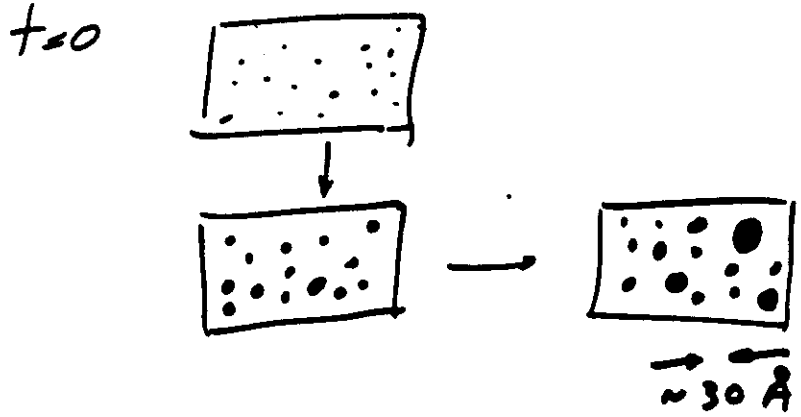

Sistema diluído de esferas com distribuição do tamanho

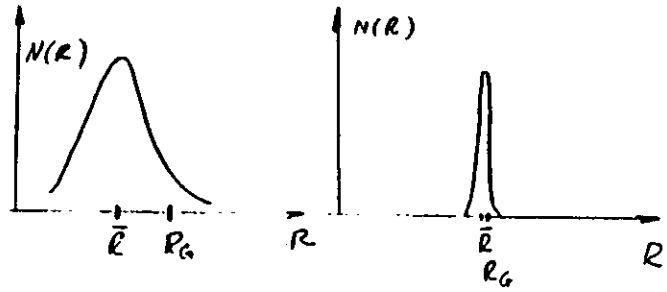

$$I(q) = \int_0^\infty N(R)\, R^6\, I_o(q,R)\, dR$$

$$\langle R^n \rangle = \int_0^\infty R^n\, N(R)\, dR$$

$$\left(\int_0^\infty N(R)\, dR = 1\right)$$

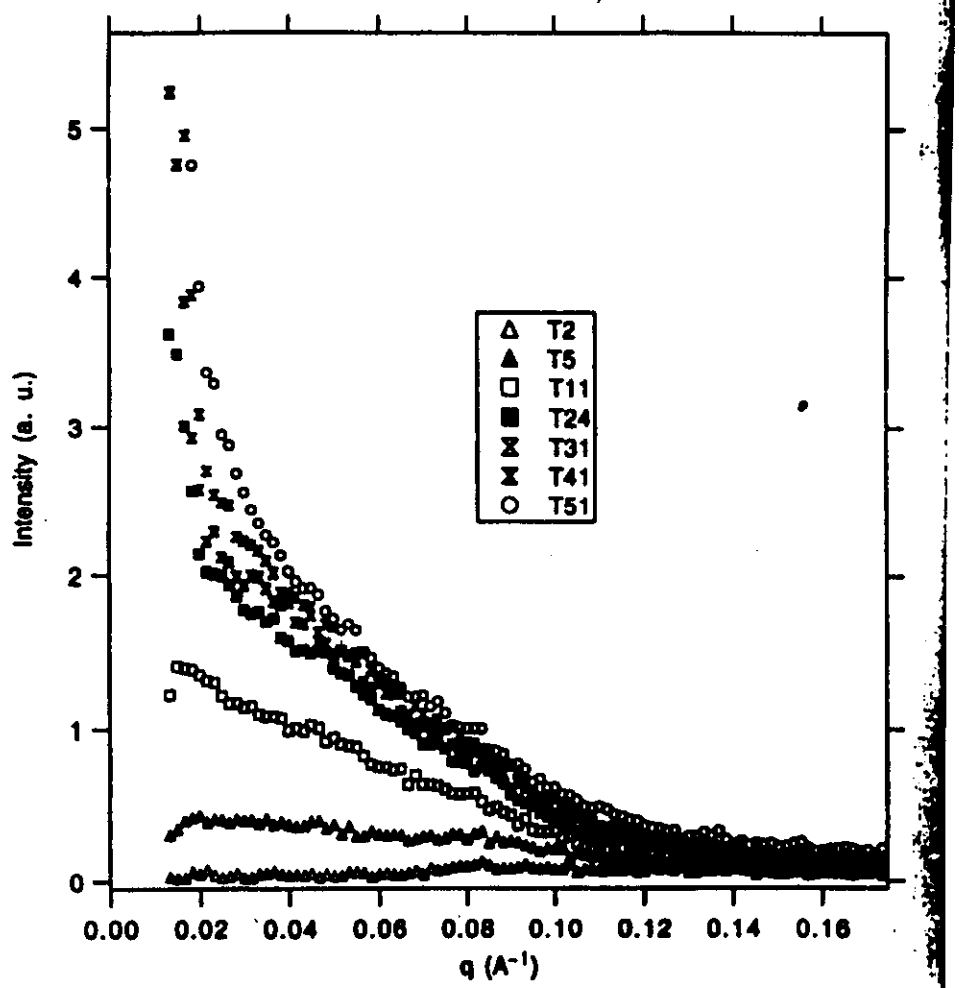

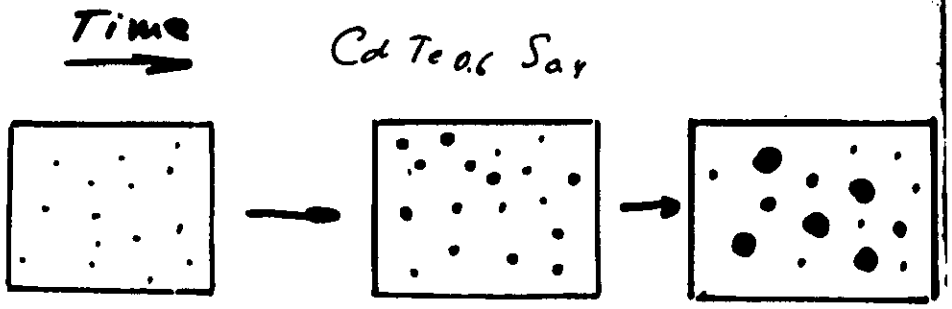

$R_g = (5/3)^{1/2} \langle R_G \rangle = [\langle R^6 \rangle / \langle R^6 \rangle]^{1/2}$

where $\langle R_G \rangle = 3^{1/2} \{ -\lim [d \ln I(q)/d(q^2)] (q \to 0) \}^{1/2}$ (Guinier law)

$R_v = (3/4\pi)^{1/3} \langle V \rangle^{1/3} = [\langle R^6 \rangle / \langle R^3 \rangle]^{1/3}$

where $\langle V \rangle = 2\pi^2 I(0) / Q$ and $Q = \int_0^\infty q^2 I(q)\, dq$

$R_p = (3/4) \langle D \rangle = \langle R^3 \rangle / \langle R^2 \rangle$

where $\langle D \rangle = (4/\pi) \int_0^\infty q^2 I(q)\, dq / K$ and

$K = \lim [I(q)\, q^4 (q \to \infty)]$ (Porod law)

$$N(R) = \frac{1}{R(2\mu)^{1/2} \ln\sigma} \exp\left[-\frac{(\ln R - \ln\mu)^2}{2\ln^2\sigma} \right]$$

$\ln R_i = \ln \mu + \ln^2\sigma\, k_i$; k_i ($i = p, v, g$) = R_p, R_v, R_g, respectively

$$\langle d \rangle = \frac{4}{\pi} \int_0^\infty q^2\, I(q)\, dq / K_P \; ; \qquad R_d = \frac{3}{4} \langle d \rangle = \langle R^3 \rangle / \langle R^2 \rangle$$

$$(K_P = \lim_{q \to \infty} I q^4)$$

$$\langle \ell \rangle = \pi \int_0^\infty q\, I(q)\, dq / \int_0^\infty q^2\, I(q)\, dq \; ; \qquad R_\ell = \frac{2}{3} \langle \ell \rangle = \langle R^4 \rangle / \langle R^3 \rangle$$

$$\langle \bar{S} \rangle = 2\pi \int_0^\infty I(q)\, dq / \int_0^\infty q^2\, I(q)\, dq \; ; \qquad R_I^2 = (5/4\pi) \langle \bar{S} \rangle = \langle R^5 \rangle / \langle R^3 \rangle$$

$$\langle v \rangle = 2\pi^2 I(o) / \int_0^\infty q^2\, I(q)\, dq \; ; \qquad R_v^3 = (3/4\pi) \langle v \rangle = \langle R^6 \rangle / \langle R^3 \rangle$$

$$\langle R_G \rangle = 3^{1/2} [- \lim d\,(\ln I(h)) / d(h^2)]^{1/2} \; ; \qquad R_g^2 = (5/3) \langle R_G \rangle^2 = \langle R^8 \rangle / \langle R^6 \rangle$$

G. Walter et al. J. Appl. Cryst. 18, 205 (1985).

$$N(R) = \frac{1}{R\,(2\pi)^{1/2}\,\ln\sigma} \cdot e^{-\frac{[(\ln R - \ln \mu)]^2}{2\ln^2 \sigma}}$$

$\ln R_i = \ln^2 \sigma \cdot k + \ln \mu$

k = 2,5 para i = d k = 3,5 para i = ℓ

k = 4,0 para i = f k = 4,5 para i = v

k = 7,0 para i = g

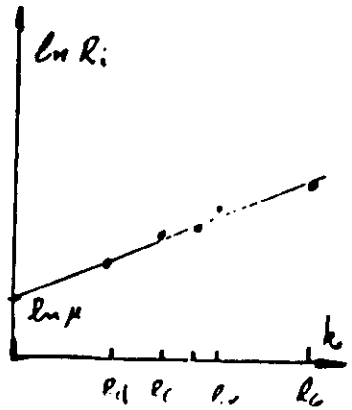

CdTe – Borosilicate glass

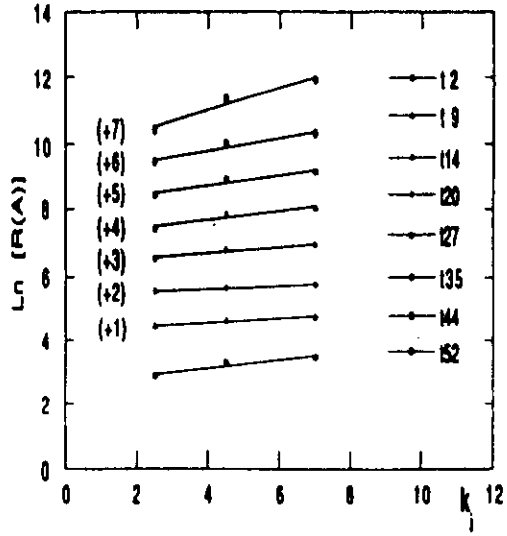

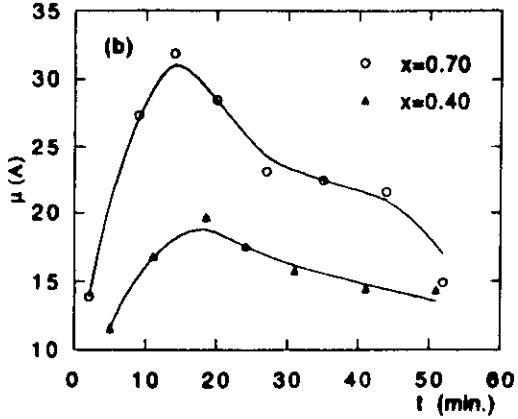

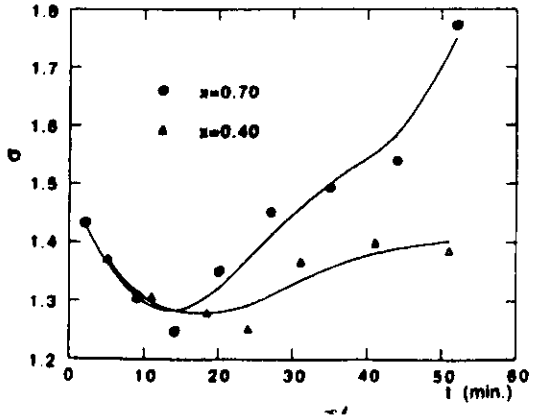

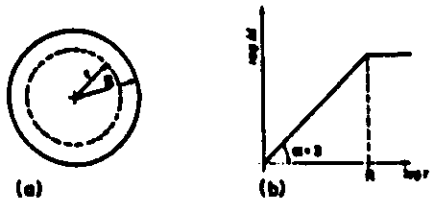

FIG. 4

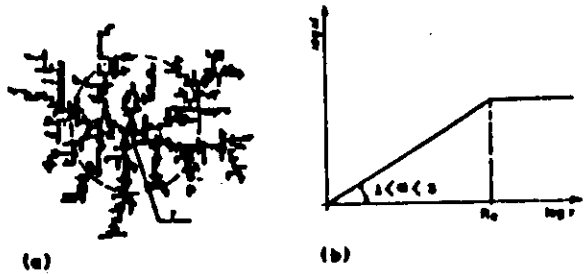

FIG. 5

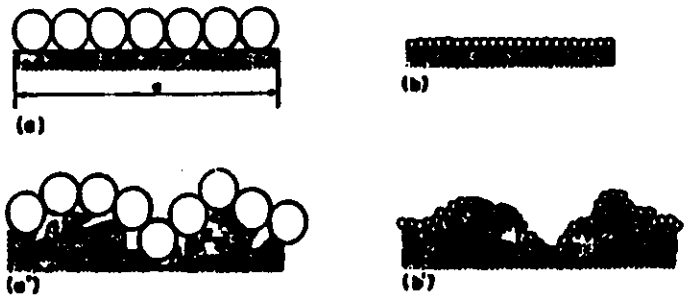

FIG. 6

$$N(r) = \phi \int g(r)\, 4\pi r^2\, dr$$

$$dN(r) = \phi\, g(1)\, 4\pi r^2\, dr$$

$$N(r) = \left(\frac{r}{r_0}\right)^D$$

$$\phi\, g(r) = (D/4\pi r_0)\, r^{D-3}$$

$$\phi\, g(r) = (D/4\pi r_0)\, r^{D-3} \cdot e^{-\frac{r}{\xi}}$$

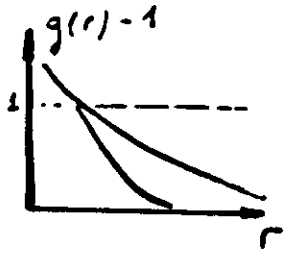

The introduction of the out-off function $e^{-\frac{r}{\xi}}$

avoids the divergence in the calculation of: $S(q)$

$$S(q) = 1 + 4\pi\phi \int [g(r) - 1]\, r^2\, \frac{\sin qr}{qr}\, dr$$

The calculation of S (q) leads to:

$$S(q) = 1 + \frac{1}{(q r_0)^D} \frac{D\Gamma(D-1)}{\left[1 + 1/(q^2 \xi^2)\right]^{(D-1)/2}} \times \sin\left[(D-1)\tan^{-1}(q\xi)\right]$$

$q \ll \xi^{-1}$ ⇓ $= P(D-1)(\xi / r_0)^D \times [1 - [D(D+1)/6] Q^2 \xi^2]$

$\xi^{-1} \ll q \ll r_0^{-1}$ ⇓ $\propto q^{-D}$

$q \gg r_0^{-1}$ ⇓ $\propto q^{-4}$ or $\propto q^{-(6 - D_s)}$

$I(q) = I(0) e^{-\frac{1}{3} R_g^2 q^2}$

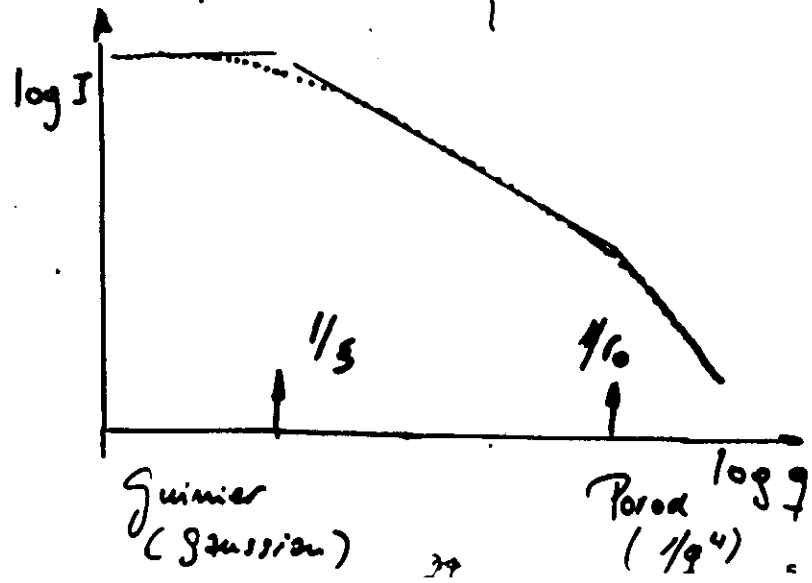

2.I

$\propto e^{-\frac{1}{3} R_G^2 q^2}$

$\propto \begin{cases} 1/q^{-D_v} \\ 1/q^{(6-D_s)} \end{cases}$

$\propto 1/q^4$

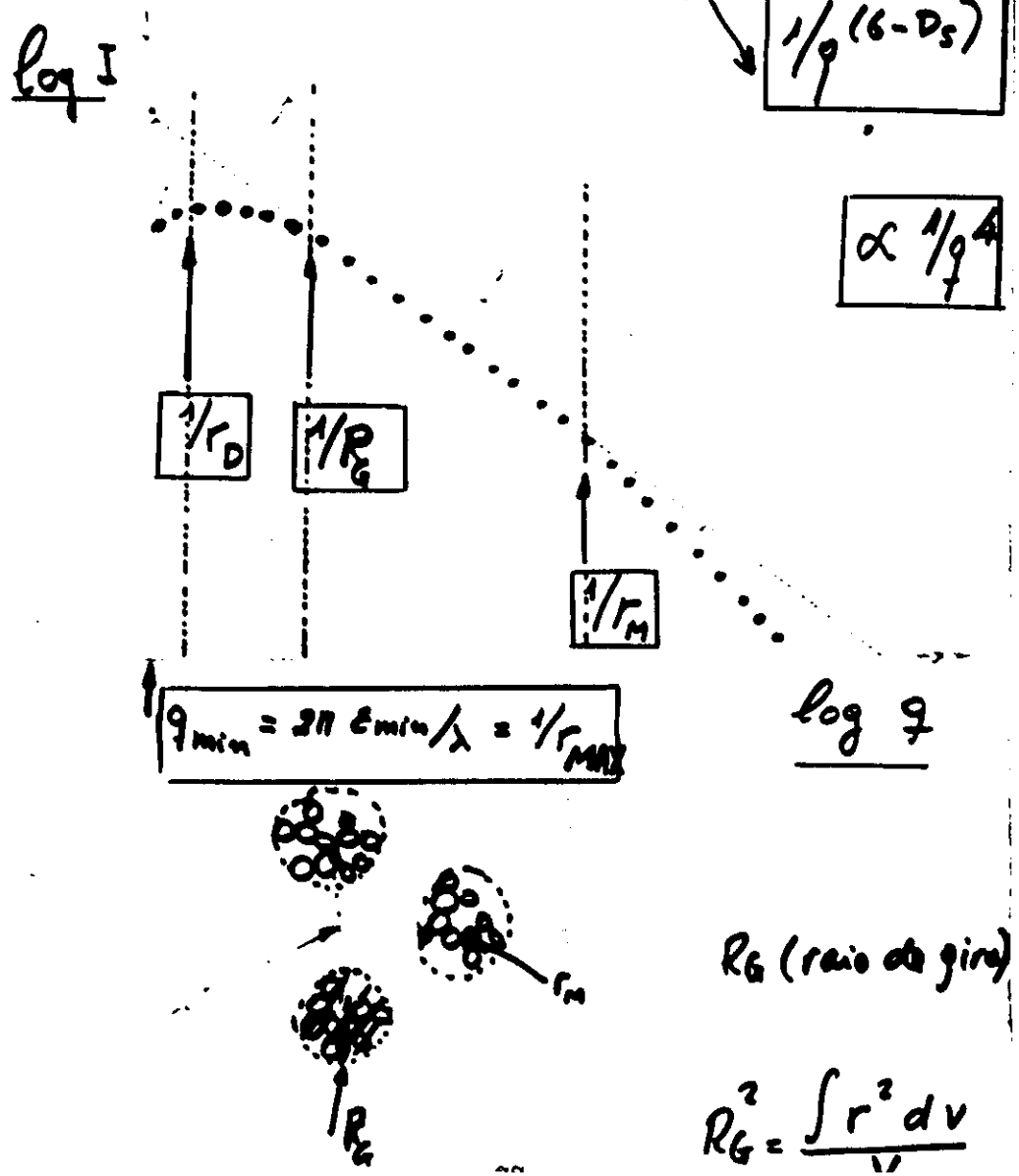

R_G (raio de giro)

$R_G^2 = \frac{\int r^2 dv}{V}$

STRUCTURAL STUDY OF FRACTAL SILICA HUMID GELS

L. CRAIEVICH

Laboratório Nacional de Luz Sincrotron, CNPq, Campinas, and Instituto de Física, Universidade de São Paulo, São Paulo, Brazil

D.I. dos SANTOS and M. AEGERTER

Instituto de Física e Química de São Carlos, Universidade de São Paulo, São Carlos, SP, Brazil

C. LOURS and J. ZARZYCKI

Laboratoire de Science des Matériaux Vitreux, Université du Languedoc, Montpellier, France

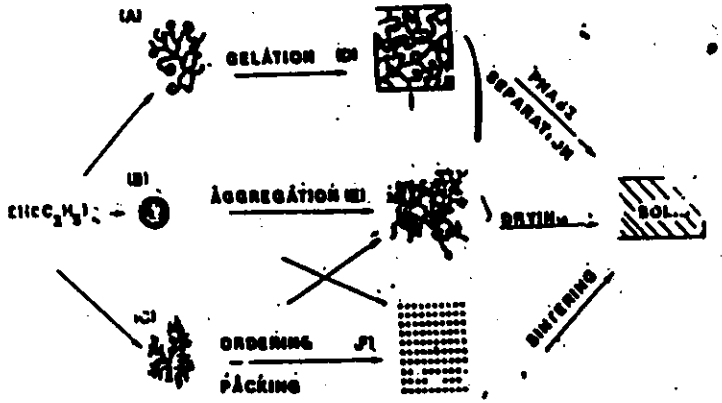

Fig. 1 Precursors to gels and ceramic materials

FIGURE 2
TEM microphotography of aerogel prepared from acidic sol.

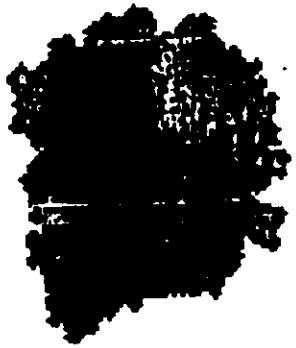

F.H.M. (Eden)

DF

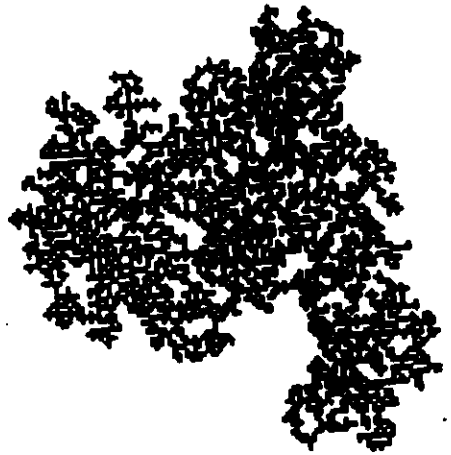

(2H+3H+FH) M

D = 1.8 F

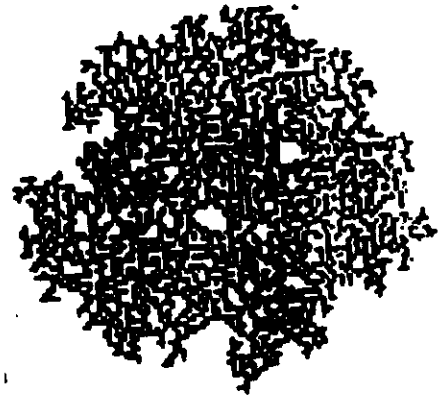

3H M

D = 2 NF

A. Craievich, V. Craievich, J. Zarzycki
LNLS, Brazil Univ. Montpellier

Aggregation kinetics and structure of precursor gels of zirconia under different preparation conditions

Introduction

Motivation

SAXS results

Conclusions

Sol-gel route to glasses

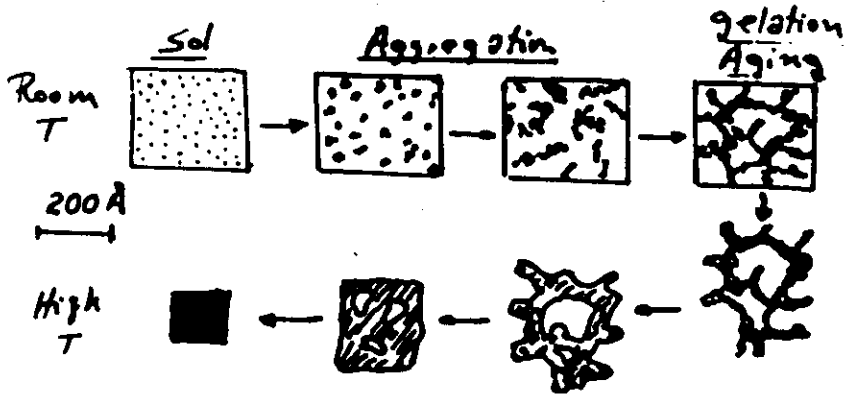

- TMOS + Methanol + water
- TEOS + Ethanol + water
- TMOS + water + ultrasound

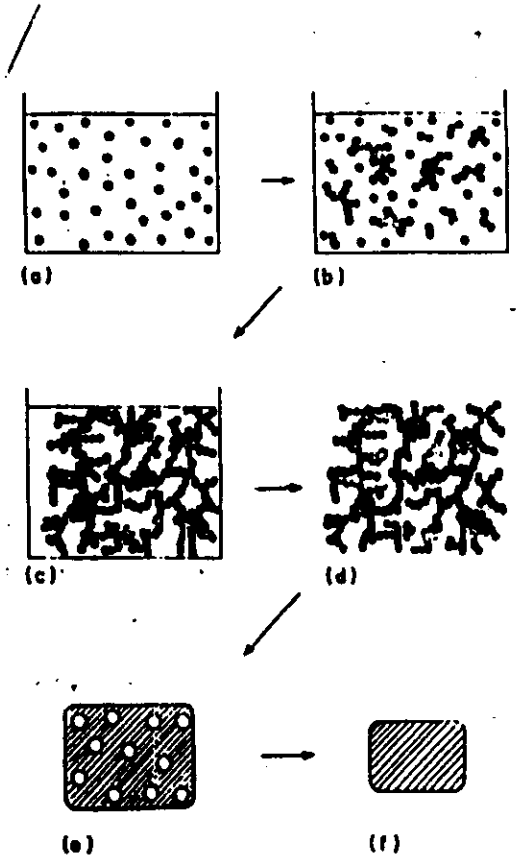

FIG. 11

Schaefer, Keefer 56, 2189 (1986)

TMOS + Metanol (Meio básico)

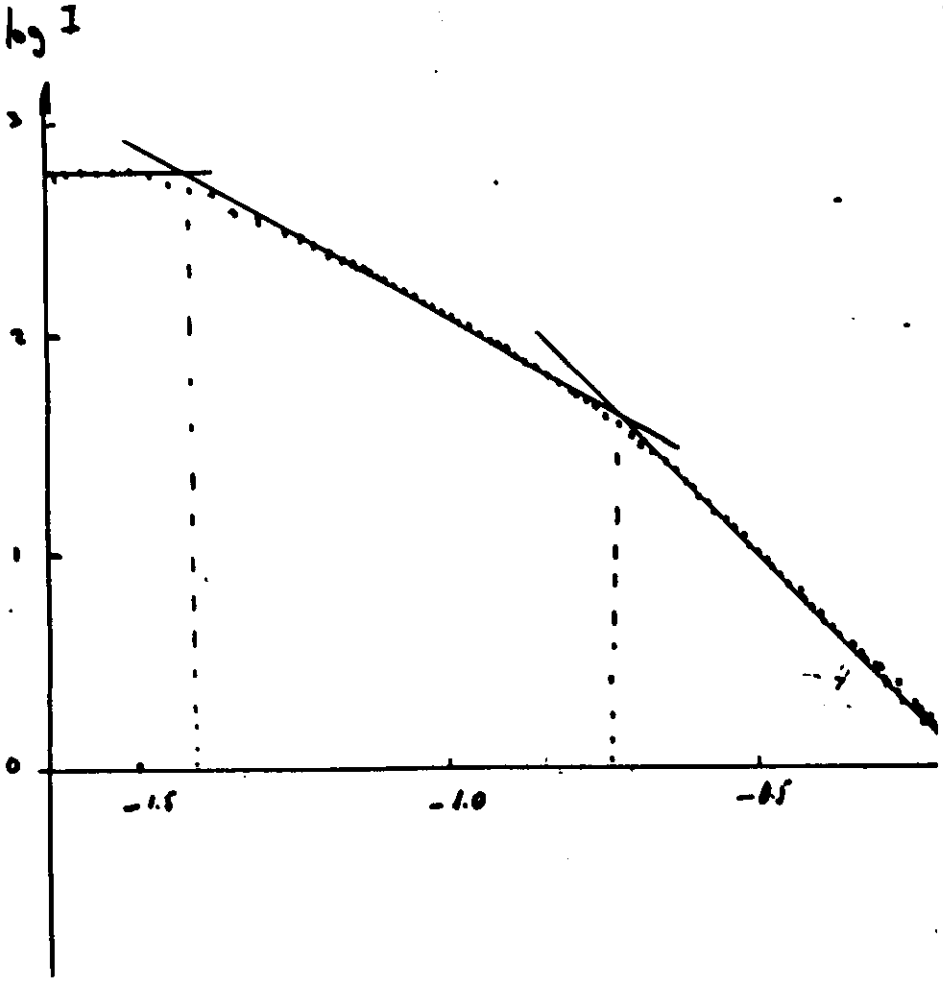

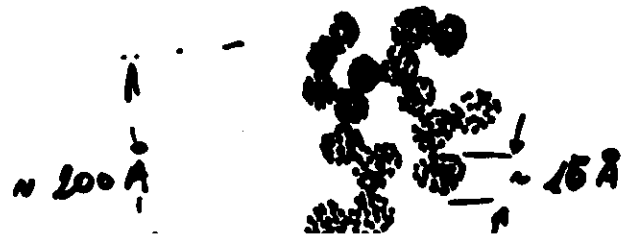

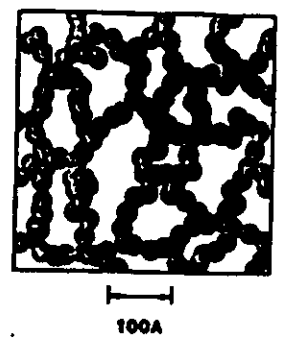

FIG. 2. Schematic diagram of the structure suggested for silica aerogel.

A : silica aerogel
B : agregate of silica particles
C : colloidal monomer

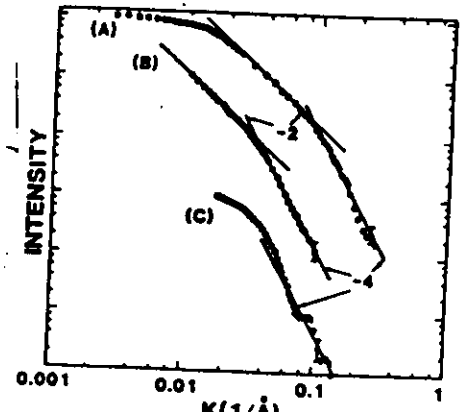

FIG. 1. Small-angle x-ray scattering curves for (curve A) silica aerogel ($\rho = 0.088$ g/cm^3), (curve B) a solution aggregate of silica particles (Ref. 12), and (curve C) the colloidal monomer. No crossover to K independence at small K is observed for the aggregate because of the large size (> 1 μm). The similarity of curves A and B indicates that the aerogel and the aggregate are structurally similar. More extensive light scattering data (Ref. 13) show a slope of -2.1 for the aggregate in the regime $K < 0.01$ Å^{-1}.

Chaumont, Craievich, Zarzycki
J. Non Cryst. Solids 1992

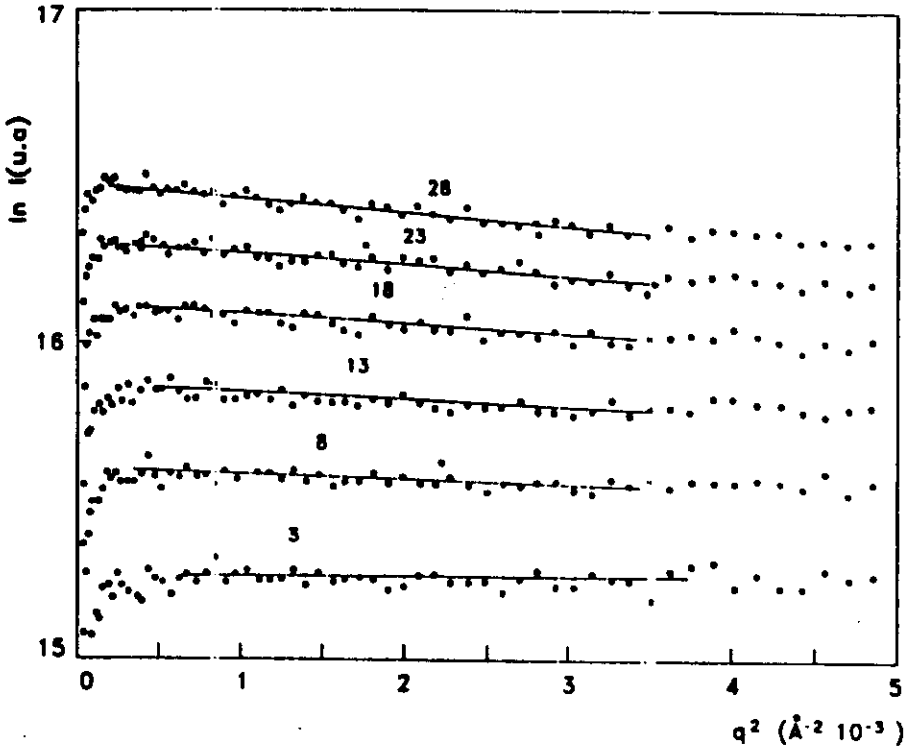

Fig. 1a: Guinier's plots corresponding to a sample solution 10 $Zr(O\,Pr)_4$ - 3 acetic acid without ultrasound for the indicated aggregation times (min.) a 60 °C (early stages of aggregation).

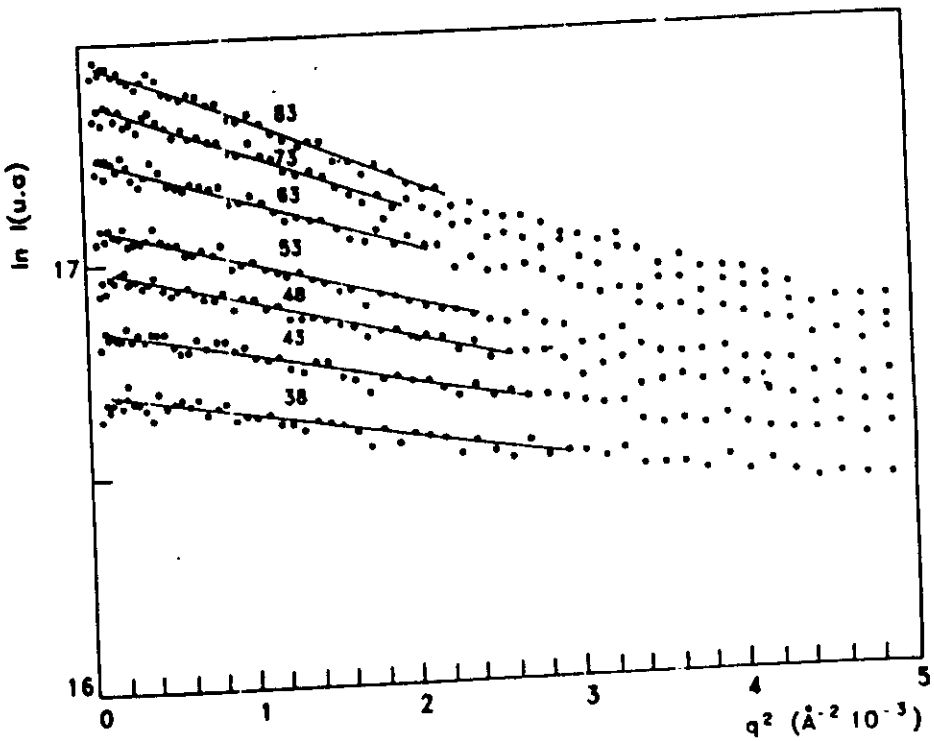

Fig. 1b: Guinier's plots corresponding to the same composition than in Fig. 1a for advanced stages of aggregation and gelation, as functions of the indicated aggregation times (min.).

Silica - TMOS sol

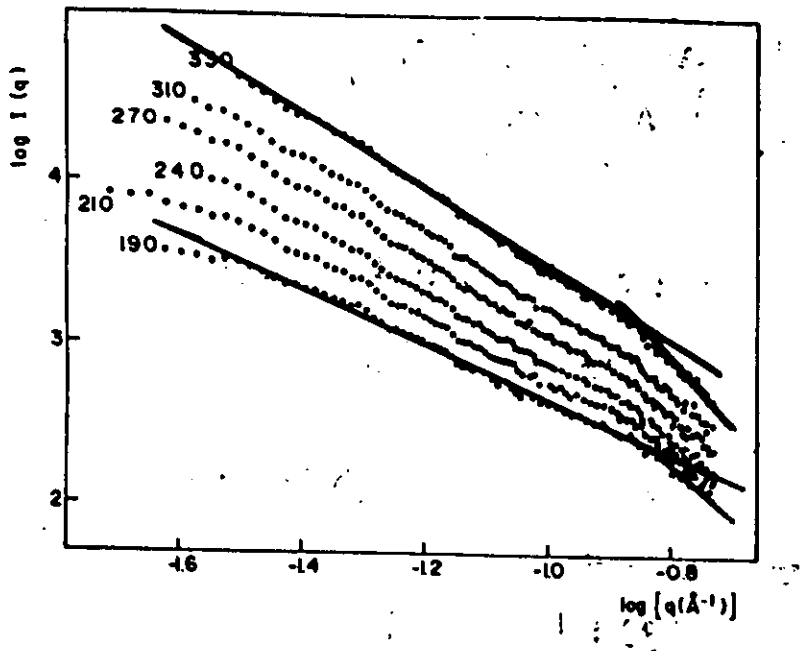

FIG. 1

2.1 Isothermal spinodal decomposition

$$\frac{\partial c(\vec{r},t)}{\partial t} = D\nabla^2 c(\vec{r},t) - \kappa'\nabla^4 c(\vec{r},t) \quad (1)$$

$$I(k,t) = I(k,0)\, e^{2R(k)t} \quad (2)$$

$$R(k) = -Dk^2\left(1 - \frac{k^2}{k_c^2}\right) \qquad k_M = k_c/\sqrt{2}. \quad (3)$$

$$I(k,t) = |I(k,0) - L(k,T_g)|\, e^{2R(k)t} + L(k,T_g) \quad (4)$$

$$D(t) = D + D' e^{-\frac{t}{\tau}} \quad (5)$$

$$I(k,t) = I(k,0)\, e^{2R(k)\tau}\, e^{2R'(k)\tau\left(1 - e^{-\frac{t}{\tau}}\right)} \quad (6)$$

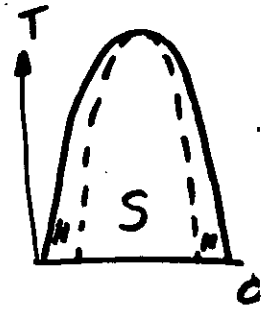

2.2 Nucleation and Growth

$$R = \gamma/Dc \quad (7)$$

$$I(k) = A R^6 e^{-\frac{1}{5}R^2k^2} \quad (8)$$

$$A(k_1,t) = A' t^3 e^{-\frac{1}{5}\gamma' k_1^2 t} \quad (9)$$

2.3 Coarsening

$$A(t) = \int k^2 I(k,t)\,dk \quad (11)$$

$$R^3 = a + gt \quad (10)$$

Hennion, Renaud, Gayot (1982)

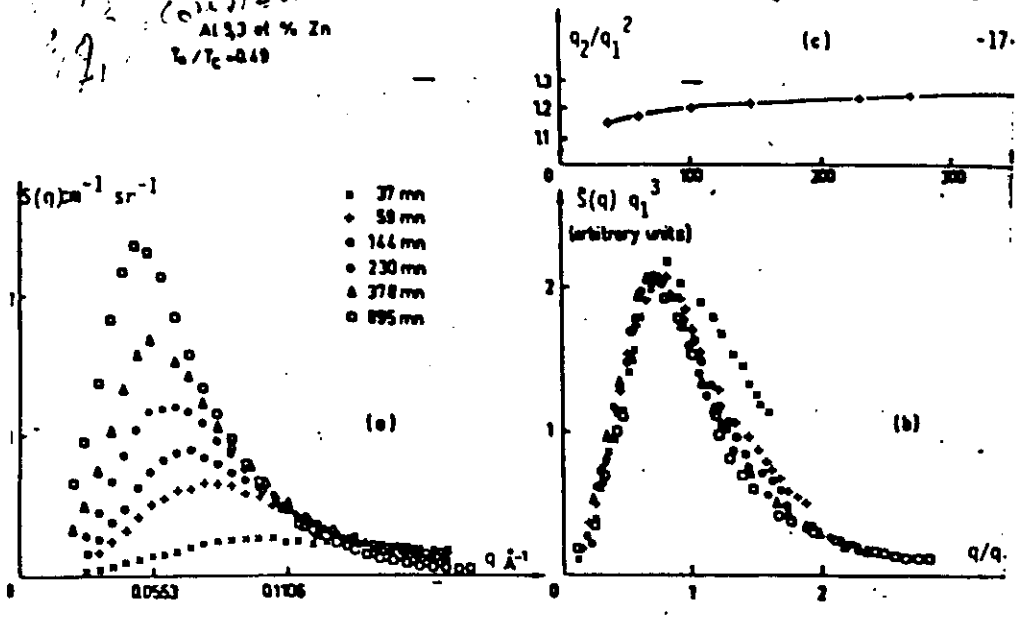

Fig. 12 : Al-5,3 at.% Zn. T = 20°C. a) S(q,t) moyen pour différents temps de vieillissement. b) $\bar{S}(q).q_1^3 = f(q/q_1)$. c) q_2/q_1^2.

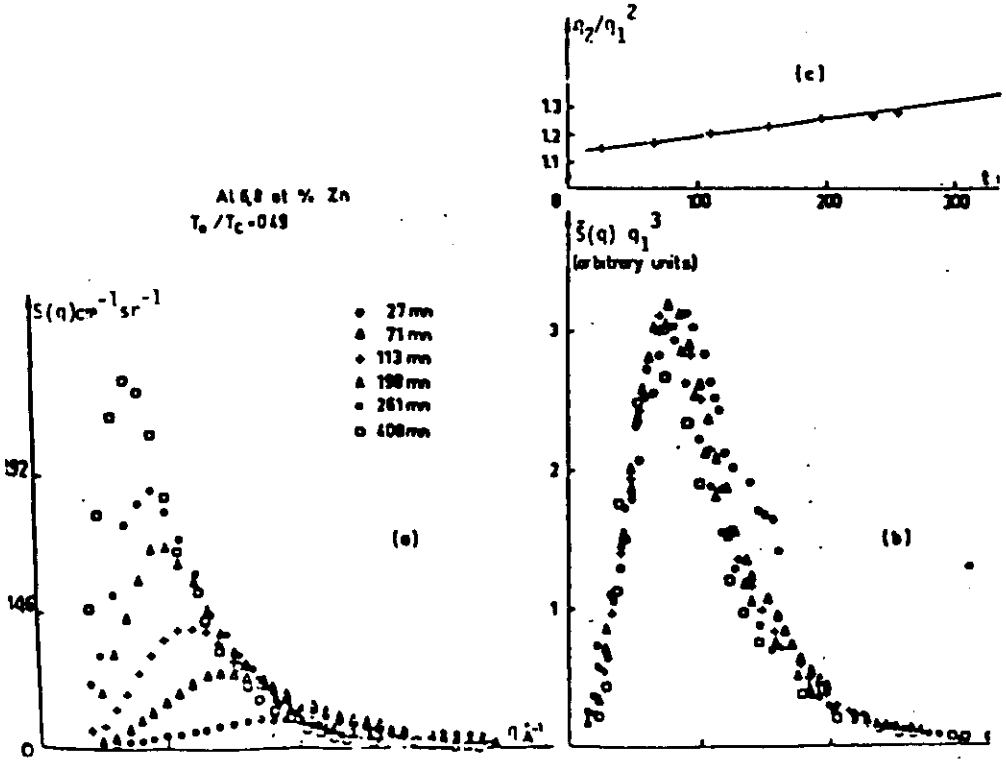

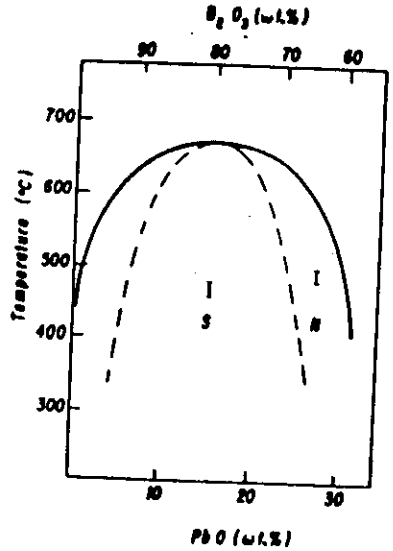

FIG. 1. Miscibility gap for the quasibinary B_2O_3-PbO-Al_2O_3 glass system, from Ref. 15. The continuous line corresponds to the solubility limit and the dashed line is the classical spinodal. The bars *S* and *N* indicate the composition and temperature range investigated in this work.

Crichwich
Sanchez
Williams
Phys Rev. B
34, 2762 (1986)

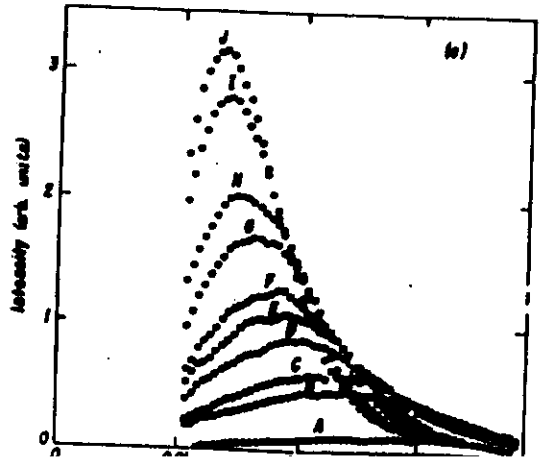

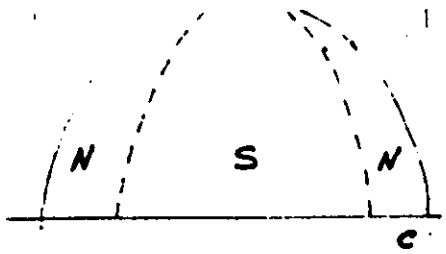

Physica 86-88B (1977)

KINETICAL ISING MODEL

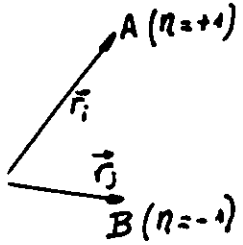

$$U = -J \sum \eta(\vec{r}_i)\cdot\eta(\vec{r}_j) \qquad J > 0$$

$$P_{ij} = \propto e^{-\beta \Delta U_{ij}/(1+e^{-\beta \Delta U_{ij}})}$$

$$\beta = 1/k_B T \qquad \propto = \nu_0 e^{-\Phi/k_B T}$$

$$J/T_c k_B = 0.89$$

$$S(\vec{q},t) = \sum_{\vec{r}} e^{i\vec{q}\cdot\vec{r}} \sum_i [\eta(\vec{r}_i,t) - \bar{\eta}][\eta(\vec{r}_i+\vec{r},t) - \bar{\eta}]$$

$$S(\vec{q},t) = I(\vec{q},t)$$

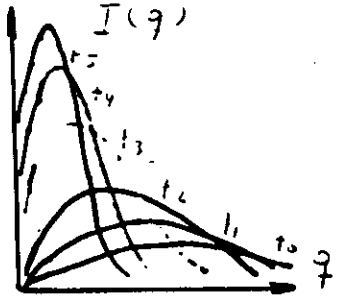

SCALING PROPERTIES OF THE STRUCTURE FUNCTION

$$S_n(t) = \int q^n I(q,t)\, dq$$

$$q_n(t) = S_n/S_0$$

$$\frac{S(q,t)\cdot q_1^3(t)}{\text{or}}$$

$$\frac{I(q,t)\cdot q_1^3(t)}{}$$

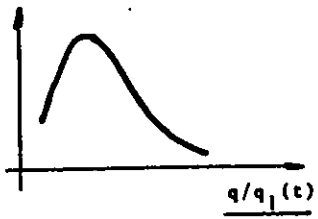

$q_1 \propto t^{-a}$ $\quad a \simeq 0.22$

$a \simeq 0.29$

Marro et al. Phys. Rev. Lett. 43, 282 (1979)

Dynamical scaling:

$$S(q,t) = [K(t)]^{-3} F[q/K(t)]$$

$$K(t) = q_1(t)$$

$$q_1(t) = \frac{\int q\, S(q,t)\, dq}{\int S(q,t)\, dq}$$

1) $q_1 \propto t^{-a}$

2) $S_M \propto t^{+a'}$

$a' = 3a$

3) $q_2 \propto q_1^2 \therefore \frac{q_2}{q_1^2} \neq f(t)$

4) $F(q/q_1) = q_1^3\, S\left(q/q_1, t\right)$

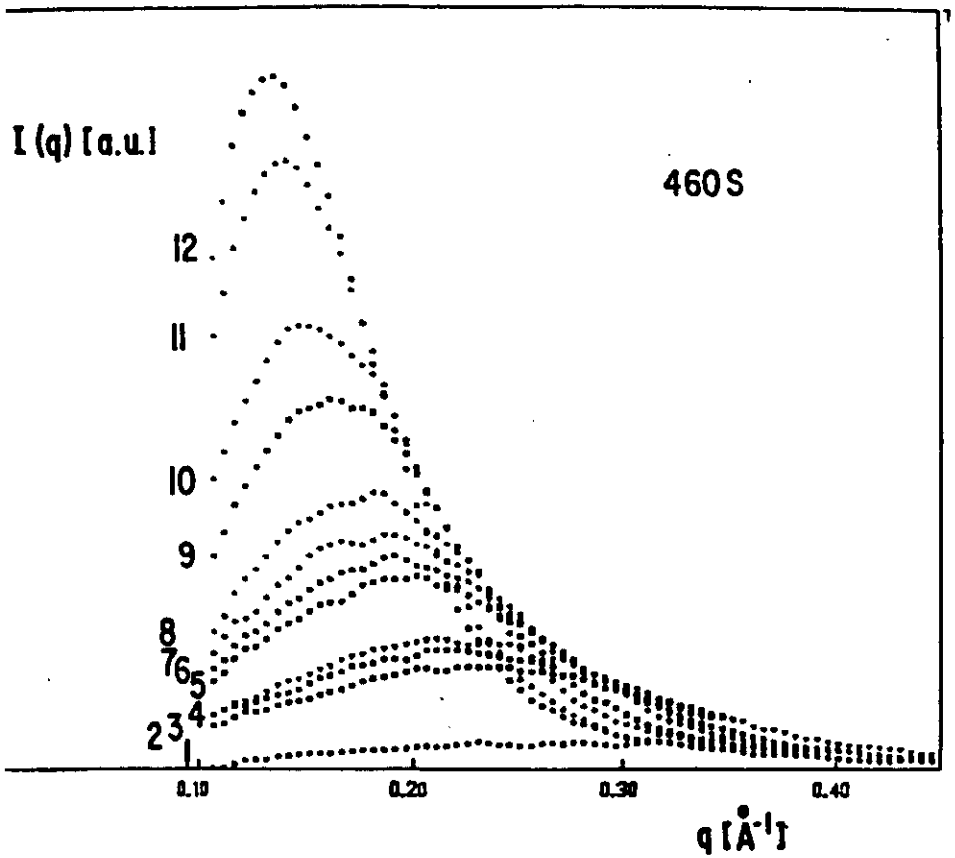
I (q) [a.u.]
460 S
12
11
10
9
8
7
6
5
4
3
2
1
0.10
0.20
0.30
0.40
q [Å⁻¹]

$I(q)\, q_m^3$

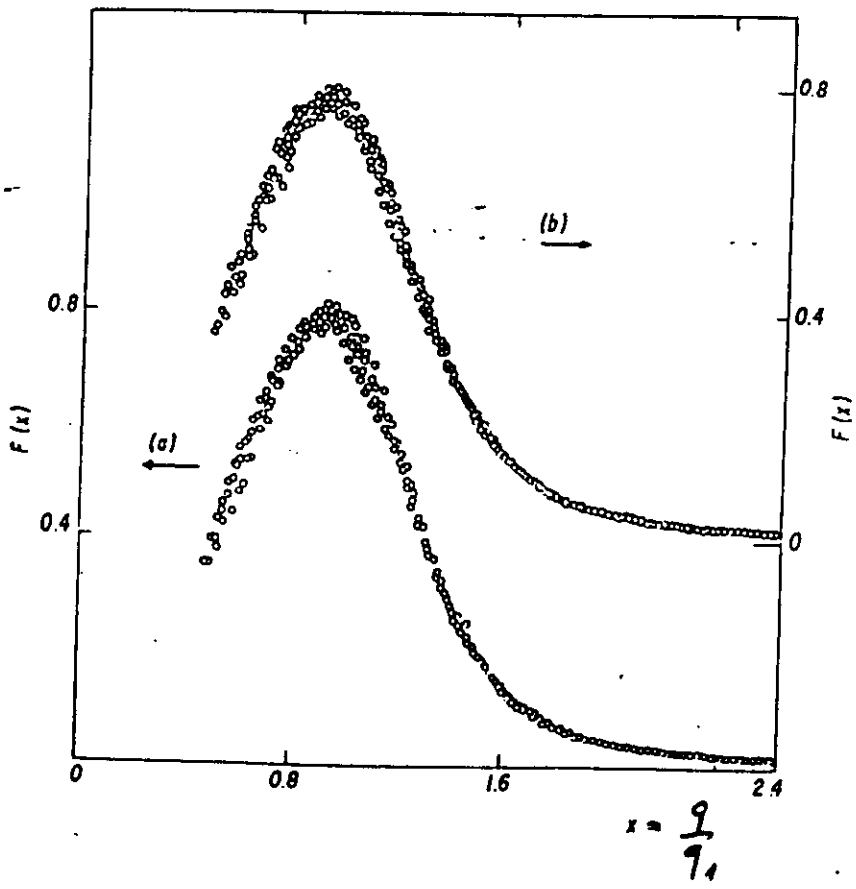
(b)
(a)
F (x)
F (x)
0.8
0.4
0
0.8
0.4
0
0.8
1.6
2.4
x = q/q₁

Fig. 8

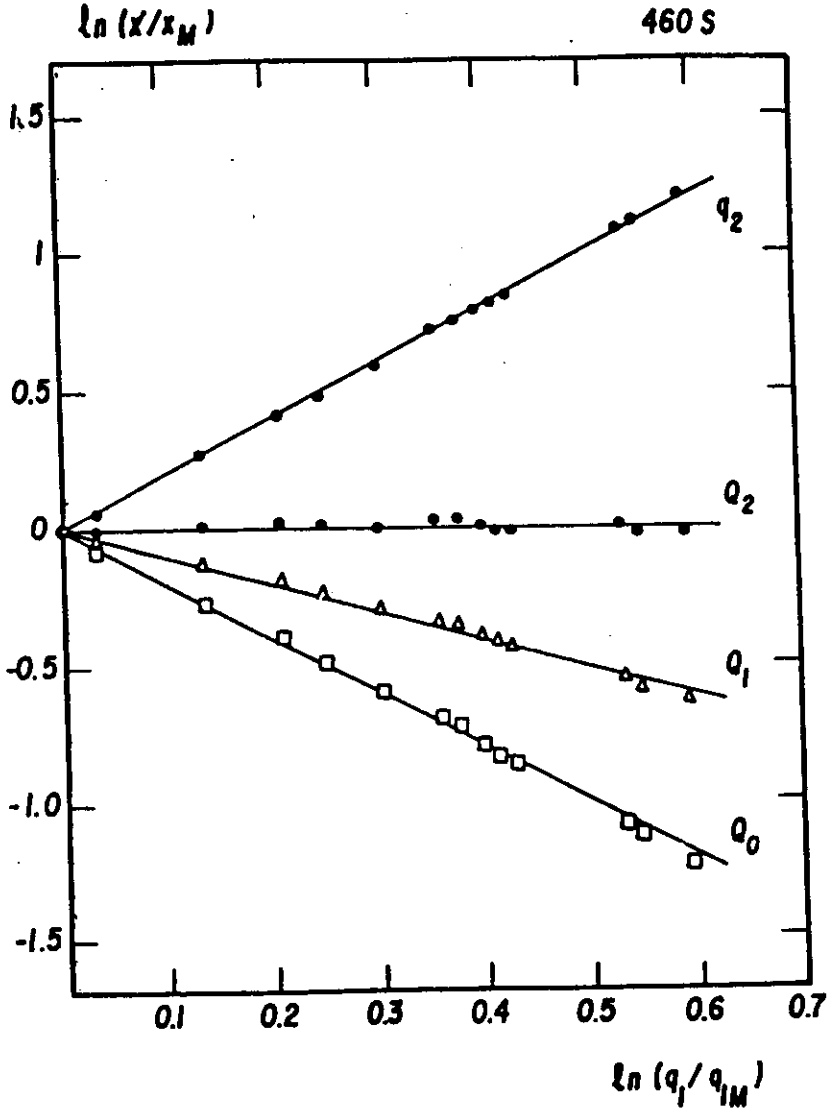

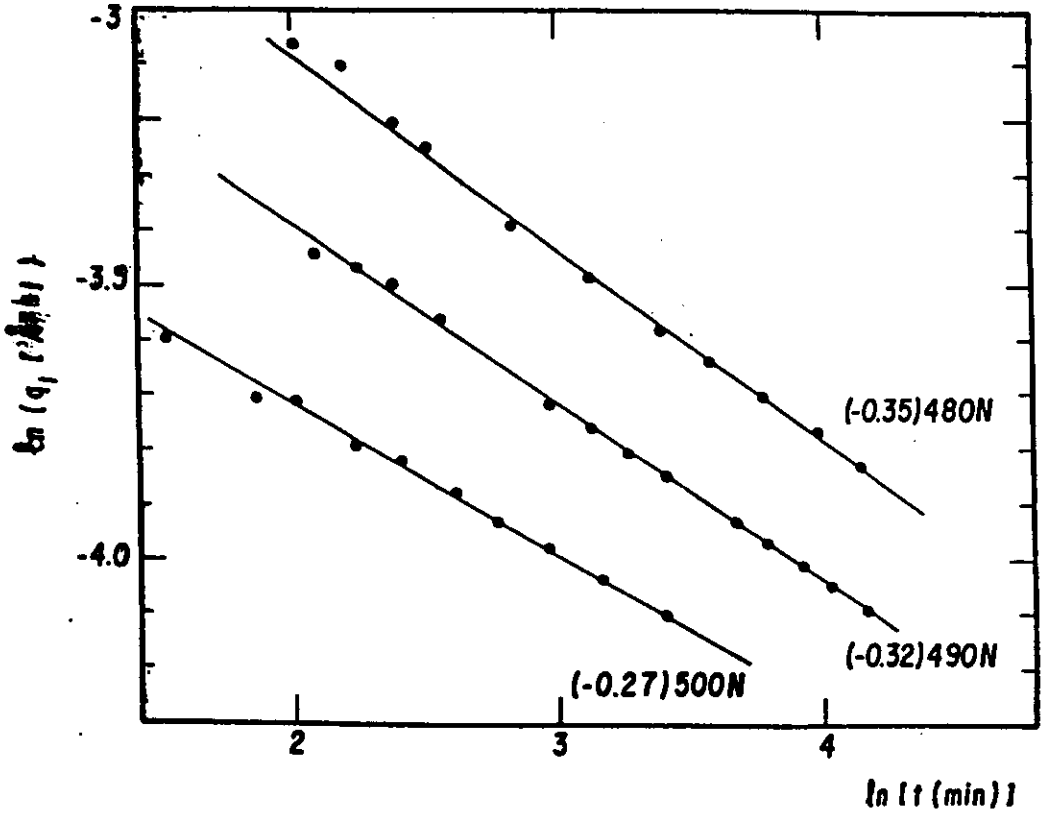

Theory : $q_1 \propto t^{-\frac{1}{2}}$

Theory :

$q_2 \propto q_1^2$

$S_n \propto$

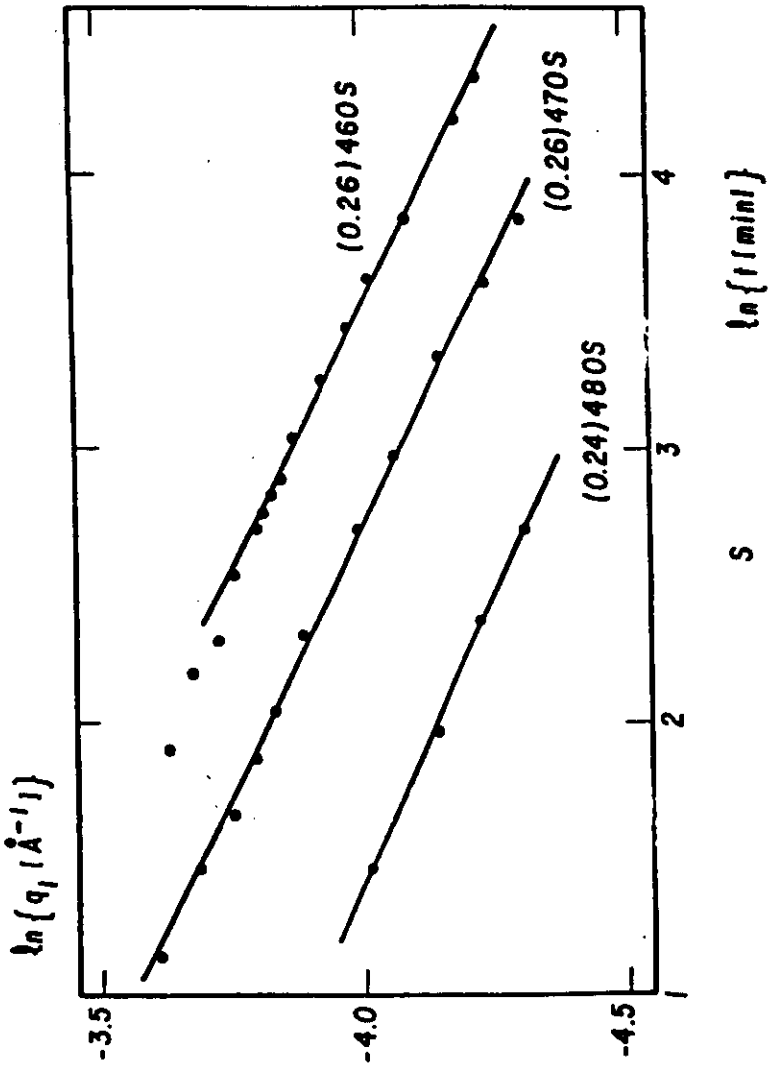

SPINODAL REGION

- Theory of spinodal decomposition (Cahn) Linear theory (valid only for early stages).
- Reasonable agreement with experiments on alloys (Al-Zn, Au-Pt).
- Poor agreement with experiments on glasses (B_2O_3-PbO-Al_2O_3, SiO_2-Na_2O).

NUCLEATION AND GROWTH

- Classical diffusion theory ("GP" zones in alloys and "droplets" in glasses).
- Ambiguous comparisons between theory and experiments.

NEW THEORIES

- Kinetical Ising model for simple cubic lattice.
- Calculations by computer simulation using Monte Carlo method.
- Scaling properties and "universality".

Cahn's theory was applied to explain the kinetics of SAXS from real phase separation systems under isothermal conditions and, we could say, that it has had an only limited sucess for early stages in alloys.

Its agreement with experimental results in glassy systems was poorer, probably because of the intrinsic impossibility for isolators of reaching high quanching rates.

Recent new theoretical developments have considerably simplified the picture of phase separation. They are based on the Ising model for ferromagnets applied to binary alloys by using computer simulation and the Monte Carlo method.

This theories lead to scaling and "universality" properties of the structure function.

The first theoretical study of the complex phenomena of phase separation in solids was provided by the now classic theory of spinodal decomposition of Cahn. Central to the theory is the fact that, within the "spinodal" region, the homogeneous mixture is unstable to small concentration fluctuations of the system. The evolution equation of the Fourier components of the atomic composition and, consequently, of the small angle X-ray scattering intensity could only be solved in closed form after linearization. Therefore it can only be applied to very early stages of phase separation.

Outside of the spinodal region, i.e. near the boundary of the miscibility gap, the decomposition process was described by the classical diffusion theories of nucleation and growth of "GP zones" (in alloys) or "droplets" (in glasses).

Binaire systems (1,2)

$$I(E,q) = F_1(q,E)^2 S_{11} + 2F_1(E) F_2(E) \cos\varphi S_{12} + F_2(E)^2 S_{22}$$

In order to obtain S_{11}, S_{12} and S_{22} it is necessary to perform three experiment at three different energies: (I, F e S are function of q).

$$I(E_1) = F_1(E_1)^2 S_{11} + 2F_1(E_1) F_2(E_1) \cos\varphi S_{12} + F_2(E_1)^2 S_{22}$$

$$I(E_2) = F_1(E_2)^2 S_{11} + 2F_1(E_2) F_2(E_2) \cos\varphi S_{12} + F_2(E_2)^2 S_{22}$$

$$I(E_3) = F_1(E_3)^2 S_{11} + 2F_1(E_3) F_2(E_3) \cos\varphi S_{12} + F_3(E_3)^2 S_{22}$$

In matricial form:

$$(\bar{I}) = (\bar{F})(\bar{S})$$

A method to estimate the errors propagation in solving this equation uses the Turing relation:

$$\frac{\| \Delta S \|}{\| S \|} \leq \| F \| \, \| F^{-1} \| \frac{\| \Delta I \|}{\| I \|}$$

where $\| A \|$ are the norm of vectors and matrix:

$$\| A \| = (\sum_{ij} a_{ij})^{\frac{1}{2}}$$

CONCLUSIONS

- Real space analysis (T.E.M.) does not allow quantitative studies of phase separation.

- Cahn theory for spinodal decomposition is not a good approximation for isothermically phase separating real glasses.

- The statistical dynamic Ising model describes well the advanced stages of phase separation in glasses.

- Some discrepancies related to the scaled structure function have bean detected in the B_2O_3-PbO-Al_2O_3 system.

ASAXS

The scattered intensity may be written as

$$I(q) = \Sigma \, \Sigma f_j \, f_k^* \, S_{jk}(q)$$

$S_{jk} = S_{kj}^*$ is the partial structure factor

$$f_j = f_j^o + \dot{f}_j(E) + i\ddot{f}_j(E)$$

$$f_j^o(q \to 0) = Z_j$$

The ASAXS allows for the determination of the partial structure function S_{jk}.

SECOND SCHOOL ON THE USE OF SYNCHROTRON RADIATION IN SCIENCE AND TECHNOLOGY:
"JOHN FUGGLE MEMORIAL"

25 October - 19 November 1993

Miramare - Trieste, Italy

Additional Material

A. Craievich

J. Phys. I France 2 (1992) 801-811

Classification
Physics Abstracts
61.10F — 61.40

SAXS studies of phase separation in borate glasses and structural transformations in precursors of silica glass

Aldo Craievich

National Synchrotron Light Laboratory/CNPq, C.P. 6192, 13081 Campinas, SP, Brazil and Institute of Physics/USP, São Paulo, Brazil

(*Received 19 November 1991, revised and accepted 19 March 1992*)

Abstract. — Applications of SAXS to structural studies of oxide glasses are reviewed. The evolution in the basic understanding of the mechanisms involved in microphase separation in borate glasses is presented. Experimental SAXS results and their comparison with classical theories of spinodal decomposition and more recent statistical theories are discussed. Other applications of SAXS, such as the structural characterization of the « sol-gel route » to obtain silica glasses is outlined.

1. Introduction.

Transparent glasses have been considered as essentially homogeneous materials. SAXS and electron microscopy studies performed in the fifties demonstrated that many of these macroscopically homogeneous glasses are in fact heterogeneous at a submicroscopic scale. It was established that a number of silica and borate-based binary and more complex glasses exhibit a fine structure associated with a microphase separation process.

The microstructure of a number of phase separated glasses consists of segregation zones with sizes ranging from about ten Angstroms to several hundred Angstroms. The submicroscopic size of the heterogeneities and the existence of an electronic density contrast between the phases makes SAXS an adequate experimental technique for the study of these materials.

Phase separation in multioxide glasses is associated with the existence of a miscibility gap in their phase diagram. The gaps correspond to a condition of quasi-equilibrium of these materials. When the glass system has many oxide components, basic studies of the process of phase separation become complex. For this reason, theoretical and experimental investigations of phase separation are usually performed on binary or quasi-binary glasses. These studies generally deal with an initially homogeneous sample outside the miscibility gap, which is brought by fast quenching into the gap and is maintained in it at a constant temperature. The structural characteristics of the phase separating glasses are then studied at increasing heat-treatment times. The question is to establish the features of the unmixing process starting with the initially quasi-homogeneous glass and leading to the final equilibrium two-phase material.

The conventional method to produce glasses involves the melting of the raw materials and the subsequent more or less fast cooling of the melt. In order to produce common silica-based glasses, the use of high temperature (1 500 to 2 000 °C) furnaces is required. The « sol-gel route » to obtain oxide glasses is an alternative procedure which starts from a liquid solution of alkoxides, containing the oxide of the resulting glass, water and alcohol. After several processes at rather low temperatures, from room temperature up to about 1 000 °C, monolithic and extremely pure glasses can be produced. By an appropriate control of the preparation and heating conditions, a variety of porous glasses can also be obtained. These materials exhibit interesting structural, thermal and optical properties which make them useful for many applications, such as transparent and opaque insulators, gas filters, Cerenkov detectors, catalytic substrates, etc.

The method to produce monolithic and homogeneous glasses by the sol-gel route involves aggregation of monomers in a liquid phase, gelation, aging, drying and sintering. Through all the partial steps, the evolving system is heterogeneous at a submicroscopic scale. In a number of glass precursors, the heterogeneity size covers the range from some Angstroms to several hundred Angstroms along all the process. By an adequate choice of the components and the control of the various preparation steps, it is possible to obtain monolithic and porous glasses with designed properties.

This paper reviews the main experimental results and conclusions of the SAXS studies done by the author and his collaborators concerning phase separation in borate glasses and the sol-gel procedure to obtain silica glasses.

A standard X-ray source and a SAXS goniometer were used for the experiments done until 1980. The experiments carried out since 1981 were performed at the LURE synchrotron radiation facility, in Orsay. Most of the experiments referenced in this review correspond to kinetic studies performed *in situ* using temperature-controlled cells for the samples. Two experimental workstations which provide intense, pin-hole collimated and monochromatic X-ray beams were used for the reported studies. The recording of the scattered X-ray photons was performed by means of gas position-sensitive detectors.

2. Phase separation.

Phase separation in multioxide glasses is related to the existence of a miscibility gap in the phase diagrams. Most of the basic experimental investigations of phase separation deal with simple binary or quasi-binary systems. Silica-based and borate glasses are the most thoroughly studied systems. A schematic miscibility gap corresponding to a binary or quasi-binary system is presented in figure 1. The two-phase region is divided into two subdomains by a so-called spinodal line. This line is a boundary enclosing the composition-temperature domain for which the continuous variation in composition in an initially homogeneous matrix does not require overcoming any free energy barrier. The thermodynamic theories which were used to describe phase separation suggested the existence of two different and well-defined mechanisms for phase separation : spinodal decomposition, within the central part of the miscibility gap, and nucleation and growth between the spinodal line and the gap boundary.

The thermodynamic linear Cahn's theory for spinodal decomposition [1] was widely applied to the study of metastable aggregation in metallic solid solutions. The main prediction of this theory concerns the time evolution of the q-component of SAXS intensity, $I(q)$, produced by phase separating binary systems. This evolution is expressed by

$$I(q, t) = I(q, 0)\, e^{2R(q)t} \qquad (1)$$

$R(q)$ being an amplification factor which is positive for $q < q_c$ and negative for $q > q_c$. For $q = q_c$ (the crossover), the SAXS intensity remains constant during the phase separation

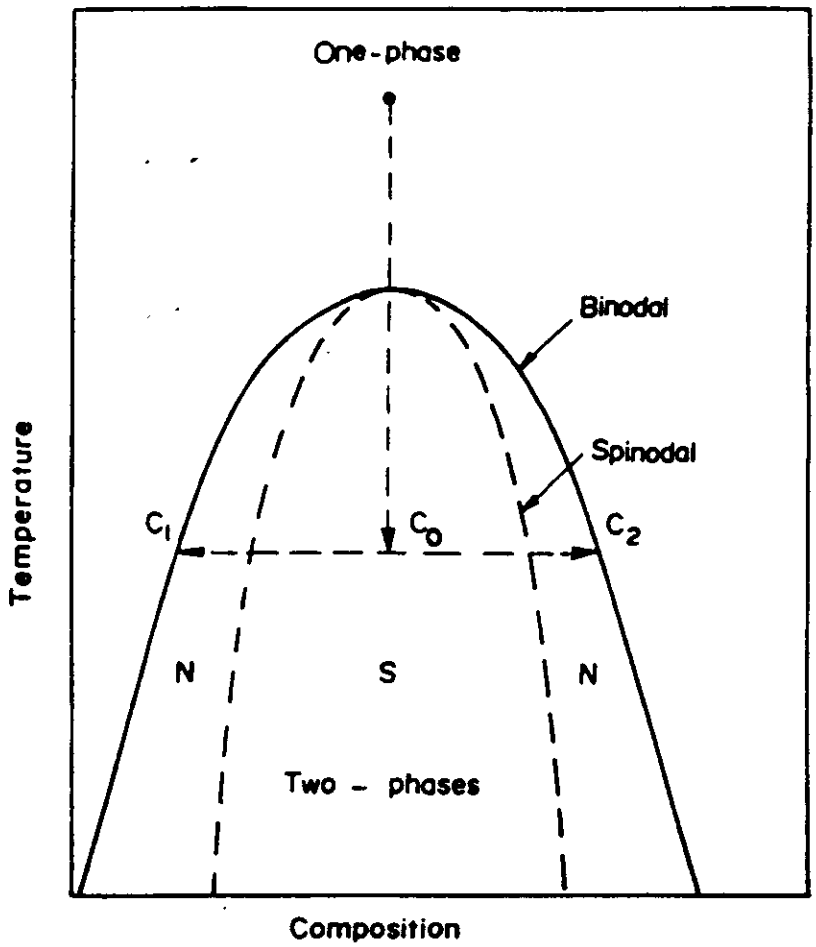

Fig. 1. — Schematic phase diagram of a binary solution with a miscibility gap. A typical temperature-composition path in phase separation studies is indicated (c_0 is the composition of the initial homogeneous phase and c_1 and c_2 are the compositions of the final phases). The « spinodal » and « nucleation and growth » domains are indicated by S and N, respectively.

process. This theory applies to the first stages of phase separation. At more advanced stages, non-linear contributions should be added and, consequently, a more complex evolution of SAXS intensity curves is expected.

The solid solutions between the spinodal and the binodal lines are expected to separate in two phases through the formation of nuclei of one of the stable or metastable equilibrium phases and its subsequent growth. The classical diffusion theory for the growth of spherical nuclei immersed in a isotropic matrix predicts the average size of the zones R at a time t:

$$R \propto t^{1/2}. \tag{2}$$

At advanced stages of phase separation, when the matrix approaches its equilibrium composition, a coarsening process becomes dominant. In this process, the smaller particles dissolve and the larger grow at their expense. The expected time evolution of the average

radius of the spherical zones in this coarsening stage is given by the Lifschitz and Slyozov equation [2] :

$$R^3 - R(0)^3 = Kt \qquad (3)$$

K being a constant.

The theoretical time evolution described by equations (2) and (3) can be experimentally verified by SAXS, using the Guinier law to determine the average radius of gyration of the segregation zones. The assumption of a spherical shape for the zones can be safely applied to glasses, since electron microscope studies put in evidence the presence of isolated spherical droplets in many vitreous systems near the binodal boundary. The direct application of Guinier's law to these systems may be subject to errors because they cannot be considered as diluted solutions of isolated particles. In practice, the droplets exhibit a size distribution which make Guinier's law applicable even to moderately diluted particle systems.

The first SAXS investigation of phase separation which tried to test the Cahn linear theory for spinodal decomposition [1] in glasses was published by Zarzycki and Naudin [3]. The experimental results of these authors concern the B_2O_3-PbO-(Al_2O_3) quasi-binary system. This study is in qualitative accordance with Cahn's theory. The agreement cannot be considered as a quantitative verification of the theory for spinodal decomposition because the experimental $R(q)$ functions exhibited clear deviations from the predicted q-dependence. In addition, a clear crossover of the experimental SAXS curves was not observed.

Another study of the B_2O_3-PbO-(Al_2O_3) glass system at two temperatures, within the spinodal domain, was performed [4]. This study showed clear deviations of the experimental SAXS results from those predicted by the linear theory for spinodal decomposition. The time evolution of $I(q, t)$ indicated a pronounced deviation from equation (1) during the earliest stage of the process. The same study [4] verified the applicability of equation (3) for a glass system within the spinodal region of the miscibility gap.

An explanation for the deviation of the experimental SAXS results [4] for glasses from those predicted by the theory for spinodal decomposition was tried [5]. It was argued that the probable existence of a structural relaxation after the thermal quenching of the homogeneous glass may affect the first stages of phase separation. The transient variation in the atomic mobility was assumed to be a simple exponential function with a characteristic relaxation time [5]. This model of a relaxing structure explained the deviation of the experimental $I(q, t)$ function from the behavior stated by equation (1). Nevertheless, the model does not describe the absence of the crossover of the experimental curves nor the deviation of the experimental $R(q)$ function from the theoretically expected one in a simple way.

Parallel to these experimental studies of phase separation in glass systems, many investigations dealt with the formation of Guinier-Preston zones in metallic binary solid solutions (Al-Zn, Al-Ag, etc.). The linear theory for spinodal decomposition applied to alloys showed an agreement with the experimental results which was in general better than in the case of glasses. The reasons for this different behavior were unclear at the time.

One strong difference between the studied borate glasses and metallic alloys concerns their speed of cooling during the quenching process. Metallic homogeneous solid solutions can be more easily retained by fast cooling than oxide glasses. Even using fast splat-cooling techniques, the low thermal diffusivity coefficient of glasses puts serious limitations on the maximum attainable cooling rate. It was considered that the reason for the failure of the linear theory for spinodal composition to explain the experimental SAXS results for glasses quantitatively was the eventual practical impossibility of attaining the « first stages » of phase separation in the isothermal studies of glasses. As a matter of fact, the linear theory applies for systems with small variation in the initial composition.

A new attempt to describe the unmixing process in glasses started with the assumption that an appreciable amount of phase separation occurs during the quenching. Several samples of

the same B_2O_3-PbO-(Al_2O_3) glass were cooled down to room temperature at different rates and studied by SAXS [6] before any subsequent heat treatment. A good agreement between experimental results and a linear theory of spinodal decomposition during continuous cooling [7] was established. This result seemed to confirm the first ideas about the glass samples which were investigated under isothermal conditions. The conclusion was that the « early stages » of phase separation mostly occur for these samples during the cooling process and, consequently, all the previously performed experimental isothermal studies correspond to « advanced stages » for which the linear Cahn theory does not apply.

A new statistical theory was developed in the seventies to describe the unmixing process in solid solutions [8]. This theory involves the numerical solution of a kinetic equation [9] for binary systems and describes the initial clustering of the atoms and the advanced coarsening stage as well. The calculation of the structure function, which is proportional to the SAXS intensity function $I(q, t)$ was carried out by Monte Carlo simulations [10].

The time evolution of the scattering intensity $I(q, t)$ predicted by the statistical theory, exhibits a remarkably simple behavior for advanced times of phase separation. The experimental test of this theory for the advanced stages can be done through the analysis of the variation with time, under isothermal conditions, of several functions related to SAXS intensity integrals. As an example, the function

$$q_1(t) = \int I(q, t)\, q\, dq / \int I(q, t)\, dq \tag{4}$$

should theoretically have the simple t-dependence :

$$q_1(t) \propto t^a \tag{5}$$

where a is a negative constant which depends on the mechanism of clustering.

Monte Carlo simulations also demonstrated the dynamical scaling of the SAXS intensity functions $I(q, t)$. It was deduced that the SAXS intensity functions for different times at constant temperature, plotted as $I(q/q_1)\, q_1^3$ *versus* q/q_1, should scale as a single time-independent and characteristic function $S(x) = I(x) \cdot q_1^3$, x being equal to q/q_1.

Another feature of the statistical theory is that it holds for any composition within the miscibility gap. It does not predict any sharp boundary between spinodal and nucleation and growth domains. Since this theory becomes very simple for advanced stages of unmixing, its use for a better understanding of the phase separation mechanism in glasses appeared to be worthwhile.

The first application of the statistical theory to investigate phase separation in glasses by SAXS was done on a borate system inside the spinodal domain of the phase diagram [11]. An additional SAXS investigation of borate glasses at two temperatures and of two compositions (in the central part and near the boundary of the miscibility gap) were carried out later [12].

The statistical theory explains the main characteristics of the SAXS results related to phase separation in borate glasses [11]. The good agreement between theory and experiment verified the correctness of the assumptions involved in the statistical theory for advanced stages of phase separation. The good agreement was found for compositions inside the « spinodal » and in the « nucleation and growth » region as well. This suggests that the statistical theory does describe phase separation in the whole miscibility gap.

An experimental result which remains unclear concerns the composition dependence of the scaled SAXS function $S(x)$. Theoretical evaluations of the scaled SAXS function indicate that they are peaked curves with a half-maximum width which depends on the composition. This scaled structure function was calculated by several authors for simple models [13]. Its half-

maximum width turns out to be lower for compositions in the central part of the miscibility gap than for compositions near the binodal boundary. Experimental SAXS studies of quasi-binary borate glasses lead to an opposite conclusion [12]. A half-maximum width 15 % lower for a composition close to the binodal than that corresponding to the central part of the gap was experimentally observed.

The inconsistency mentioned in the precedent paragraph may be due to the fact that SAXS experiments were not done on rigorously binary systems. To verify that, similar SAXS studies should be carried out in two-oxide glasses. It must be pointed out that borate glasses (as for example B_2O_3-PbO) are not adequate for this purpose because in this binary system most of phase separation occurs during cooling. Al_2O_3 is added to the binary borate glasses in order to increase their viscosity and, consequently, to reduce phase separation during cooling. Silica glasses (SiO_2-Na_2O, SiO_2-Li_2O, SiO_2-BaO) are more suitable for the suggested investigation. An alternative reason for the lack of agreement between the theoretical and experimental composition dependence of the scaled structure function may be the eventual impossibility for the simple theoretical models to describe the real structure of the studied quasi-binary glasses.

3. The « sol-gel route » to glass.

The « sol-gel route » is an alternative method for obtaining monolithic homogeneous and porous glasses. It does not require the melting of raw materials and involves several stages, starting from liquid solutions of alkoxides, water and alcohols at room temperature. The different stages of this procedure are : monomer aggregation, gelation, aging, drying and sintering. A schematic picture of the method is given in figure 2.

Aggregation, or clustering, proceeds by the hydrolysis of the alkoxide monomers and further polycondensation in liquid phase. The clusters increase in size by different mechanisms of growth depending on the chemical conditions. Several mechanisms may be responsible for cluster growth such as particle-cluster or cluster-cluster aggregation [14]. The kinetics of clustering is controlled by diffusion or chemical reaction, depending on the efficiency of the « sticking » effect when two particles come into contact after diffusion through the liquid phase. Different types of clustering mechanisms in real solutions, which are used as glass precursors, are responsible for the formation of aggregates with fractal structure [14]. Real fractal structures are characterized by three parameters. One of them, r_0, corresponds to the size of the primary particle which builds up the fractal aggregates. Another parameter is the overall size, R_0, of the clusters. The third parameter is the dimensionality D of the fractal objects, which depends on the mechanism of cluster growth. These three parameters can in principle be easily determined in ideal systems by SAXS : the crossovers of the SAXS curves in log-log scales permit the evaluation of r_0 and R_0 and the slope of the central part yields the fractal dimensionality D, as shown in figure 3. The experimental SAXS plots associated with a fractal structure exhibit the above mentioned features provided $R_0 \gg r_0$. The simple equation

$$I(q) \propto q^{-D} \tag{6}$$

holds for $1/R_0 \ll q \ll 1/r_0$.

After some time, which depends on composition and temperature, the gelation of the solutions containing the growing clusters eventually occurs. Microscopically, gelation corresponds to the percolation of the individual clusters. The isolated clusters build up a continuous structural network at the gel point.

The resulting structure is not stable after gelation. Monomers still can diffuse through the liquid matrix leading to additional structural modifications. This process is so-called gel aging.

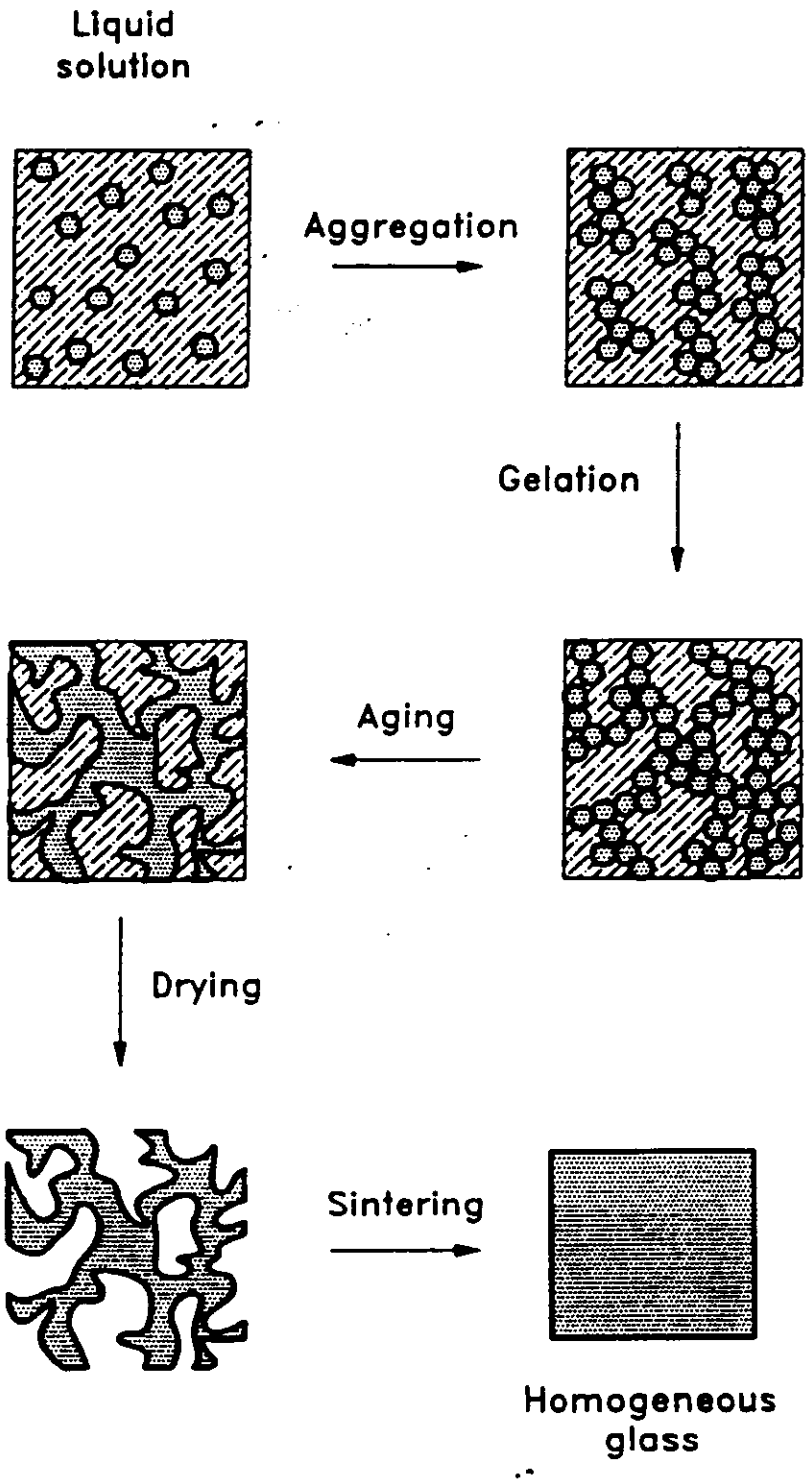

Fig. 2. — Structural transformations in the sol-gel procedure to obtain homogeneous glasses (schematic).

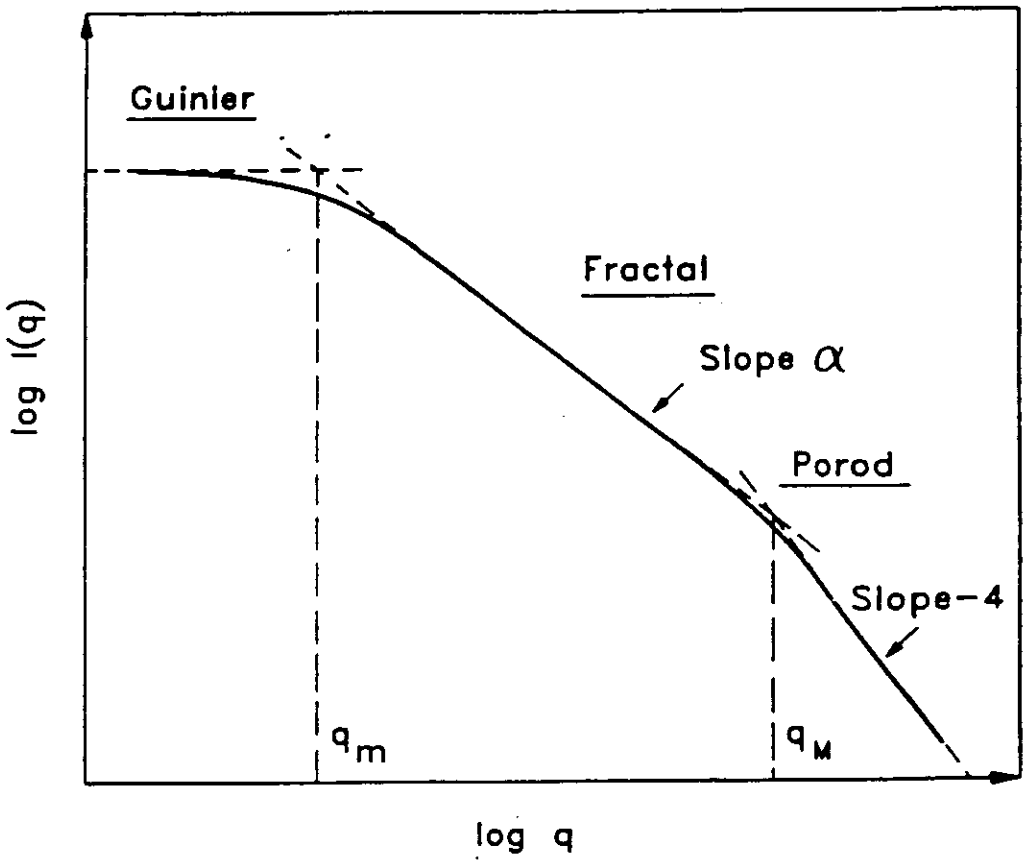

Fig. 3. — Ideal SAXS plot from a fractal structure in a log-log scale. The parameters r_0, R_0 and D are given by $1/q_M$, $1/q_m$ and $|\alpha|$, respectively. The presence of both crossovers in actual experimental plots depends on the sizes of the primary particles and fractal aggregates.

After aging, the wet gel is dried. The drying is often performed under hypercritical conditions of pressure and temperature in order to suppress the strong capillary effect of the interfaces liquid-gas within the micropores. Using this technique monolithic porous aerogels (dry gels) are obtained. The aerogels may be more or less compact depending on the dilution of the precursor solutions. In extreme conditions, the density may be very low. In the case of aerogels of silica, very light aerogels having about 1 % of the density of homogeneous silica glass were obtained.

The last stage of the procedure to obtain monolithic homogeneous glasses is the heating of the aerogels at increasing temperatures in order to evaporate the organic components and, at higher temperatures, to eliminate the porosity. This last sintering process should be carried out at temperatures as low as possible in order to avoid crystallization.

The structural properties of the final monolithic homogeneous or porous glasses depend on the composition of the precursor solution and on the conditions under which each one of the preparation stages is carried out. This makes the characterization of every stage of the process useful. Many silica and other glass precursor materials exhibit a very fine submicroscopic structure from the initial monomer solution to the gel and aerogel states. Therefore, the SAXS technique can be used to study all structural evolution occurring along the sol-gel process.

The most common silica glass precursor solutions are liquid mixtures of TEOS-water-ethanol and TMOS-water-methanol. They were experimentally studied by SAXS under acidic and basic conditions using different alkoxide/water and alkoxide/alcohol ratios.

An experimental SAXS study of the clustering process in solutions of TMOS-water-methanol suggested different mechanisms of aggregation for different TMOS/water ratios [15]. The ratio R controls the degree of monomer hydrolyzation and is defined as R = (mol TMOS/mol water). Guinier plots of SAXS results were applied to characterize the growth of the clusters. The $\log I$ *versus* $\log q$ plots of the SAXS curves, for increasing aggregation times, approached a straight line for both acid and base catalyzed solutions. The fractal dimensionality values corresponding to the solutions under acidic conditions, were $D = 2.00$ for $R = 1$ and 2 and $D = 2.14$ for $R = 4$. In the case of a base-catalyzed solution with $R = 1$, a higher value of the fractal dimensionality was obtained ($D = 2.60$). An analysis of these experimental SAXS results, based on a model which assumes a polydispersivity in cluster size, was tried. For a polydisperse system having a number distribution in cluster mass given by $N(m) \propto m^{-\tau}$, the SAXS intensity exhibits the same potential dependence on the scattering wavevector as equation (6), but in this case the exponent depends on D and τ [16]:

$$I(q) \propto q^{-\alpha} \quad \text{with} \quad \alpha = D(3 - \tau). \tag{7}$$

For three dimensional clusters, the percolation theory predicts $D = 2.5$ and $\tau = 2.2$ [16] and then equations (7) yield $\alpha = 2.0$. The experimental values of α for the acid-catalysed sols studied in reference [15] are close to 2, in good agreement with the model of percolation clusters. It should be pointed out that equations (7) holds strictly for dilute cluster solutions. Since the experimental results reported in reference [15] concern undiluted solutions, the conclusion concerning the mechanism of gel formation may be biased by concentration effects.

The SAXS plots in log-log scale of the wet silica gels prepared from the precursor solutions mentioned in the precedent paragraph show more complex features [17]. Two linear regions were observed for most of the compositions. This was attributed to the existence of a two-level fractal structure : the primary particles having a size of about 2 A generate fractal clusters with an average size of 20 A and these clusters grow up to larger dimensions building up secondary fractal objects. In the case of gels, the parameter R_0 obtained from SAXS plots corresponds to a correlation distance, instead of representing a radius of gyration, because after gelling clusters are no longer isolated zones. The experimental results of reference [17] indicated that the aging process decreases the correlation length. This suggests that aging modifies the structure and destroys its fractal features.

The drying produces some minor variations in the resulting aerogel structure as compared with that of the precursor wet gel [18]. The asymptotic behavior of the experimental SAXS curves corresponding to aerogels satisfy Porod's law :

$$I(q) \propto q^{-4}. \tag{8}$$

This suggests a smoothing effect of the hypercritical drying on the finer structure of the wet gels. The second upper level of the fractal structure of the wet gels is not modified by drying [18].

The sintering process in aerogels was also studied at increasing temperatures by SAXS. The experimental variations in SAXS curves demonstrate the progressive loss of the fractal characteristics of the structure. SAXS results on aerogels are consistent with a two-phase model composed of mesopores and a « light » matrix [19]. These results suggest the existence of micropores immersed in the matrix which are responsible for its low density.

A simple geometrical model of a hierarchical structure composed of spheres which contains 13 equal spherical particles, this structure being repeated at several levels, was proposed for dense aerogels [20]. This model was demonstrated to be consistent with SAXS experiments and BET measurements [21].

The reported SAXS studies of the structural transformations related to the sol-gel procedure have recently been extended to other systems such as mixed titania-silica [22], silica with formamide additions [23], zirconia [24], tin oxide gels [25] and silica gels which contain small semiconducting CdS particles [26].

4. Final remarks.

A number of SAXS studies of glasses was reported. It was shown that this technique provided useful information on phase separation processes in borate glasses and other more complex structural transformations concerning silica glass precursor materials.

The use of synchrotron radiation was helpful for the reported SAXS investigations. It allowed extensive studies of samples under many preparation conditions within a reasonable time. The SAXS workstations at LURE permitted the study of different kinetic processes which require good quality measurements in short time (typically a few minutes) intervals.

SAXS results could be directly and easily connected and compared with the related theories dealing with the mechanisms of structural transformation. This feature of the SAXS technique has an evident importance for basic research.

The structural characterization of the studied glasses may also have technological relevance. As a matter of fact, the knowledge of the effects of the physico-chemical conditions, along all the transformation process, on the structure of the resulting glasses is a necessary condition for correct material designs.

Acknowledgements.

The author acknowledges Professor André Guinier for the valuable advice and support during his first steps in the SAXS world and the LURE staff for the cooperation during the reported experiments.

References

[1] Cahn J. W., *Trans. Metall. Soc. A.I.M.E.* **242** (1968) 166.
[2] Lifschitz I. M. and Slyozov V. V., *J. Chem. Phys.* **19** (1961) 35.
[3] Zarzycki J. and Naudin F., *J. Non-Cryst. Solids* **1** (1969) 215.
[4] Craievich A., *Phys. Chem. of Glasses* **16** (1975) 133.
[5] Craievich A., *Phys. Stat. Solidi* **A 28** (1975) 609.
[6] Craievich A. and Olivieri J., *J. Appl. Cryst.* **14** (1981) 444.
[7] Acuna and Craievich A., *J. Non-Cryst. Solids* **34** (1979) 13.
[8] Binder K. and Stauffer D., *Phys. Rev. Lett.* **33** (1974) 1006.
[9] Furukawa H., *Prog. Theor. Phys.* **59** (1978) 1072.
[10] Boltz A. B., Kalos M. H., Leibowitz J. L. and Zendejas M. H., *Phys. Rev.* **B 10** (1974) 535.
[11] Craievich A. and Sanchez J. M., *Phys. Rev. Lett.* **47** (1981) 1308.
[12] Craievich A., Sanchez J. M. and Williams C., *Phys. Rev.* **B 34** (1986) 2762.
[13] Rikvold A. and Gunton J. D., *Phys. Rev. Lett.* **49** (1982) 1223.
[14] Schaeffer D. W. and Keefer K. D., *Mat. Res. Soc. Symp. Proc.* **32** (1984) 1.
[15] Lours T., Zarzycki J., Craievich A., dos Santos D. I. and Aegerter M., *J. Non-Cryst. Solids* **100** (1988) 207.

[16] MARTIN J. E. and ACKERSON B. J., *Phys. Rev.* A 31 (1985) 1180.
[17] CRAIEVICH A., DOS SANTOS D. I., AEGERTER M., LOURS T. and ZARZYCKI J., *J. Non-Cryst. Solids* **100** (1988) 424.
[18] DOS SANTOS D. I., AEGERTER M., CRAIEVICH A., LOURS T. and ZARZYCKI J., *J. Non-Cryst. Solids* **95** and **96** (1987) 1143.
[19] CRAIEVICH A., AEGERTER M., DOS SANTOS D. I., WOIGNIER T. and ZARZYCKI J., *J. Non-Cryst. Solids* **86** (1986) 394.
[20] ZARZYCKI J., Science of Ceramic Chemical Processing, L. L. Hench and D. R. Ulrich Eds. (Wiley, New York, 1986) p. 21.
[21] LOURS T., ZARZYCKI J., CRAIEVICH A. and AEGERTER M., *J. Non-Cryst. Solids* **121** (1990) 216.
[22] RAMIREZ DEL SOLAR M., ESQUIVIAS L., CRAIEVICH A. and ZARZYCKI J., *J. Non-Cryst. Solids* (1991) in press.
[23] BLANCO E., RAMIREZ DEL SOLAR M., DE LA ROSA FOX N. and CRAIEVICH A., Submitted (1991).
[24] CHAUMONT D., CRAIEVICH A. and ZARZYCKI J., *J. Non-Cryst. Solids* (1991) in press.
[25] VOLLET D. R., HIRATSUKA R. S., PULCINELLI S. H., SANTILLI C. V. and CRAIEVICH A. F., *J. Non-Cryst. Solids* (1991) in press.
[26] PIÑEIRO M., ZARZYCKI J. and CRAIEVICH A., In progress (1991).

J. Appl. Cryst. (1988). 21, 781-785

Small-Angle Scattering by Fractal Systems

By J. Teixeira

Laboratoire Léon Brillouin, CEN-Saclay, 91191 Gif-sur-Yvette CEDEX, France*

(*Received* 28 *October* 1987; *accepted* 4 *January* 1988)

Abstract

Fractal structures are characterized by self similarity within some spatial range. The mass distribution in a fractal object varies with a power D of the length R, smaller than the dimension d of the space. When the range of physical interest falls below 1000 Å, scattering techniques are the most appropriate way to study fractal structures and determine their fractal dimension D. Small-angle neutron scattering (SANS) is particularly useful when advantage can be taken of isotopic substitution. It is easy to show that the scattering law for a fractal object is given by $S(Q) \sim Q^{-D}$, where Q is the magnitude of the scattering vector. However, in practice some precautions must be taken because, near the limits of the fractal range, there are important deviations from this simple law. Some relations are derived which can be applied in relatively general situations, such as aggregation and gelation. The effects of polydispersity, important, in particular, in situations described by percolation models, are also shown.

Introduction

Since its introduction by Mandelbrot (1977), the concept of fractals has been used in many situations and systems, such as aggregates and gels. The fractal dimension very often summarizes and averages over very complex structural details. In physics this kind of description is useful if some physical property can be related to the fractal dimension. This is, for example, the case for aggregation, where different models, such as diffusion-limited aggregation (Witten & Sander, 1983), predict a well defined fractal dimension. However, the determination of the fractal dimension is not always easy, and some precautions must be taken when analysing experimental data.

Theory

For the purpose of this paper, a fractal object can be described by two properties. The first one is self similarity, which means that a detail of the fractal object is structurally identical to the whole or, in other words, that the structure of the object is independent of the characteristic length scale of observation. It is clear that such a situation will break down at some scale in a real experiment. This means that, in the real world, an object can be considered as a fractal object and be described by a fractal dimension only within some spatial range, covering at least one decade. Near the borders of the fractal domain the ideal scattering law of the fractal object will no longer be obeyed and a specific treatment of the system cannot be avoided.

The second property which characterizes the fractal object is its fractal or Hausdorff dimension, D (Mandelbrot, 1977), defined as the exponent of the linear dimension R in the relation $M(R) \sim (R/r_0)^D$ where M represents the mass and r_0 is the gauge of measurement. The exponent D characterizes mass fractals. It is smaller than the dimension d of the space where the fractal object is embedded.

The concept of fractal dimension can easily be generalized to fractal surfaces. The fractal surface dimension D_s relates the measure of the surface and the linear length. Its limits are $d-1$ and d.

In computer simulations, fractal objects are generated and their dimensions are determined from images in real space or their projections in a two-dimensional space, *e.g.* on photographs. If the simulation is performed in three dimensions, the fractal dimension is conserved in the projection if it is smaller than 2 (Weitz & Oliveria, 1984). Real experiments have been analysed as well in this way. The statistics of such a technique is in general poor. Conversely, scattering techniques, because of averaging in reciprocal space, are the appropriate way to determine a structure. This statement applies of course to fractal structures and some review papers have been devoted recently to the subject (Teixeira, 1986; Martin & Hurd, 1987).

Because the fractal structure never extends below the atomic separation, evaluations of fractal dimensions by scattering techniques concern small scattering vectors Q, say below 0·5 Å^{-1}. In a small-Q experiment the sample is analysed with a spatial resolution of the order of $2\pi/Q$. Typical values for Q in a small-angle neutron scattering (SANS) experiment extend from 10^{-3} to 1 Å^{-1}. Consequently, the fractal structure is easily observed by SANS if self similarity holds in some spatial range below 1000 Å.

* Laboratoire commun CEA-CNRS.

0021-8898 88 060781-05$03.00

experimental range the scattering law is particularly easy to derive. Actually, from the mass distribution $M(R) \sim R^D$, one obtains the density distribution $\rho \sim R^{D-d}$ (which goes to zero at infinite distances) and, by Fourier transform, the scattering law $S(Q) \sim Q^{-D}$. This gives the well known straight line with slope D in a logarithmic plot of $S(Q)$. Of course, this law applies only if one remains at values of Q large enough to be independent of the non-zero density of the sample at large scales. This law also breaks down for large values of Q when one analyses the sample over length scales small enough to be sensitive either to individual scatterers (the form factor) or to the surface (Porod region).

If the individual scatterers are relatively monodisperse, the scattered intensity $I(Q)$ can be decomposed as

$$I(Q) = \Phi P(Q) \bar{S}(Q). \quad (1)$$

In this expression, $\Phi = N/V_0$, where N is the number of scatterers and V_0 the volume of the sample. Φ is a number density expressed in cm^{-3}.

$P(Q)$ is a function of the form factor $F(Q)$ which will be defined below. It depends on the spatial distribution of the scattering lengths of the atoms constituting the sample. A precise determination of $P(Q)$ is not always possible, but simple expressions can be derived for some simple geometrical shapes. In principle, one must start from the coherent scattering length b_i of each individual atom i and evaluate, from their instantaneous positions $\mathbf{r}_i$, the density

$$\rho(\mathbf{r}) = \sum_i b_i \delta(\mathbf{r} - \mathbf{r}_i). \quad (2)$$

[Because the distribution $\delta(\mathbf{r} - \mathbf{r}_i)$ has the inverse dimensions of a volume, $\rho(r)$ is expressed in cm^{-2}.]

For practical purposes, in SANS the spatial resolution is low enough to allow some spatial averaging. In this context it is useful to introduce the notion of contrast in the following way. $\rho(\mathbf{r})$ is averaged over distances small compared with $1/Q$. The medium where the fractal object is immersed (often called the solvent) is in general well represented by a single number ρ_0 because its structure cannot be observed with the resolution of the SANS experiment. Very often the particle itself is supposed to have a uniform density. The contrast is given by $\rho(\mathbf{r}) - \rho_0$. One of the important advantages of SANS is that the contrast can very often be modified by isotopic substitution which has only minor effects on the structure. This is currently used with hydrogenated samples, owing to the large differences in the scattering lengths of hydrogen and deuterium.

The form factor $F(Q)$ is the Fourier transform of the contrast evaluated over the volume of the particle and $P(Q)$ is the square of the modulus of $F(Q)$ averaged over the ensemble of particles:

$$P(Q) = \langle |F(Q)|^2 \rangle = \left\langle \left| \int_{\substack{\text{volume of} \\ \text{the particle}}} [\rho(\mathbf{r}) - \rho_0] \exp(i\mathbf{Q}.\mathbf{r})\, d\mathbf{r} \right|^2 \right\rangle \quad (3$$

[$P(Q)$ is expressed in cm^2].

For some simple shapes $P(Q)$ is easily determine (Guinier & Fournet, 1955). For example, for uniform spheres of density ρ, volume V and radius r_0,

$$P(Q) = V^2(\rho - \rho_0)^2 \times [3\sin(Qr_0) - Qr_0\cos(Qr_0)/(Qr_0)^3]^2. \quad (4$$

At large values of Q the scattered intensity become independent of the shape of the particles and i dominated by surface scattering. This is particularl true if a small polydispersity is present, as is always th case in real systems. In this domain, $P(Q)$ is given b the Porod law

$$P(Q) = 2\pi(\rho - \rho_0)^2 S/Q^4 \quad (5$$

where S is the total surface. In this derivation, th density profile is supposed to vary sharply ove distances smaller than $1/Q$. If the density profile varie less sharply, one obtains smoother Q dependence (Auvray, 1986).

The Porod law can be generalized (Bale & Schmidt 1984) to fractal surfaces of dimension D_s. Writing

$$S = (r/r_0)^{D_s} \quad (6$$

for the measurement of the fractal surface with dimension D_s, one obtains

$$P(Q) = \pi(\rho - \rho_0)^2 S\Gamma(5 - D_s) \times \sin[\pi(D_s - 1)/2]Q^{-(6-D_s)}, \quad (7$$

which gives (5) when $D_s = 2$.

Because $6 - D_s$ falls between 3 and 4, the Q dependence of the scattering law of a fractal surface is not easily distinguishable from that of a smooth interface.

$\bar{S}(Q)$ is an effective structure factor (Chen & Bendedouch, 1985), given by

$$S(Q) = 1 + \frac{|\langle F(Q) \rangle|^2}{\langle |F(Q)|^2 \rangle}[S(Q) - 1]. \quad (8)$$

For a centrosymmetric particle $\bar{S}(Q) = S(Q)$. $S(Q)$ describes the spatial distribution of the individual scatterers. It is the Fourier transform of the pair correlation function, $g(r)$. [$g(r)$ is dimensionless.] $\Phi g(r)$ represents the probability of finding a particle at a distance r from a particle situated at the origin.

Explicitly, $S(Q)$ can be written as [see, for example, Squires (1978)]

$$S(Q) = 1 + \Phi \int [g(r) - 1] \exp(i\mathbf{Q}.\mathbf{r})\, d\mathbf{r}. \quad (9)$$

For isotropic systems

$$S(Q) = 1 + 4\pi\Phi \int_0^\infty [g(r) - 1] r^2 \sin(Qr)/Qr \, dr. \quad (10)$$

If the individual scatterers are sufficiently far apart (dilute system), $S(Q)$ reduces to unity and the total scattered intensity depends only on the form factor. Whenever possible, dilute systems are used to determine $P(Q)$.

Above some concentration, the individual scattering objects can no longer be seen as isolated. There will be at least a steric effect. In situations where there are, moreover, interparticle interactions, such as in systems containing charged particles, structural effects can appear even at extremely low concentrations, avoiding the direct determination of $P(Q)$. Methods have been derived to evaluate the structure factor in such situations (Guinier & Fournet, 1955).

The structure factor $S(Q)$ very often has a liquid-like shape with one or more oscillations, and goes necessarily to unity at large Q. It is unfortunately frequent practice, in the difficult interpretation of $S(Q)$, that a physical significance is attributed to the position of the first structural peak. Such a procedure is incorrect, because the structure factor is the Fourier transform of a pair correlation function. The first structural peak cannot in general be associated with some enlarged Bragg peak, as in a disordered solid material. At most, its position will give the order of magnitude of some characteristic distance in the sample. Because the measured Q range in a typical SANS experiment does not allow the evaluation of the Fourier integral, the determination of $g(r)$ must start from a plausible model able to reconstitute the measured scattering function.

For a fractal object, the structure factor $S(Q)$ can be derived in the following way. From the meaning of $g(r)$, the total number of particles within a sphere of radius r centred in a central particle is given (for $d = 3$) by

$$N(r) = \Phi \int_0^r g(r) 4\pi r^2 \, dr \quad (11)$$

or

$$dN(r) = \Phi g(r) 4\pi r^2 \, dr. \quad (12)$$

On the other hand, a fractal object is characterized by a spatial distribution of the individual scatterers given by

$$N(r) = (r/r_0)^D, \quad (13)$$

where r_0 is the gauge of the measurement, which has the magnitude of the characteristic dimension of each individual scatterer.

Differentiation of (13) and identification with (12) gives

$$\Phi g(r) = (D/4\pi r_0^D) r^{D-3}. \quad (14)$$

Because D is smaller than 3, $g(r)$ goes to zero at large r, as we have seen above. This is clearly unphysical. At some large scale, the sample will show a macroscopic density. A good knowledge of the sample allows in general a reasonable assumption for the large-scale behaviour of $g(r)$. We will adopt here a procedure first introduced by Sinha, Freltoft & Kjems (1984), which proved to be very useful, even if not absolutely general. It involves an expression of the form $\exp(-r/\xi)$, where ξ is a cut-off distance, to describe the behaviour of the pair correlation function at large distances. To derive the analytical form of $S(Q)$ within this assumption, one can use the general theory of liquids, where the uniform density is subtracted to avoid a divergence in the evaluation of $S(Q)$ (Chen & Teixeira, 1986; Teixeira, 1986). We then write

$$\Phi[g(r) - 1] = (D/4\pi r_0^D) r^{D-3} \exp(-r/\xi). \quad (15)$$

The introduction of the cut-off distance ξ is done in analogy with the Ornstein–Zernike treatment of critical phenomena (Stanley, 1971), which is represented by (15) with $D = 2$.

The meaning of ξ is only qualitative and has to be made precise in any particular situation. Generally speaking, it represents the characteristic distance above which the mass distribution in the sample is no longer described by the fractal law. In practice, it can represent the size of an aggregate or a correlation length in a disordered material.

Fourier transformation of (15) gives, in accordance with (10),

$$S(Q) = 1 + \frac{D}{r_0^D} \int_0^\infty r^{D-1} \exp(-r/\xi) \frac{\sin(Qr)}{Qr} \, dr$$

$$= 1 + \frac{1}{(Qr_0)^D} \frac{D\Gamma(D-1)}{[1 + 1/(Q^2\xi^2)]^{(D-1)/2}} \times \sin[(D-1)\tan^{-1}(Q\xi)] \quad (16)$$

where $\Gamma(x)$ is the gamma function of argument x.

This expression reduces of course to $S(Q) \sim Q^{-D}$ when $\xi^{-1} < Q < r_0^{-1}$. Expressions (1), (3) to (7) and (16) have been used with success to fit experimental data in many different situations. As an example, we give in Fig. 1 the scattered intensity from different samples of silica aerogel and their fit by the preceding equations (Courtens & Vacher, 1987).

The unity term in $S(Q)$ becomes dominant at large Q. Then, the scattered intensity $I(Q)$ is dominated by the form factor $P(Q)$ [see (1)]. By contrast, at small values of Q the intensity $I(Q)$ is dominated by $S(Q)$ and for $Q \ll \xi^{-1}$ has the generalized Guinier-type behaviour

$$\lim_{Q \to 0} S(Q) = \Gamma(D+1)(\xi/r_0)^D \times \{1 - [D(D+1)/6]Q^2\xi^2\}. \quad (17)$$

comparison of this expression with Guinier's law shows that ξ is related to a generalized radius of gyration R_g by

$$R_g^2 = D(D+1)\xi^2/2.$$

In a general way, $S(Q)$ can be considered as the form factor of an ensemble of fractal objects distributed at a larger scale in the space.

Polydispersity

A particular situation is that of gelation processes described by percolation models (Stauffer, 1976; de Gennes, 1979), where a large polydispersity is present. During the gelation process of branched polymers, there is a very large distribution $n(s)$ of polymers of different sizes s. This distribution is characterized (Fig. 2) by two numbers: the average size, N_w, and the maximum cut-off size, N_z.

Within the percolation theory, N_w and N_z, near the percolation threshold, are associated with the two universal exponents, γ and σ.

$$N_w \sim \varepsilon^{-\gamma} \tag{18}$$

$$N_z \sim \varepsilon^{-1/\sigma} \tag{19}$$

where ε measures the distance to percolation.

The distribution $n(s)$ has been derived by Stauffer (1985) and depends on the exponent τ:

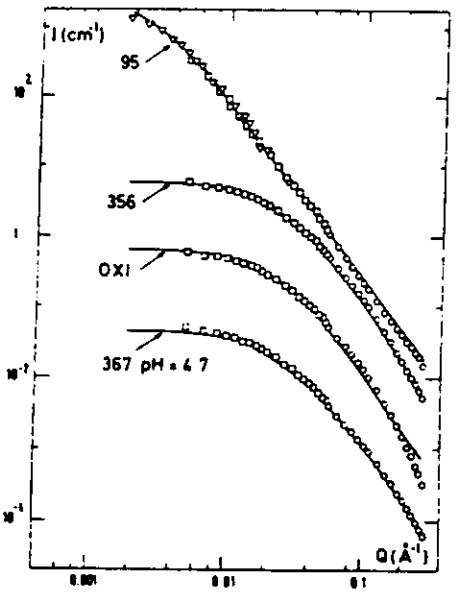

Fig. 1. Scattered intensity from several samples of silica aerogels. Numbers labelling the curves give the densities in g cm^{-3} and OXI means an oxidized sample with density equal to 356 g cm^{-3}. The sample labelled pH = 4·7 was prepared with acid catalysis. All the others are neutrally reacted samples. Solid lines represent fits with equations (1), (5) and (16). Each intensity is divided by ten compared with the previous one, starting from the top. (From Courtens & Vacher, 1987.)

$$n(s) = s^{-\tau} f_1(\varepsilon s^{\sigma}) = s^{-\tau} f_1(s/N_z), \tag{20}$$

where $f_1(x)$ is an exponentially decaying functio which accounts for the cut off of the distribution a large s.

Near the percolation threshold, each polymer has fractal structure with dimension D. The radius o gyration of each polymer can be associated with th cut-off parameter ξ. Consequently, one can write

$$s = \xi^D \tag{21}$$

where ξ is now the radius of gyration of the polymer o size s.

The pair correlation function of a single polymer containing s monomers (the individual scatterers) has the form of (15), where D is the fractal dimension of the polymer. In a more general way, one writes, instead of (15),

$$\Phi[g(r)-1] = (D/4\pi r_0^D) r^{D-3} f_2(-r/\xi)$$
$$= (D/4\pi r_0^D) r^{D-3} f_2(-r/s^{1/D}), \tag{22}$$

where we use (21). $f_2(-r/\xi)$ represents a decreasing function of r.

The scattering function of such a polymer is obtained, following the same steps as for the derivation of (16), as

$$S(s,Q) = 1 + \frac{D}{r_0^D}\int_0^{\infty} r^{D-3} f_2(-r/s^{1/D}) \frac{\sin(Qr)}{Qr}\,dr$$

$$= 1 + \frac{D}{(r_0 Q)^D} f_3(Q\xi)$$

$$= 1 + s f_4(Q^D s) \tag{23}$$

where $f_3(x)$ and $f_4(x)$ can be determined if $f_2(-r/\xi)$ is known.

The total scattering function at infinite dilution is now obtained (Martin & Ackerson, 1985; Bouchaud, Delsanti, Adam, Daoud & Durand, 1986) by summing all the contributions $S(s,Q)$ with their relative

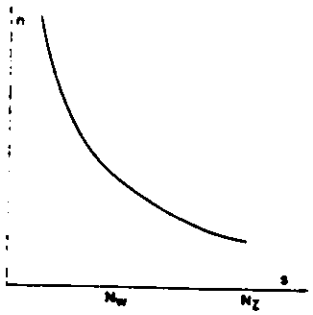

Fig. 2. Schematic representation of the number $n(s)$ of polymers with size s, near the percolation threshold. N_w and N_z are the average and the maximum size, respectively. This distribution is described by equation (20).

weights, $n(s)$, given by (20):

$$S(Q) - 1 = \int ds\, sn(s)[S(s, Q) - 1]$$
$$= \int ds\, s^2 s^{-\tau} f_1(s/N_z) f_4(Q^D s)$$
$$= Q^{-(3-\tau)D} f_5(QR_z) \quad (24)$$

where $R_z \sim N_z^{1/D}$. This result applies only for $\tau > 2$.

For large values of Q ($Q \gg R_z^{-1}$), $f_5(QR_z) \sim 1$. Comparing (16) and (24), one notices that, in the fractal region, the scattered intensity is now represented in a logarithmic plot by a straight line with a slope $(3-\tau)D$, instead of D. The theory of percolation predicts $D = 2$ and $\tau = 2{\cdot}2$. In a recent experiment Bouchaud *et al.* (1986) have measured these exponents using fractionated samples containing only the polymers of large size. In the polydisperse sample, the dependence on Q of the scattered intensity gives $(3-\tau)D = 1{\cdot}59$ and, in the fractionated sample, D is evaluated directly giving $D = 2$ (Fig. 3), in excellent agreement with the theory.

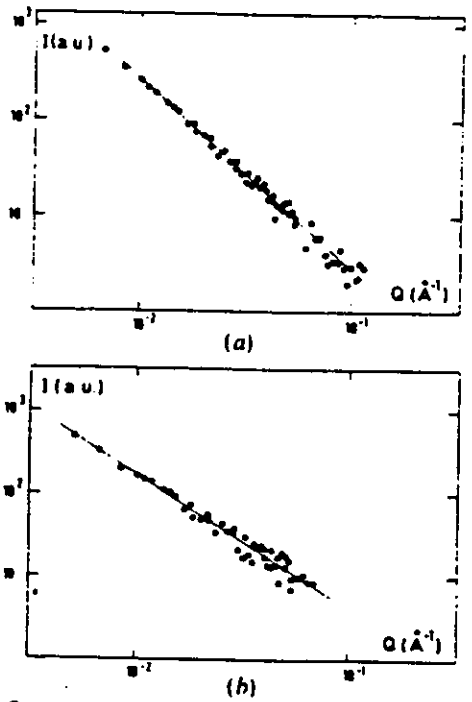

Fig. 3. (*a*) Scattered intensity by a fractionated sample containing only polymers with a large size. The slope gives $D = 1{\cdot}98$. (*b*) Scattered intensity by the dilute polydisperse sample. The slope gives $D(3-\tau) = 1{\cdot}59$. (From Bouchaud *et al.* 1986.)

These results show that fractal concepts are useful in interpreting complex situations in disordered materials and are the most convenient method for studying physical phenomena such as aggregation and gelation. Scattering techniques and SANS, in particular, appear to be the most appropriate technique for the determination of the fractal dimension. We have summarized some simple and relatively general expressions which can be derived to describe the intensity scattered by fractal objects.

References

AUVRAY, L. (1986). *C. R. Acad. Sci.* **302**, 859–862.

BALE, H. D. & SCHMIDT, P. W. (1984). *Phys. Rev. Lett.* **53**, 596–599.

BOUCHAUD, E., DELSANTI, M., ADAM, M., DAOUD, M. & DURAND, D. (1986). *J. Phys. (Paris)*, **47**, 1273–1277.

CHEN, S.-H. & BENDEDOUCH, D. (1985). In *Enzyme Structure, Method in Enzymology*, edited by C. H. W. HIRS & S. N. TOMASHEFF. New York: Academic Press.

CHEN, S.-H. & TEIXEIRA, J. (1986). *Phys. Rev. Lett.* **57**, 2583–2586.

COURTENS, E. & VACHER, R. (1987). *Z. Phys. B*, **68**, 355–361.

GENNES, P. G. DE (1979). *Scaling Concepts in Polymer Physics*. Cornell Univ. Press.

GUINIER, A. & FOURNET, G. (1955). *Small-Angle Scattering of X-rays*. New York: Wiley.

MANDELBROT, B. B. (1977). *Fractals, Form and Dimension*. San Francisco: Freeman.

MARTIN, J. E. & ACKERSON, B. J. (1985). *Phys. Rev. A*, **31**, 1180–1182.

MARTIN, J. E. & HURD, A. J. (1987). *J. Appl. Cryst.* **20**, 61–78.

SINHA, S. K., FRELTOFT, T. & KJEMS, J. (1984). In *Kinetics of Aggregation and Gelation*, edited by F. FAMILY & D. P. LANDAU, pp. 87–90. Amsterdam: North Holland.

SQUIRES, G. L. (1978). *Introduction to the Theory of Thermal Neutron Scattering*. Cambridge Univ. Press.

STANLEY, H. E. (1971). *Introduction to Phase Transitions and Critical Phenomena*. Oxford: Clarendon Press.

STAUFFER, D. (1976). *J. Chem. Soc. Faraday Trans.* 2, **72**, 1354–1364.

STAUFFER, D. (1985). *Introduction to Percolation Theory*. London: Taylor & Francis.

TEIXEIRA, J. (1986). In *On Growth and Form*, edited by H. E. STANLEY & N. OSTROWSKY, pp. 145–162. Dordrecht: Nijhoff.

WEITZ, D. A. & OLIVERIA, M. (1984). *Phys. Rev. Lett.* **52**, 1433–1436.

WITTEN, T. A. & SANDER, L. M. (1983). *Phys. Rev. B*, **27**, 5686–5697.

Journal of Non-Crystalline Solids 147&148 (1992) 206–212
North-Holland

NON-CRYSTALLINE SOLIDS

Ultrastructural evolution during gelation of TiO_2–SiO_2 sols

M. Ramírez-del-Solar [a], L. Esquivias [a], A.F. Craievich [b] and J. Zarzycki [c]

[a] *Department of Structure and Properties of the Materials, University of Cádiz, Apdo. 40, Puerto Real 11510, Cádiz, Spain*
[b] *Laboratorio Nacional de Luz Sincrotron / CNPq, Campinas, SP, Brazil and Instituto de Física / USP, Sao Paulo, Brazil*
[c] *Laboratory of Science of Vitreous Materials (LA1119), University of Montpellier II, 34060 Montpellier cedex, France*

Small angle X-ray scattering was used to examine in situ formation of mixed TiO_2–SiO_2 gels. In order to elaborate the homogeneous solution, either ultrasonic radiation or alcoholic dilution of the precursors was carried out. The evolution of the typical sizes calculated at low and high q-regions were correlated. This lead to an approximate model for the aggregation process. The fit of the experimental data to a simple growth law was attempted allowing a kinetic rate constant to be estimated. This permits the evaluation of the differences induced in titanium doped silica sono- and classic gels.

1. Introduction

The sol–gel process is frequently applied to synthesize ceramics and glasses of a great variety of systems. In order to facilitate the control of final material properties, an integrated study of the different aggregation states from the initial colloidal solution is essential. In previous papers [1–3], the physico-chemical and structural characteristics of sonogels were compared with those of standard gels obtained with alcoholic dilution. These studies were undertaken after the gel point, but a complete investigation of this mechanism requires investigation of the 'sonosol to sonogel' transition.

Analysis of a gelling solution needs an 'in situ' method such as NMR, vibrational spectroscopy or small angle scattering. Small angle X-ray scattering (SAXS) was used to probe the structure and growth kinetics of the macromolecular networks of pure and titania-doped silica sono- and classic sols before gelation. This technique measures the angular dependence of the intensity scattered by a sample with heterogeneities in electron density. At low angles, the scattered intensity from isolated aggregates can be approximated by Guinier's law [4]:

$$I(q) = I(0)\exp\left(-\frac{Rg^2q^2}{3}\right), \qquad (1)$$

where $I(0)$ is the extrapolated intensity to $q = 0$, R_g is the radius of gyration of the aggregates and $q = (4\pi/\lambda)\sin(\theta/2)$ is the modulus of the scattering vector; λ and θ are the X-ray wavelength and scattering angle, respectively. Analysis of this region of the scattering curves and their time evolution provides information about the overall size and mechanism of cluster growth [5]. The asymptotic behaviour, for large q, is described by Porod's law ($I \sim q^{-4}$) provided the system has sharp interfaces [4]. If aggregates are mass fractals, the intermediate q-range exhibits a potential dependence [6]:

$$I(q) \propto q^{-x}, \qquad (2)$$

where x is the fractal dimension (D), which can be determined from the linear part of a log I versus log q plot. A crossover between these two domains and the asymptotic (Porod) q-region are usually observed. This crossover, located at $q \sim q_m$, defines a parameter, R', corresponding to the size of the primary particles which comprise the fractal aggregate ($R' = 1/q_m$).

3. Structural features

Figures 1(a) and (b) show representative sets of curves obtained at different aggregation times for 5% TiO_2 sols. The overall behaviour of SAXS curves indicates an increase of the q-range showing a power–law decay with aggregation. Close to the gel point ($t/t_g \approx 1$), most of the curve domain is consistent with a q power–law. The calculated slopes related to internal structure of aggregates indicate that the local geometric structure is unchanged during the sol–gel transition [4]. The linearity of the log I versus log q plots for a wide q-domain is consistent with the behaviour ex-

Table 1
Several characteristic parameters measured for both series of sono- and classic solutions

X	t_g (min)	D	D'	$R_g(t_g)$ (Å)
0S	390	1.82	–	17
1S	105	1.92	1.73	22
5S	30	1.99	1.88	45
0C	1800	1.73	–	58
1C	300	1.90	–	109
5C	140	1.93	1.75	41

Gelation time at 60°C, dimensionalities calculated from final slope of fresh gel scattering curves, those averaged during the aggregation process from $I(0) = f(R_g)$ dependence and gyration radius of fresh gels.

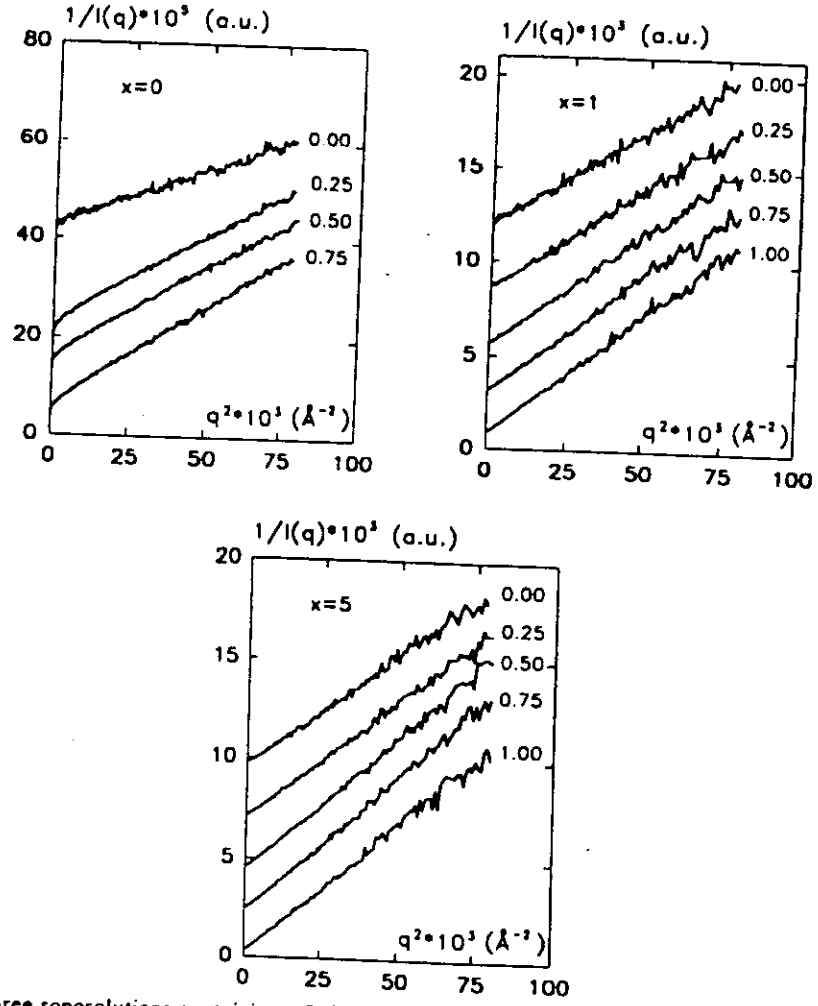

Fig. 2. Zimm plots for three sonosolutions containing x% TiO_2 and for the t/t_g values indicated on each right side. (Curves have been vertically displaced the same relative distance for a more clear visualization.)

2. Experimental

2.1. Sample preparation

Gels of the composition $xTiO_2$–$(100-x)SiO_2$ were made by mixing solutions of oxides precursors tetraethoxysilane (TEOS) and tetrabutylorthotanate (TBOT). The chemical reactions were carried out under acidic conditions with pH[HCl] = 1.5. The classic hydrolysis of TEOS is accomplished by stoichiometric additions of water (4 mol/mol alkoxide) in an alcoholic (EtOH) environment, under magnetical stirring, while in the sonocatalytic method the solventless TEOS–water mixture is subjected to ultrasonic radiation [3].

In both cases, once the solutions were cooled to 0°C, appropriate volumes of a titanium precursor solution TBOT : AcOH : nBuOH (1 : 5.5 : 3.5), in which AcH behaves as titanium alkoxide chemical modifier, were added under vigorous stirring to obtain different compositions. Sono- and classic mixed solutions are labelled as xSm and xCm, respectively, x being 0, 1 or 5 (the nominal TiO_2 molar content) and m corresponds to the relative t/t_g time where t_g is the gelation time.

2.2. Small angle X-ray scattering

Small angle X-ray scattering measurements were performed at the small angle scattering station of the synchrotron radiation laboratory LURE, Orsay, France, using a pin-hole collimated X-ray beam. A suitable wavelength was selected ($\lambda = 1.4$ Å) using a Ge(111) bent monochromator. For the SAXS experiments, the solutions were poured into a bronze cell between two Mylar windows. The sample thickness, t, was chosen to be $t = 1/\mu$, μ being the linear absorption coefficient, in order to obtain the maximum in the scattered intensity [4]. The cell was placed in a thermostated block maintained at 60°C during the aggregation and gelation processes. Recording of scattered intensities at fixed intervals provides useful information that can be correlated with the evolution of microstructure. The gelation time, t_g, of the solutions was previously measured in similar cells, for each composition in the same conditions (table 1).

The scattered X-ray intensities were recorded as a function of scattering angle using a one-dimension position-sensitive detector. Parasitic scattering was measured using a blank sample with an empty cell. For samples with a faster gelation kinetics (5S, 5C and 1S), the spectra were obtained continuously with acquisition times ranging from 3 to 5 min. For the slower ones, data were taken at various intervals, depending on the sample, with counting times of 5 min.

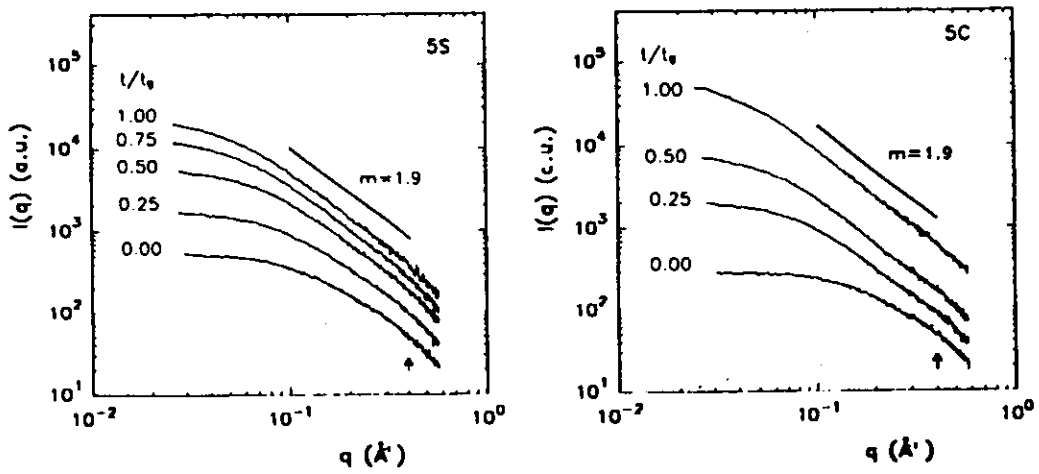

Fig. 1. Development of the scattering profiles for sono- and classic $5TiO_2$–$95SiO_2$ solutions at different stages of polymerization. Notice the change of the final slope of the curves at the high q-region indicated. (Curves have been vertically displaced the same relative distance for a more clear visualization.)

pected for mass fractal structures. This linearity extends to a maximum q_m value at which a crossover is theoretically expected. This behaviour is associated with the size, R', of the primary particles by $R' = 1/q_m$. The experimental curves yield $R' \approx 2.5$ Å.

As aggregation proceeds, clusters become much larger than monomers, causing a widening of the linear domain of the log–log curves. Thus, more precise linear regressions are found from the scattering intensity plots corresponding to fresh gels of all compositions. The effect of titanium on the SiO_2 structure produces an increase in the exponent x of eq. (2) (table 1) and, consequently, in the fractal dimensionality, D. This suggests a more compact network occurs with increasing TiO_2 content. However, comparisons between these D-values must be made with care because of small differences in the aging time of each gel.

Since a saturation of the scattered intensity at low q is observed, an analysis of this region on the basis of the Guinier approximation (eq. (1)) was attempted. However, owing to the limited approximation validity ($qR_g \ll 1$), linear regressions in the log $I(q) - q^2$ plots are only possible at early stages in the reaction and within a narrow q-range. The variation in the scattered experimental intensities at low q was fitted using the Zimm approximation which holds for polymeric-ball like particles. Better agreement was observed with the Zimm equation [7]:

$$\frac{1}{I(q)} = \frac{1}{I(0)}\left[\left(1 + \frac{q^2 R_g^2}{3}\right)\right] \qquad (3)$$

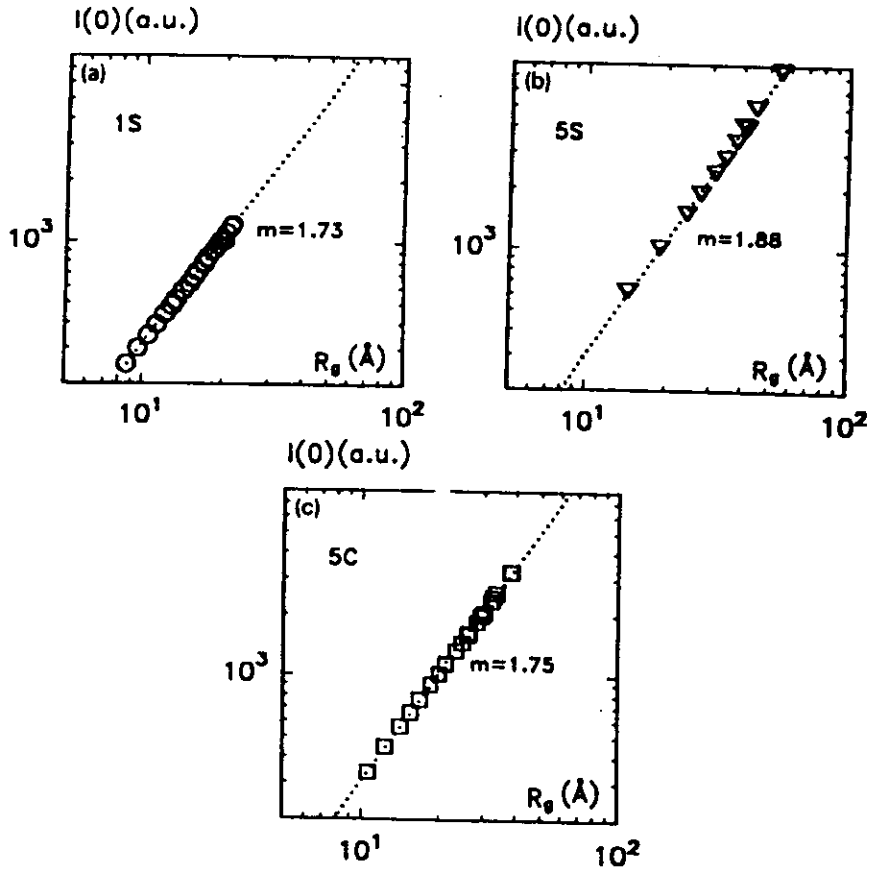

Fig. 3. Variation of the extrapolated intensity, $I(0)$, with the average radius of gyration, R_g.

and $I(0)$ and R_g can be evaluated from the wide linear regions in fig. 2 for the three sonosolutions.

Logarithmic plots of $I(0)$ versus R_g values provide additional information about solution structure. This analysis has been made for samples with a gelation times that permit continuous study in situ. Figure 3 data show the evolution of $I(0)$, which is proportional to the aggregate mass, as a function of their average size parameter, R_g. These log–log plots should display linear behaviour when the extrapolated SAXS intensity, $I(0)$, is related to R_g by [4]

$$I(0) \propto R_g^D. \tag{4}$$

This equation applied to growing mass fractal objects. The slopes of fig. 3 plots indicate the presence of slightly branched polymeric clusters [8], in agreement with the previous results. The dimensionality, D, calculated from the slopes of log I versus log q plots for fresh gels are a little higher than D' determined from log $I(0)$ versus log R_g plots. The last ones (D') are average values during cluster growth. So, differences between D and D' indicate that fractal dimensionality increases during aggregation, suggesting that a restructuring process is also acting. Dimensionalities are expected to be higher in processes involving restructuring than in those involving only pure aggregation [9].

In order to obtain further details of the aggregation process, the evolution of the integral invariant, Q_0, was determined. This integral parameter, when applied to a 'two-density' material, is related to its structure by [4]

$$Q_0 = \int_0^\infty I(q) q^2 \, dq = 2\pi^2 (\Delta\rho)^2 \phi(1-\phi) V, \tag{5}$$

where $\Delta\rho$ is the difference in electronic density between the phases, ϕ is the volume fraction of one of the phases and V is the irradiated volume.

For evaluation of eq. (5), appropriate extrapolations for $q \to 0$ and $q \to \infty$ must be done [10]. For $q \to 0$, the extrapolation is easily accomplished using Zimm plots. For $\theta \to \infty$, it is assumed that, after the crossover found, the SAXS intensity for $q > q_{max}$ (q_{max} being the maximum q-value for which the intensity was recorded) exhibits a Porod behaviour [4], i.e., $I(q)q^4 = k_p$, k_p being a constant. The contribution of the Porod's region is small for all the experimental curves except those corresponding to very short reaction time.

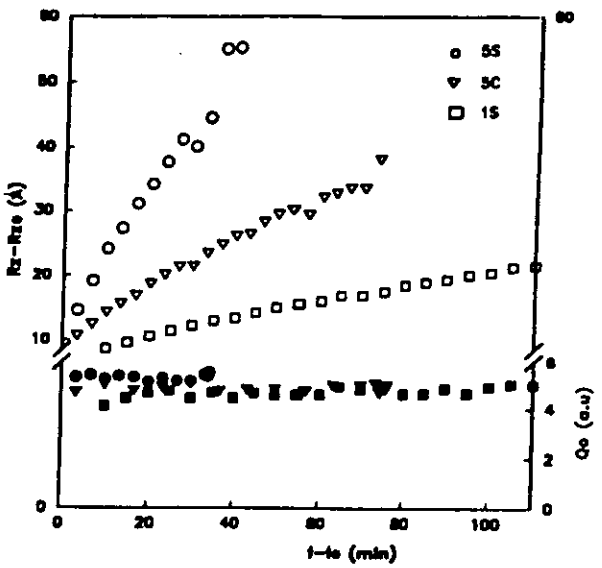

Fig. 4. Evolution during gelation time of the gyration radius calculated from Zimm plots (open symbols) and the integral invariant (filled symbols).

The integral invariant, Q_0, was calculated from the curves measured in a larger q-domain (5c, 5s and 1s), for which a reasonable extrapolation, beyond the experimental q-range is possible. The integral values, which are plotted in fig. 4, do not vary noticeably during aggregation and, hence, the total volume fraction of the scatterers is also constant. Gelation of these solutions is concluded to occur by a cluster–cluster aggregation process.

The surface/volume ratio of the scatterers can be determined as the ratio K_p/Q_0, but a particular geometry should be assumed in order to estimate their characteristic dimension. In this sense, attention must be paid to the fact that there is no evolution with time of the V/S ratio. Consequently, we can rule out the formation of spherical particles (or voids), the growth of which would imply an increase of this parameter as R_g does. It seems more appropriate to describe the internal structure on the basis of rod-like scatterers which lengthen with an essentially constant cross-section.

4. Kinetic of aggregation

The evolution of the correlation length, R_g, calculated at the lower angles, i.e., larger distances, is apparent in fig. 4. It is clear that the wide angular domain explored makes accessible two characteristic dimensions (R_g and R') of the system which allow a more detailed investigation. A tentative model of the growing clusters, which is consistent with the above structural considerations and this behaviour, is represented in fig. 5. In such polymeric-like clusters, the cross-dimension, R', of the elementary particles (or voids) remains unchanged, at least on gelation, while there is aggregation due to their lengthening which generate clusters with rising size, R_g. The increase in the fractal dimension indicates that internal restructuring and, probably, coalescence of the filaments occurs, leading to densification during aging.

The time evolution of the clusters size can usually be described on the basis of a growth law [11]:

$$R_g - (R_g)_0 = K(t - t_0)^{\alpha}. \qquad (6)$$

Log–log plots of the gyration radius versus time permit estimation of the kinetic rate constant of the process, K, and the constant α. Figure 6 presents results on systems analyzed which fit this law. The K-values confirm that both the increase of the TiO_2 content and the supply of ultrasound increases aggregation rate. The constant α is the same for all samples. This would indicate that the aggregation mechanism does not change with composition. In a simple aggregation model we expect $\alpha = 1/D$. The value of D obtained from fig. 6 plots ($D \approx 1.2$) is much slower than that obtained using the log–log and $I(0)$ versus R_g plots. Therefore we conclude that the approximation $\alpha = 1/D$ does not apply to the system studied.

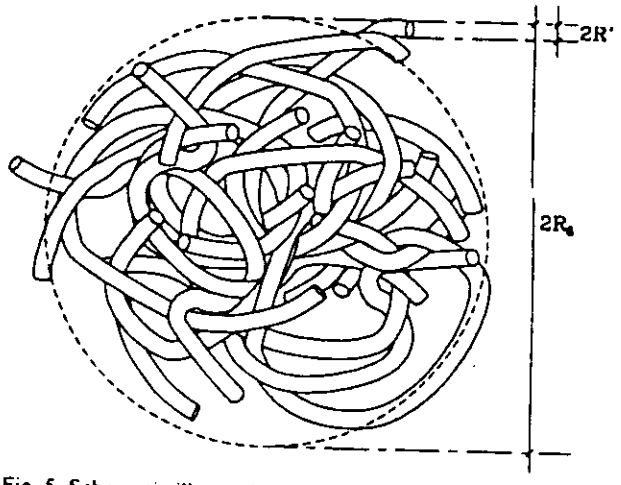

Fig. 5. Schematic illustration of the model proposed for mixed titania–silica gelling systems.

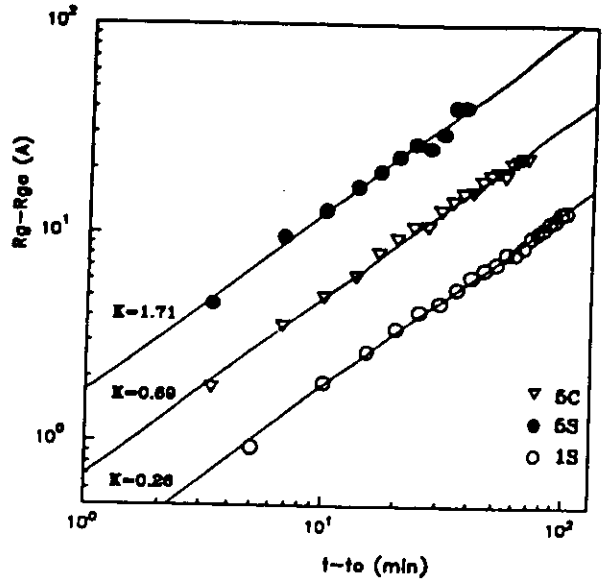

Fig. 6. Fitting of the time dependence of the gyration radius before the gel point to a law of growth like $\log[R_g - R_g(0)] = \log K + 1/D \log t$. Notice the augmentation of the extrapolated value ($\log K$) when increasing x and ultrasounds are applied.

5. Conclusion

This SAXS study of titania-doped sono- and classic silica sols reveals that the local geometric structure of aggregates remains unchanged during gelation. Analysis provides the kinetics of two characteristic scatterer length from which a structural model can be inferred. This model is consistent with the mass fractal growth behaviour de-

duced from the time evolution of the scattering profiles.

The evolution was described on the basis of a simple growth law that allows estimation of the process rate constant. The values obtained confirm that both the increase of TiO_2 content and ultrasound accelerate aggregation.

The authors gratefully acknowledge the assistance of Dr de la Rosa-Fox in computational calculations and Mr J. González in graphic designs. This work has been supported by Plan Nacional F.P.I. (Spain) and CNPq (Brazil).

References

[1] L. Esquivias and J. Zarzycki, in: Ultrastructure Processing of Advanced Ceramics, ed. J.D. Mackenzie and D.R. Ulrich (Wiley, New York, 1987) p. 255.

[2] J. Zarzycki, in: 4th Int. Conf. on Ultrastructure Processing of Ceramics, Glasses and Composites, Tucson AZ, 1989.

[3] M. Ramírez del Solar, N. de la Rosa-Fox, L. Esquivias and J. Zarzycki, J. Non-Cryst. Solids 121 (1990) 84.

[4] O. Glatter and O. Kratky, Small Angle X-Ray Scattering (Academic Press, New York, 1982).

[5] D.W. Schaefer and K.D. Keefer, Phys. Rev. Lett. 53 (1984) 1383.

[6] D.W. Schaefer, Mater. Res. Soc. Bull. 8 (1988) 22.

[7] B.H. Zimm, J. Chem. Phys. 16 (1948) 1093.

[8] C.J. Brinker, K.D. Keefer, D.W. Schaefer, R.A. Assink, B.D. Kay and C.S. Ashley, J. Non-Cryst. Solids 63 (1984) 45.

[9] R. Jullien and R. Botet, Aggregation and Fractal Aggregates (World Scientific, Singapore, 1987).

[10] M. Ramírez-del-Solar, PhD thesis, University of Cádiz (1990).

[11] T. Lours, J. Zarzycki, A. Craievich, D.J. Dos Santos and M. Aegerter, J. Non-Cryst. Solids 100 (1988) 207.

Thus, we have chosen to study borate glasses since they are nearly ideally isotropic systems for which the time and length scales are easily accessible by means of SAXS experiments. Our experiments were carried out using high-intensity x-ray radiation from a synchrotron source in pinhole collimation, thus avoiding corrections of the measured intensity and allowing accurate intensity measurements at relatively high angles. Isothermal annealing of the glass samples was performed *in situ*.

Throughout this work we use the first moment of the structure function $q_1(t)$ as a measure of the inverse of the real-space characteristic length $R(t)$. However, scaling was also tested by means of the procedure recently outlined by Fratzl *et al.*[6] This procedure is based on a global fitting of the structure function and it does not require the calculation of the first moment q_1 or the determination of q_m. We also investigated the validity of several relations implied by the scaling laws between the moments of $S(q,t)$, and between the maximum of the structure function S_m and its location q_m in reciprocal space.

The remaining sections of the paper are organized as follows. In Sec. II we summarize the procedures used in the preparation of the samples together with a description of the SAXS experimental setup. A brief account of the scaling laws is given in Sec. III, and the experimental results are presented in Sec. IV. A discussion of our results together with some concluding remarks are given in Sec. V.

II. EXPERIMENTAL PROCEDURES

The glass samples were prepared from reagent-grade HBO_3, PbO, and Al_2O_3. The batches were melted in a platinum crucible and homogenized by stirring at 1200 °C for several hours. Platelike samples with essentially homogeneous composition were obtained directly from the melt using the splat-cooling technique. The resulting lamellae were approximately 100 μ thick, which is close to the optimum thickness for SAXS experiments.

A specially designed high-temperature cell, stable to within ± 1 °C,[14] was used for *in situ* isothermal treatment of the glass samples during SAXS measurements. The kinetics of phase separation was investigated at several temperatures for two different compositions: Composition S (B_2O_3, 80 wt.%; PbO, 15 wt.%; Al_2O_3, 5 wt.%) and composition N (B_2O_3, 64 wt.%; PbO, 27 wt.%; Al_2O_3, 9 wt. %). Both compositions are indicated in the experimental phase diagram (solid lines) shown in Fig. 1.[15] A schematic plot of the spinodal (dashed lines), as estimated by Zarzycki and Naudin,[15] is also shown in Fig. 1. Thus, compositions S and N should fall, respectively, inside the classical "spinodal" and "nucleation and growth" regions of the phase diagram.

The SAXS experiments were carried out using synchrotron radiation from the DCI positron storage ring at Laboratoire pour l'Utilisation de Rayonnement Electromagnétique (LURE) (Orsay). SAXS profiles were recorded a few seconds after the samples were placed in the high-temperature cell. The recording time, of approximately 100 sec, was kept shorter than the time between measurements.

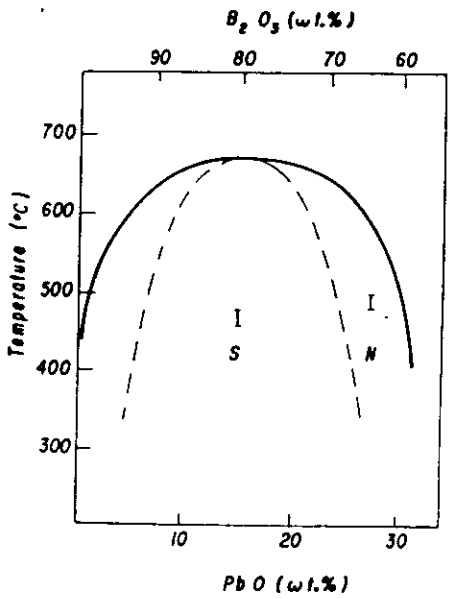

FIG. 1. Miscibility gap for the quasibinary B_2O_3-PbO-Al_2O_3 glass system, from Ref. 15. The continuous line corresponds to the solubility limit and the dashed line is the classical spinodal. The bars S and N indicate the composition and temperature range investigated in this work.

The station for small-angle experiments at LURE provides an incoming white beam horizontally focused and monochromatized by a bent, asymetrically cut germanium (111) crystal. In this investigation we used a wavelength of $\lambda = 1.380$ Å. The scattering profiles were recorded using a one-dimensional position sensitive proportional counter of resistive cathode type. The counter had an energy resolution of 20%, which is sufficient to remove the harmonics from the beam.

Two sets of slits were used to define a pinhole collimated beam. An ionization chamber placed before the sample was used to monitor the intensity decay of the incoming beam and the corresponding correction was applied to all experimental intensities. The SAXS intensities were also corrected for inhomogeneities in the position sensitive detector, the response of which was determined using an isotropic Fe^{55} source. Air scattering was measured without the glass sample in the experimental setup and subsequently subtracted from the SAXS intensities, properly attenuated by the sample absorption. The SAXS intensities were represented as functions of the modulus of the scattering vector q, which is given by $q = 4\pi \sin(\theta)/\lambda$, with θ half the scattering angle and λ the x-ray wavelength. The cross section of the incident beam corresponds to a resolution in reciprocal space $\Delta q \approx 10^{-3}$ Å^{-1}. The beam geometry used in this work tend to improve the accuracy of the experimental results since it allows us to avoid the deconvolution of the measured intensities. This latter step is necessary when linear collimation is used.

III. SCALING OF THE STRUCTURE FUNCTION

A direct experimental check on theoretical models for the kinetics of phase separation may be obtained from the

Phase separation and dynamical scaling in borate glasses

A. F. Craievich
Centro Brasileiro de Pesquisas Fisicas, Conselho Nacional de Desenvolvimento Científico e Tecnológico (CNPq), 22290 Rio de Janeiro, Rio de Janeiro, Brazil

J. M. Sanchez
Henry Krumb School of Mines, Columbia University, New York, New York 10027

C. E. Williams
Laboratoire pour l'Utilisation du Rayonnement Electromagnétique, Université de Paris—Sud, 91405 Orsay Cédex, France
(Received 12 March 1986)

Quasibinary B_2O_3-PbO-(Al_2O_3) glasses of two different compositions and at several temperatures inside the miscibility gap were investigated using small-angle x-ray scattering. Measurements were carried out using an x-ray beam from a synchrotron source in pinhole collimation and the samples were isothermally annealed *in situ*. The experimentally determined structure function was found to be in general agreement with recently proposed scaling laws. The exponent for the time dependence of the characteristic scaling length was found to change from a minimum value of 0.24 to a maximum of 0.35 for, respectively, samples near the center and near the boundary of the miscibility gap. The time exponent for the maximum of the structure function was found to be nearly equal to three times the exponent of the characteristic length, as expected from the scaling laws. The scaling structure function changes appreciably with composition, becoming considerably sharper near the boundary of the miscibility gap.

I. INTRODUCTION

The existence of dynamical scaling during the last stages of phase separation in binary mixtures has recently been proposed by several investigators on the basis of phenomenological and statistical models[1–3] as well as detailed computer simulations.[4] The underlying implication of dynamical scaling is that the process of phase separation is entirely controlled by a unique characteristic length $R(t)$. The scaling hypothesis was, therefore, implicitly included in the classical coarsening theory of Lifshitz and Slyozov,[5] although, in its present form, scaling is considerably more general. For example, analysis of data generated by different experiments and by computer simulations has led Fratzl *et al.*[6] to interpret the structure function as given by the product of two universal functions.

A direct consequence of dynamical scaling is that the structure function $S(q,t)$, i.e., the Fourier transform of the composition correlation function at time t, follows a simple asymptotic behavior for large values of t. Since the time evolution of the structure function can be directly measured by small-angle diffraction techniques, the theoretical evidence for dynamical scaling has also generated renewed interest in the experimental study of phase separation in binary mixtures. In particular, dynamical scaling has recently been established, at least as a very good approximation, in liquid mixtures,[7–9] quasibinary glasses,[10] and binary alloys.[11–13]

In order to ascertain experimentally the validity of scaling, one must determine the existence of a unique real-space characteristic length $R(t)$ and, in principle, its time dependence. Most commonly, the inverse of the characteristic length is taken to be the first moment $q_1(t)$ of the structure function or, alternatively, the magnitude of the reciprocal space vector q_m corresponding to the maximum S_m of the structure function. Although both quantities provide an equally acceptable measure of the characteristic length, there are intrinsic experimental difficulties in the calculation of the moments as well as in the precise location of q_m. For example, the calculation of the first few nondivergent moments requires precise intensity measurements at large angles where the structure function is very small and thus difficult to determine accurately. On the other hand, the location of the maximum of the structure function is particularly difficult to pinpoint since q_m is sensitive to the type of collimation used for the incident beam.

In this investigation we perform a quantitative test of the scaling hypothesis using small-angle x-ray scattering (SAXS) experiments in quasibinary borate glasses for two different compositions and several temperatures. Our investigation of two different compositions is aimed at a quantitative study of the universality of the structure function recently proposed by Fratzl *et al.*[6]

Among the several items that may tend to mask the scaling (or departure from scaling) of the experimentally determined structure function is the intrinsic anisotropy of crystalline alloys. This anisotropy has been documented by Hennion *et al.*[11] in Al-Zn and was presumably also present in the other studies of crystalline systems.[12,13]

comparison of the predicted isotropic structure function $S(q,t)$ with the experimentally determined SAXS intensity $I(q,t)$, where q is the modulus of the scattering vector and t represents the total decomposition time after a rapid quench of the sample into a metastable or unstable region inside the miscibility gap.

As mentioned in the Introduction, phenomenological models and computer simulation results[1-4] suggest that, for the advanced stages of phase separation, the structure function obeys a scaling law of the form

$$S(q,t)=J(t)F(q\cdot R(t)) \tag{1}$$

with $R(t)$ the real-space characteristic length, $F(x)$ the scaling structure function, and where the scaling factor $J(t)$ can be shown to be proportional to $[R(t)]^d$, with d the dimensionality of the system. The relationship between the scaling factor $J(t)$ and the characteristic length $R(t)$ follows from the fact that the integral of the structure function $S(q,t)$ over the entire volume in reciprocal space is time independent due to the conservation of atomic species. In general, since SAXS experiments sample only a small region in reciprocal space, a time dependence of the integrated intensity is observed during the early stages of decomposition. However, the integrated SAXS intensity is expected to be time independent during the late stages of phase separation for which the final equilibrium transformed volume fraction has been essentially reached.

It is convenient to introduce the moments Q_n and the normalized moments q_n of the structure function defined by

$$Q_n(t)=\int_0^\infty S(q,t)q^n\,dq \tag{2}$$

and

$$q_n(t)=Q_n(t)/Q_0(t)\ . \tag{3}$$

With $J(t)\propto[R(t)]^d$, as required by the conservation of integrated intensity, the scaling relation (1) implies

$$Q_n(t)=[R(t)]^{(d-n-1)}F_n\ , \tag{4}$$

$$q_n(t)=[R(t)]^{-n}f_n\ , \tag{5}$$

where the time-independent constants F_n and f_n are, respectively, unnormalized and normalized moments of the scaling function $F(x)$ and are defined by equations similar to (2) and (3).

The asymptotic behavior of the characteristic length may be described by

$$R(t)\propto t^a \tag{6}$$

with the exponent a being dependent upon the microscopic mechanism of particle growth.[1-4] For example, Stauffer and Binder[1] have shown that the exponent a varies from $\frac{1}{6}$ when the controlling growth process is that of cluster coagulation to $\frac{1}{3}$ for the classical diffusion growth mechanism of Lifshitz and Slyozov.[5] Computer simulations as well as recent experimental results in alloy systems[4,11-13] appear to confirm the predictions of Stauffer and Binder.

Equations (1) and (6) imply that the maximum of the structure function $S_m=S(q_m,t)$ evolves with time as

$$S_m\propto t^{a'} \tag{7}$$

with $a'=3a$. This particular relation between a and a', together with the time independence of the second moment Q_2 of the structure function, are sensitive tests on whether or not the asymptotic scaling behavior of $S(q,t)$ has been reached. Some of the reported experimental data aimed at confirming the validity of scaling, however, do not reproduce the expected relation $a'=3a$.[11-13]

In addition to precise measurements of the SAXS intensity itself, we may also determine accurately the first and second moments $Q_1'(t)$ and $Q_2'(t)$ of $I(q,t)$. Since SAXS intensity measurements are carried out in arbitrary units, these moments differ from those of the structure function $S(q,t)$ by a time-independent factor. On the other hand,

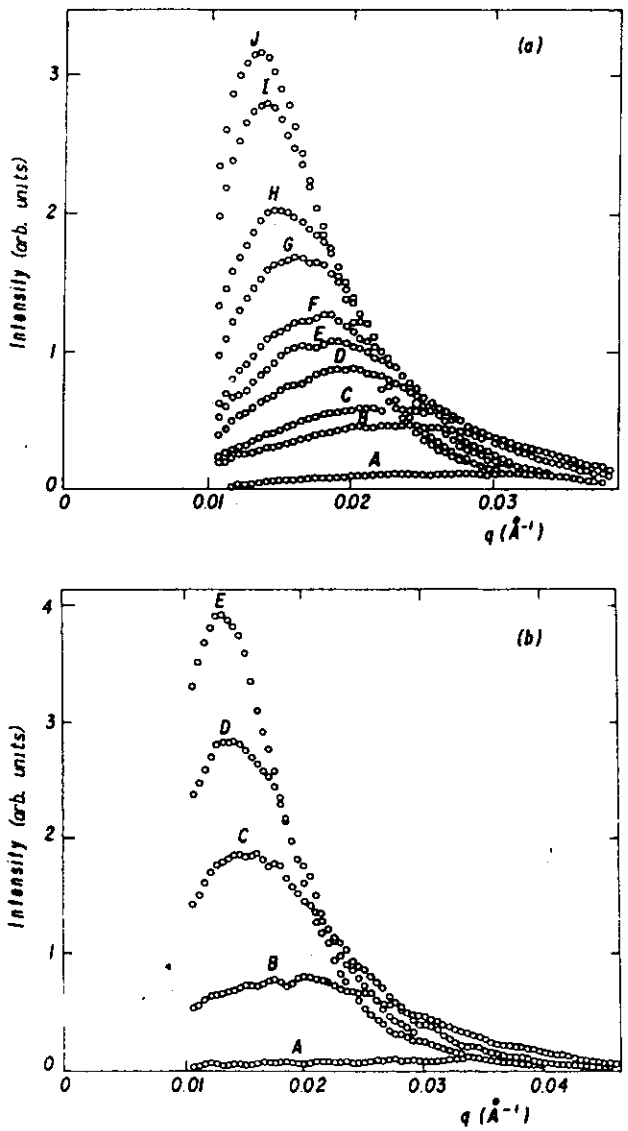

FIG. 2. Time evolution of the SAXS intensity (in arbitrary units) for composition S. (a) Samples heat treated at 460°C and increasing times (min): A, 1.5; B, 6.5; C, 11.3; D, 18.1; E, 21.0; F, 25.6; G, 37.3; H, 46.9; I, 67.1; J, 78.0. (b) Samples heat treated at 480°C and times (min): A, 4.4; B, 7.2; C, 10.7; D, 15.0; E, 22.0.

the normalized moments $q_1(t)$ and $q_2(t)$ may be obtained directly using $I(q,t)$ in Eqs. (2) and (3). With this in mind, we have chosen the following relations, derived directly from Eqs. (1)–(7), in order to test the validity of the scaling hypothesis:

$$q_1(t) \propto t^{-a}, \tag{8}$$

$$I_m \propto t^{a'}, \tag{9}$$

$$q_2(t) \propto [q_1(t)]^2, \tag{10}$$

$$Q_0'(t) \propto [q_1(t)]^{-2}, \tag{11}$$

$$Q_1'(t) \propto [q_1(t)]^{-1}, \tag{12}$$

$$Q_2' \propto \text{constant}, \tag{13}$$

where I_m denotes the maximum of the SAXS intensity $I(q_m,t)$.

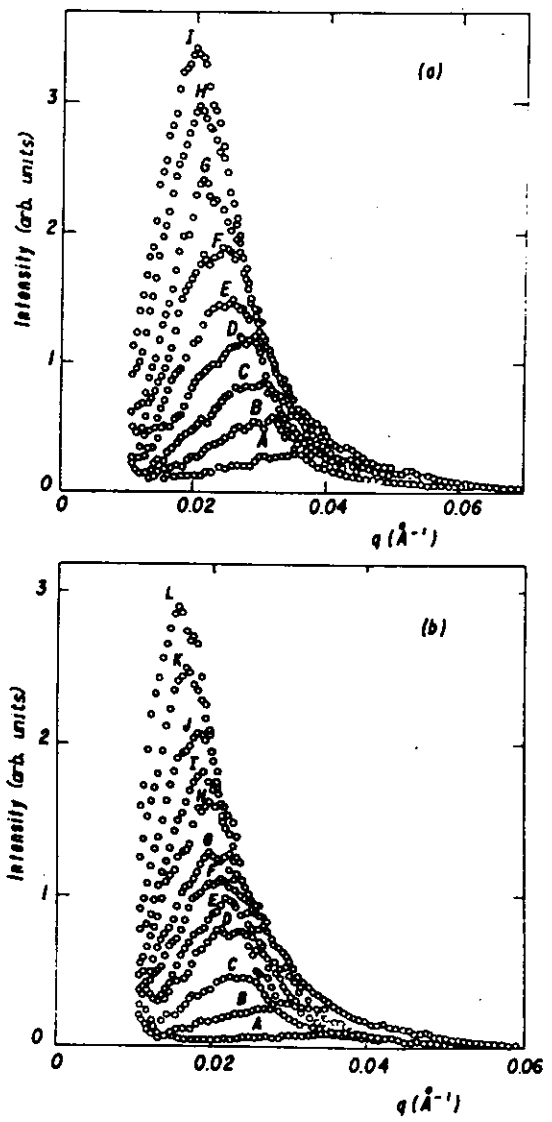

FIG. 3. Time evolution of the SAXS intensity (in arbitrary units) for composition N. (a) Samples heat treated at 480 °C for the following times (min): A, 10.8; B, 12.2; C, 17.0; D, 23.0; E, 29.7; F, 35.8; G, 43.8; H, 54.0; I, 62.7. (b) Samples heat treated at 500 °C for the following times: A, 1.7; B, 3.0; C, 4.5; D, 6.3; E, 7.5; F, 9.3; G, 11.0; H, 13.5; I, 16.0; J, 19.5; K, 24.0; L, 30.0.

IV. EXPERIMENTAL RESULTS

The time evolution of the SAXS intensity was determined for samples of composition S during *in situ* isothermal heat treatment of 460 °C, 470 °C, and 480 °C. Figures 2(a) and 2(b) show the measured intensity in arbitrary units for 460 °C and 480 °C, respectively, and several times. For this composition and temperatures, the system lies deep inside the classical spinodal region of the miscibility gap (Fig. 1). SAXS curves were also obtained from samples having the composition N and treated isothermally at 480 °C, 490 °C, and 500 °C for different lengths of time. In this case, the system is located close to the boundary of the miscibility gap (Fig. 1) where, according to the classical theory, decomposition proceeds by a nucleation and growth mechanism. The evolution of the SAXS curves for composition N at 480 °C and 500 °C are shown, respectively, in Figs. 3(a) and 3(b).

Plots of the normalized first moment $q_1(t)$ versus t are shown in Fig. 4(a) for samples of composition S and three different temperatures (460 °C, 470 °C, and 480 °C). Figure 4(b) shows the same plots for samples of composition N at 480 °C, 490 °C, and 500 °C. As seen in the figures, the behavior predicted by Eq. (8) is closely obeyed. For the

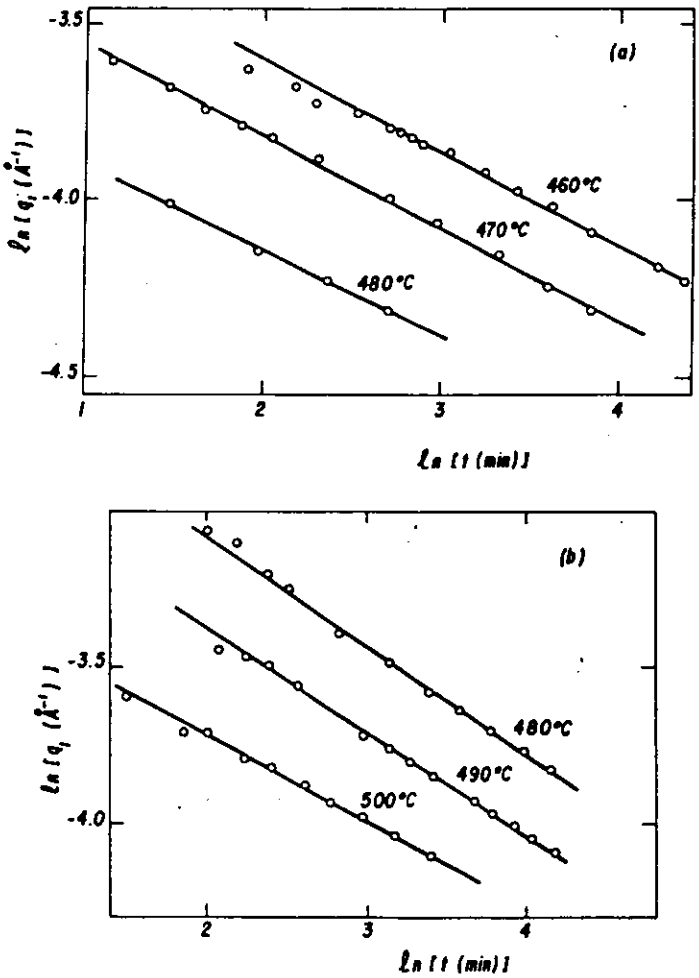

FIG. 4. Time dependence of the inverse characteristic length q_1 corresponding to compositions S (a) and N (b) at several temperatures.

relatively narrow temperature range investigated, the exponents do not change appreciably with temperature, although they show a definite tendency to increase as we move from composition S at the center to composition N near the boundary of the miscibility gap.

The time evolution of the maximum of the SAXS intensity is shown in Figs. 5(a) and 5(b) for, respectively, compositions S and N. In all cases it is seen that the exponents a' are very closely equal to three times the corresponding exponents a shown in Fig. 4. As mentioned in Sec. III, this behavior is expected from the conservation of integrated intensity during the late stages of decomposition.

The general validity of Eqs. (10)—(13) is demonstrated in Fig. 6 for composition S at 460°C. In these figures, we have plotted the moments $Q_0(t)/Q_0(t_f)$, $Q_1(t)/Q_1(t_f)$, $Q_2(t)/Q_2(t_f)$, and $q_2(t)/q_2(t_f)$, versus $q_1(t)/q_1(t_f)$, where t_f stands for the longest time investigated at each temperature and composition. The behavior predicted by Eqs. (10)—(13), indicated by the solid lines in Fig. 6, is closely followed by all the studied glass samples. In particular, the second moment $Q_2(t)$ is essentially time independent. Fittings similar to that of Fig. 6 were observed for the other temperatures investigated.

Figures 7(a) and 7(b) show plots of the ratio q_2/q_1^2 as a function of time for compositions S and N, respectively, and for all temperatures investigated. In the scaling regime, this parameter is characteristic of the scaling function itself and it equals f_2/f_1^2 [see Eq. (5)].

Finally, the scaling behavior of the experimental structure function can be seen in Fig. 8 for composition S at 460°C and 480°C, and in Fig. 9 for composition N at 480°C and 500°C. In these figures we plot $[q_1(t)]^3 I(q,t)/Q_2$ versus $q/q_1(t)$. The approximately constant normalization factor Q_2 is introduced since all intensity measurements were carried out in arbitrary units. It should be noted that with this normalization factor, the scaling function $F(x)$ is such that its second moment F_2 is equal to 1. In Figs. 8 and 9 we have excluded scattering curves for which the integrated intensity Q_2 differs significantly from the nearly time-independent Q_2 values seen during the late stages of decomposition. These excluded SAXS profiles correspond to very early stages of phase separation and are not expected to follow the asymptotic scaling behavior. The deviation from the scaling law for small values of t can also be inferred, particularly for composition N, from the lack of constancy of q_2/q_1^2 seen in Fig. 7.

No significant differences between the scaling function

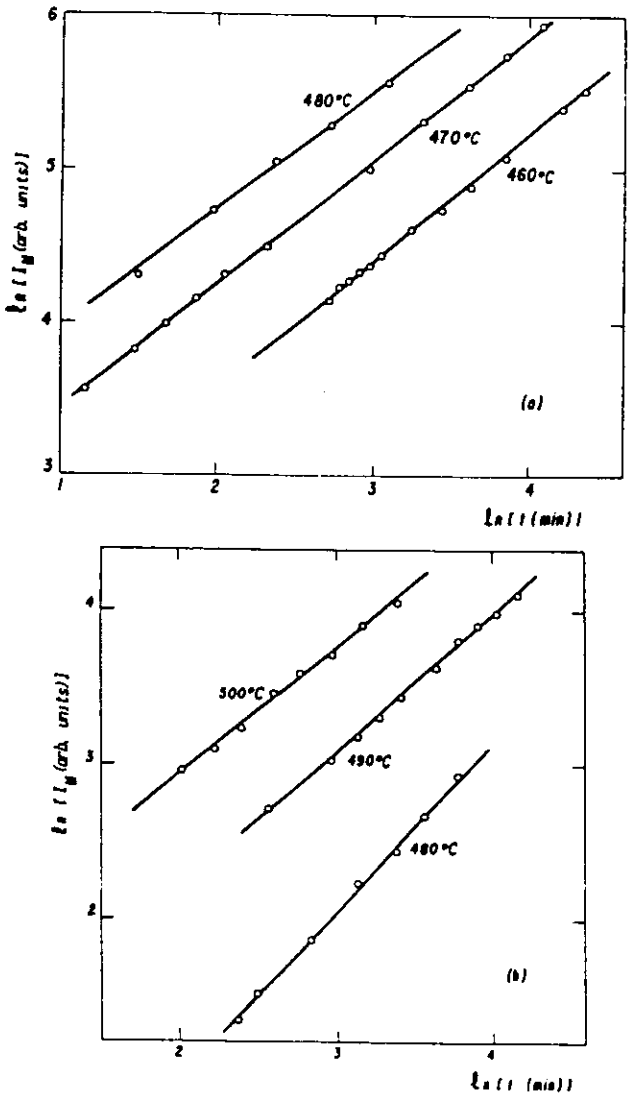

FIG. 5. Time dependence of the maximum of the SAXS intensity corresponding to composition S (a) and N (b) at several temperatures.

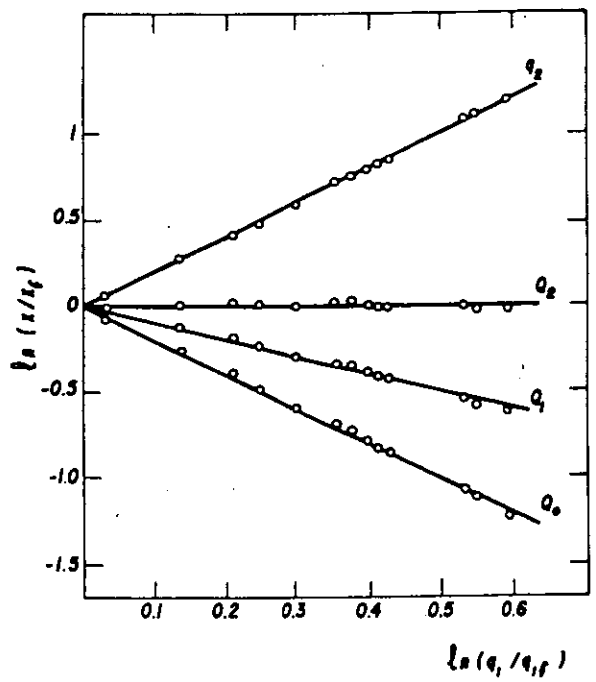

FIG. 6. Dependence of the moments $Q_n(t)$ $(n=0,1,2)$ and of the normalized second moment $q_2(t)$ on the inverse characteristic length $q_1(t)$ for composition S at 460°C. All moments are normalized to the corresponding value at the longest aging time.

$F(x)$ was detected for different temperatures at the same composition. However, appreciable changes are seen from one composition to the other. In Table I three parameters that characterize semiquantitatively the scaling function are given. These are the maximum F_m, the width at half maximum Δ, and the position of the maximum x_m. We see from Table I that $F(x)$ becomes considerably sharper near the boundary of the miscibility gap, although the ratio of normalized moments f_2/f_1^2, shown in the third column of the table, remains essentially constant with temperature and composition.

V. DISCUSSION AND CONCLUSIONS

We have found general agreement between the SAXS experimental results and the predictions of the statistical theories on the dynamics of phase separation for all glasses investigated. The scaling laws, and in particular Eqs. (10)—(13), are closely obeyed during the late stages of decomposition. An important experimental criterion for establishing "late stages" is the time independence of q_2/q_1^2. As seen in Fig. 7, scaling is reached relatively early in the decomposition process for samples of composition S, whereas for samples of composition N the scaling regime has apparently been reached only for the longest times measured. The plots of Fig. 7 are only meaningful to the extent that the first few moments of the SAXS intensity may be calculated accurately. In this regard, the experimental verification of the conservation of the integrated intensity, i.e., constancy of Q_2, plays a key role

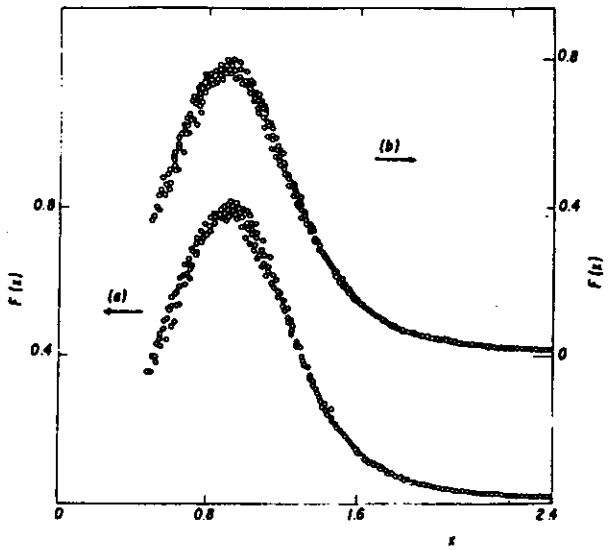

FIG. 8. Scaling of the structure function for composition S at 460°C (a) and at 480°C (b).

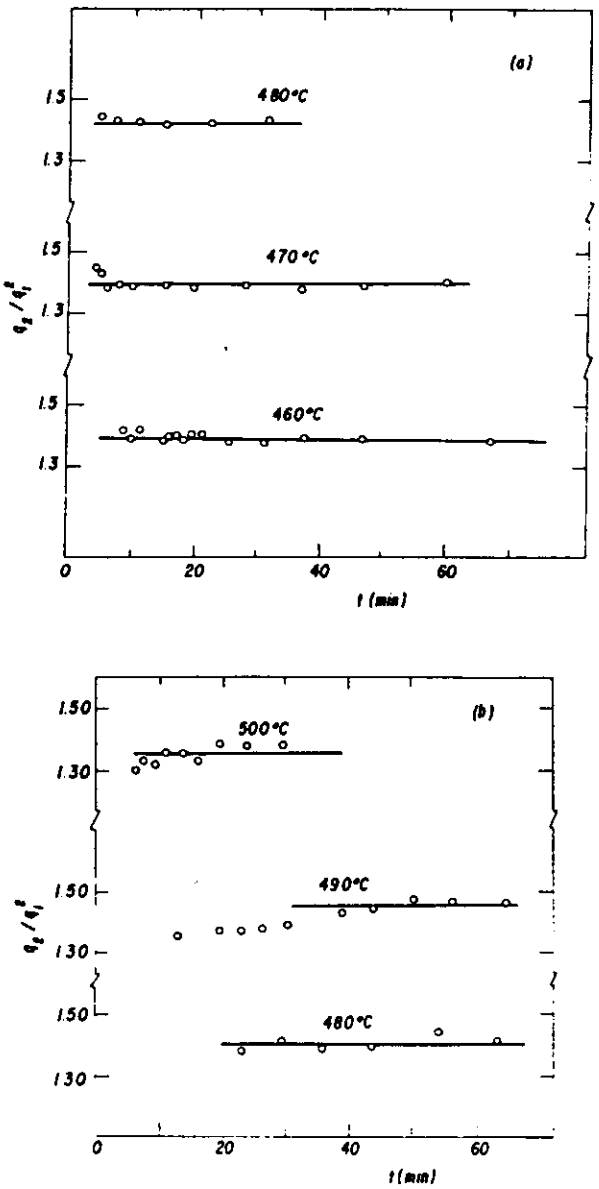

FIG. 7. Time dependence of the ratio q_2/q_1^2 for compositions S (a) and N (b) at several temperatures.

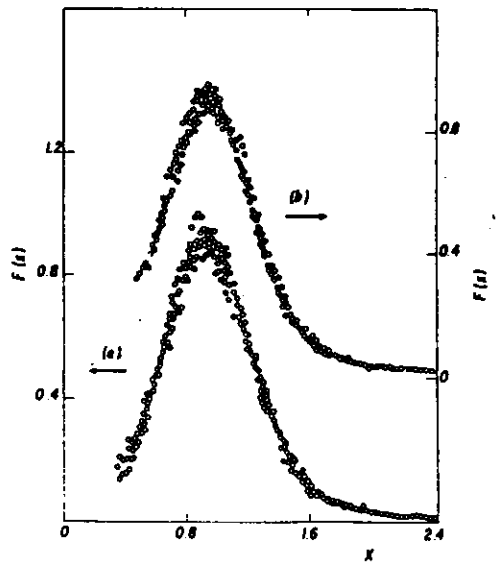

FIG. 9. Scaling of the structure function for composition N at 480°C (a) and at 500°C (b).

2.b

5f

TABLE I. Scaling parameters for samples with wt.% compositions B_2O_3, 80 wt%; PbO, 15 wt%; Al_2O_3, 5 wt% (S) and B_2O_3, 64 wt%; PbO, 27 wt%; Al_2O_2, 9 wt% (N). F_m, x_m, and Δ indicate the maximum, the position of the maximum and the half-maximum width, respectively, of the experimental scaling function.

Sample	T (°C)	q_2/q_1^2	a	a'	$3a$	F_m	x_m	Δ
S	460	1.39	0.26	0.83	0.78	0.77	0.90	0.80
S	470	1.40	0.26	0.81	0.78	0.79	0.90	0.80
S	480	1.42	0.24	0.77	0.72	0.78	0.90	0.80
N	480	1.41	0.35	1.10	1.05	0.92	0.94	0.68
N	490	1.45	0.32	0.90	0.96	0.92	0.94	0.68
N	500	1.38	0.27	0.84	0.81	0.92	0.94	0.68

(see Fig. 6). Although the integrated intensity should be strictly conserved at all times, SAXS measurements can only be performed within a "window" in reciprocal space. Thus, for very early stages, the important contribution of short-range correlations (large values of q) to the experimental structure function are not included, which results in the time dependence of Q_2. However, once Q_2 reaches a constant value with time, one is confident that all the relevant information in the structure function is contained in $I(q,t)$. Clearly, in those cases for which the integrated intensity is seen to change with time, a more appropriate test of scaling would be the procedure proposed by Fratzl *et al.*[6] For our data, however, the determination of the characteristic length by calculation of q_1 or by the graphical procedure of Fratzl *et al.* produce the same results.

An additional consistency check on the analysis of the experimental data is the expected relation $a'=3a$, where a and a' are, respectively, the time exponents defined by Eqs. (8) and (9). As seen in Table I this relation is obeyed by the borate glasses for all temperatures and compositions. The relation $a'=3a$ has not been observed in some of the metallic systems studied in the past,[11,13] although the reason is most likely due to data analysis (including perhaps crystal anisotropy) than to a violation of the scaling laws.

Concerning the time exponent of the characteristic length, we obtain average values of $a\approx 0.25$ for composition S and $a\approx 0.31$ for composition N. Thus, at least qualitatively, our results appear to confirm the predictions of Stauffer and Binder[1] of a crossover between a low-temperature cluster coagulation mechanism near the center of the miscibility gap, with exponent $a=\frac{1}{6}$, and the classical particle coarsening process of Lifshitz and Slyozov with exponent $a=\frac{1}{3}$ near the boundary of the gap. The experimental exponents are also in good quantitative agreement with the computer simulations of Marro *et al.*[4] who reported values of a ranging from 0.2 near the center to approximately 0.3 near the boundary of the miscibility gap.

The experimental scaling function $F(x)$ shows a dependence with composition: as we move from the center to the boundary of the miscibility gap, the maximum F_m increases, it shifts to slightly larger values of x, and the width at half maximum Δ decreases significantly (see Table I). This particular behavior of $F(x)$ is opposite to that predicted by the model of Rikvold and Gunton,[16] Furukawa,[2] and the computer simulations.[4] Although different normalization schemes are used by different authors (in our case we use the second moment F_2 equal to 1), the theoretical models and simulations predict, nevertheless, a sharper scaling function near the center of the gap.

Significantly, recent work on Fe-Cr by Katano and Iizumi[13] has shown that, for the same system with composition near the center of the miscibility gap, the characteristic length exponent changes with time from a value of 0.2 characteristic of a coagulation mechanism, to 0.33 as expected from a diffusion controlled process. This crossover in the exponent a has also been documented by Forouhi[12] in Al-Mg-Zn alloys. Concurrent with this apparent change in particle growth mechanism, Katano and Iizumi report a pronounced change in the shape of the scaling function: $F(x)$ becomes sharper (more peaked) during the very late stages for which the characteristic length exponent is close to 0.33. Thus, the experiments in Fe-Cr together with our results in glasses seem to indicate that the shape of the scaling function is intimately related to the underlying growth mechanism.

In conclusion, our SAXS investigation of phase separation in glasses, performed under particularly favorable conditions (pinhole collimation and *in situ* heat treatment) is in quantitative agreement with statistical theories and the scaling hypothesis. The results concerning the evolution of the structure function for different compositions and temperatures agree well with the computer simulations of Lebowitz and co-workers. Changes in shape of the experimental scaling function with composition do not conform to the predictions of the various theoretical models available. The evidence points towards a correlation between the shape of $F(x)$ and the mechanism of particle growth, at least to the extent that the latter is accurately reflected in the value of the characteristic length exponent a. Further experimental and theoretical work is clearly needed in order to elucidate this point.

ACKNOWLEDGMENTS

We wish to thank E. D. Zanotto for collaboration in preparing the glass samples and S. Bras for assistance in using the position sensitive detector. One of us (A.F.C.) acknowledges the hospitality of the staff at LURE during the initial stages of this investigation.

[1]K. Binder and D. Stauffer, Phys. Rev. Lett. 33, 1006 (1974); K. Binder, Phys. Rev. B 15, 4425 (1977).
[2]H. Furukawa, Phys. Rev. Lett. 43, 136 (1979); H. Furukawa, Phys. Rev. A 23, 1535 (1981).
[3]E. D. Siggia, Phys. Rev. A 20, 595 (1979).
[4]A. B. Bortz, M. H. Kalos, J. L. Lebowitz, and M. H. Zendejas, Phys. Rev. B 10, 535 (1974); J. Marro, A. B. Bortz, M. H. Kalos, and J. L. Lebowitz, *ibid.* 12, 2000 (1975); M. Rao, M. H. Kalos, J. L. Lebowitz, and J. Marro *ibid.* 13, 4328 (1976); J. Marro, J. L. Lebowitz, and M. H. Kalos, Phys. Rev. Lett. 43, 282 (1979); J. L. Lebowitz, J. Marro, and M. H. Kalos, Acta Metal. 30, 297 (1982).
[5]I. M. Lifshitz and V. V. Slyozov, J. Phys. Chem, Solids 19, 35 (1961).
[6]P. Fratzl, J. L. Lebowitz, J. Marro, and M. H. Kalos, Acta Metal. 31, 1849 (1983).
[7]C. M. Knobler and N. C. Wong, J. Phys. Chem. 85, 1972 (1981).
[8]Y. C. Chou and W. I. Goldburg, Phys. Rev. A 23, 858 (1981).
[9]D. N. Sinha and J. K. Hoffer, Physica (Utrecht) 107B&107C, 155 (1981).
[10]A. F. Craievich and J. M. Sanchez, Phys. Rev. Lett. 47, 1308 (1981).
[11]M. Hennion, D. Ronzaud, and P. Guyot, Acta Metal. 30, 599 (1982).
[12]A. R. Forouhi, Doctoral dissertation, University of California, Berkeley, 1982 (unpublished).
[13]S. Katano and M. Iizumi, Phys. Rev. Lett. 52, 835 (1984); S. Katano and M. Iizumi, Physica (Utrecht) 120B, 392 (1983).
[14]A. F. Craievich, J. Appl. Cryst. 7, 634 (1974).
[15]J. Zarzycki and F. Naudin, J. Non-Cryst. Solids 1, 215 (1969).
[16]P. A. Rikvold and J. D. Gunton, Phys. Rev. Lett. 49, 1223 (1982).

Formation and Growth of Semiconductor PbTe Nanocrystals in a Borosilicate Glass Matrix

A. F. Craievich, National Synchrotron Light Laboratory/CNPq, Campinas-SP and Institute of Physics/USP, São Paulo-SP, Brazil, O. L. Alves, Solid State Chem. Lab., Institute of Chemistry/UNICAMP, Campinas-SP, Brazil and L. C. Barbosa, Institute of Physics/UNICAMP, Campinas-SP, Brazil

Abstract

Pb and Te-doped borosilicate glasses are transformed by appropriate heat treatment into a composite material consisting of a vitreous matrix in which semiconducting PbTe nanocrystals are embedded. This composite exhibits interesting non-linear optical properties in the infrared, in the range of 10-20.000 Å. The characterization of the shape and size distribution of the nanocrystals and the kinetics of their growth were studied by SAXS during *in situ* isothermal treatment at 650 C. The SAXS curves were fitted using a theoretical scattering function for a diluted set of spheres having a Gaussian size distribution with an increasing average radius and a time-constant relative width. The experimental results indicate that nanocrystals are nearly spherical and have an average radius increasing from 16 up to 33 Å after two hours at 650 °C, the relative size dispersion being time-invariant and approximately equal to 8 %. This investigation demonstrates that the kinetics of nanocrystal growth is governed by the classic mechanism of atomic diffusion. The radius of nanocrystals, deduced by applying the simple Efros and Efros model to the energy values corresponding to the exciton peaks of optical absorption spectra, does not agree with the average radius determined by SAXS.

1. Introduction

A number of doped glasses are transformed by appropriate heat treatment into composite materials consisting of a vitreous matrix in which semiconductor nanocrystals are embedded. When the semiconductor crystals are small, electronic quantum confinement effects occur. The optical properties of a number of silicate and borosilicate glasses containing CdS (Potter & Simmons), CdSe (Borrelli *et al., 1987*), CdTe (Medeiros Neto *et al.*, 1991) etc were investigated by optical measurements in the visible wavelength range. Recently a new material, a borosilicate glass-PbTe nanocrystal composite which exhibits quantum confinement effects in the infrared, was discovered (Reynoso *et al.*, 1995). The consequent non-linear optical properties, being in the infrared, make this material a good candidate for applications in telecommunication devices.

The structural characterization of nanocrystals embedded in glassy matrix is usually carried out by analyzing the experimental optical absorption spectrum of the material. This spectrum exhibits a more or less sharp absorption edge and, in some cases, one or more exciton peaks, their position in the spectrum being dependent on the average size, on the size distribution and on the shape of the nanocrystals.

The method most frequently used for determining the average radius of the nanocrystals from optical data applies the Efros & Efros equation (Efros & Efros, 1982). This equation is based on a theoretical model for optical absorption which assumes spherical nanocrystals and simple parabolic energy bands for electrons and holes. It is worthwhile, however, to carry out independent experimental studies of the composites using a technique which provides more direct structural information. Because of the small size of the nanocrystals, the small-angle scattering (SAXS) technique is a good choice for obtaining relevant structural information.

Applications of glass-semiconductor nanocrystal composites in non-linear optical devices usually require the nanocrystals to be nearly isodiametric and have a narrow size distribution. This paper reports the first SAXS study of a borosilicate glass-PbTe nanocrystal composite.

2. Sample preparation and optical characterization

The nominal composition of the studied glass is $52SiO_2$-$8B_2O_3$-$20ZnO$-$20K_2O$. The raw material was doped with 2% PbO and Te (weight %), homogenized at 1350 °C during 50 min and quenched down to room temperature. By appropriate polishing, a transparent lame about 0.1 mm thick was obtained. It was then placed inside a cell at 650° C for *in situ* SAXS measurements.

Optical absorption spectra of an equivalent sample, also held at 650° C for different periods of time, were recorded and are plotted in Fig. 1. Taking into account that the energy gap of a bulk PbTe semiconductor is 0.337 eV, the wavelength corresponding to the absorption edge is 36,800 Å. The various spectra in Fig. 1 show that the absorption edges are located at wavelengths $\lambda < 20{,}000$ Å, clearly exhibiting the known blue-shift effect associated with the nanometric size of the crystals. Well-defined exciton peaks are also apparent, their position shifting from $\lambda = 12{,}000$ Å up to 19,000 Å for periods of time increasing from 10 up to 60 min. This confirms that the crystals are nanometric and that they progressively grow. The average sizes of the nanocrystals in the several samples were inferred from the optical absorption spectra plotted in Fig. 1, using the Efros & Efros equation (Efros & Efros, 1982). The results are reported in section 4.

3. Experimental SAXS setup

The SAXS experiments were performed at the D24 workstation of the synchrotron radiation laboratory LURE, Orsay. In this workstation the beam is horizontally focused and monochromatized using a bent silicon crystal ($\lambda = 1.49$Å). Three sets of slits define a collimated beam with a point-like cross-section at the detection plane. The sample was held at constant temperature (T= 650 °C) using a high-temperature cell, stable within 1°C, during the *in situ* SAXS study.

The quenched and initially homogeneous doped glass was placed inside the high-temperature cell and maintained at constant temperature during SAXS measurements.

The X-ray scattered intensity, I(q), was measured as a function of the modulus of the scattering vector q, using a one-dimensional position-sensitive X-ray detector. An ionization chamber, placed downstream from the sample, was used to monitor the intensity decay of the transmitted beam and to determine the sample attenuation. Parasitic air and slit scattering were subtracted from the total intensity. The counting time for each SAXS spectrum was 300 sec and the measurements were repeated at about every 500 sec.

We have estimated the influence on the small-angle scattering intensity from the small, but non-zero, cross-section of the incident beam at the detection plane and from the finite resolution of the position-sensitive detector. We concluded that these effects on the experimental SAXS intensity are negligible.

4. Results and discussion

The formation of PbTe nanocrystals introduces heterogeneities in the electronic density of the initially quasi-homogeneous material. PbTe nanocrystals embedded in borosilicate glass are efficient X-ray scatterers because of their very high electronic density as compared with the density of the light matrix. If we assume a simple two-electronic-density model for the nanocrystal-glass composite, with nanocrystals or "particles" occupying a small fraction of the total volume, the Guinier equation applies to the SAXS intensity function in the small q-range limit:

$$I(q) = I(0) \exp[-(\langle R_g \rangle^2 q^2/3)] \qquad (1)$$

with

$$I(0) = (\Delta\rho)^2 N \langle v^2 \rangle \qquad (2)$$

$\langle R_g \rangle$ being the so called Guinier average of the radius of gyration of the particles, $\Delta\rho$ the difference in electron density between the particles and the matrix, N the number of particles per unit volume and $\langle v^2 \rangle$ the average of the particle square volume (Guinier & Fournet, 1955). In the case of a set of spherical particles with a radius distribution given

by g(R) and taking into account that in this case $R = (5/3)^{1/2} R_g$, the Guinier average $\langle R_g \rangle$ is given by

$$< R_g >= (3/5)^{1/2} R_G = (3/5)^{1/2} [\frac{\int R^8 g(R) dR}{\int R^6 g(R) dR}]^{1/2} \qquad (3)$$

R_G being the Guinier average radius of the nanocrystals. Equation 1 is in practice obeyed within a large q range when the particles are identical or have a rather narrow size distribution.

The experimental SAXS intensity functions are displayed as log I versus q^2 (Guinier plot) in Fig. 2. The increase in SAXS intensity for samples held at 650 °C during increasing periods of time is a consequence of the progressive formation of PbTe nanocrystals which are responsible for the variation in the optical absorption reported in section 2.

We note that the Guinier plots of all curves in Fig. 2 exhibit a rather wide linear range with an increasing slope as the time of heat treatment increases. The increasing slope in the linear q-range indicates a progressive growth of the nanocrystals, in agreement with the conclusion inferred from the optical absorption measurements. The Guinier average radius of the nanocrystals, R_G, was determined using equations 1 and 3 as a function of the isothermal treatment time. We also noted in Fig. 2 that the linear behavior of I(q) is followed by a negative deviation as q increases. This occurs when the system is composed of quasi-isodiametric scattering particles with a narrow size distribution.

The scattering curves in Fig. 2 exhibit an abrupt increase in intensity at very small q. This was also observed in the SAXS intensity function from the same sample before heating. The very large negative slope at very small q indicates that this contribution to the experimental scattering intensity is a consequence of the existence of large-sized electronic density heterogeneities in the glass matrix. Since this contribution to SAXS intensity remains approximately constant for increasing periods of time, we concluded that the coarse heterogeneities do not evolve significantly. The same kind of effect was

already observed in a previously studied borosilicate glass doped with CdTe (Craievich, Alves & Barbosa, 1994). This contribution to SAXS intensity, being confined to very small q, is not considered in the further analysis associated with the formation and growth of PbTe nanocrystals.

For long periods of time at 650 °C a satellite peak is clearly apparent in the experimental SAXS intensity functions plotted in Fig. 3. This effect in scattering curves is in general produced by spherical or spheroidal particles, all of them having approximately equal radii. The conclusion about the spheroidal shape of the nanocrystals is equivalent to that previously established by transmission electron microscopy for glass-CdS composites (Liu & Risbud, 1990a).

We obtained more quantitative structural information on the studied materials by fitting the experimental SAXS intensity with a theoretical scattering function for a set of spherical nanocrystals. The scattering function, $I_s(q)$, for a sphere with a radius R is given by (Guinier & Fournet, 1955):

$$I_s(q) = K\left(\frac{4\pi R^3}{3}\right)^2[\Phi(q R)]^2$$

where K is a constant and

$$\Phi(q R) = 3\frac{\sin(q R) - q R \cos(q R)}{(q R)^3}$$

Assuming a set of spherical nanocrystals with a Gaussian radius distribution embedded in a homogeneous matrix, the fitting function for the experimental SAXS intensity I(q) is given by

$$I(q) = A\int g(R)R^6[\Phi(q R)]^2 dR + B \qquad (4)$$

where

$$g(R) = \frac{1}{\sqrt{2\pi}\sigma} \exp[-\frac{(R - R_A)^2}{2\sigma^2}] \qquad (5)$$

R_A being the nanocrystal average radius, σ the standard deviation of the radius distribution, A a scale constant and B a constant which accounts for a constant contribution to the scattering intensity produced by short-range electronic density fluctuations in the matrix.

It was assumed in the fitting procedure using the function defined by equation 4, that the quotient σ/R_A is a time constant equal to 8 % during the whole isothermal treatment. The best fitting functions of several SAXS curves for different heat treatment times are shown in Fig. 3. A good agreement between the theoretical and experimental SAXS intensities is apparent for all heat treatment times in the full q-range, except in the very small q-range, in which the contribution from the previously mentioned coarse heterogeneities is predominant.

We determined another Guinier average of the nanocrystal radii, R_G', using equations 3 and 5 with the parameters R_A and σ of the fitting functions plotted in Fig. 3. The values of the average radii R_G and R_G' are expected to be the same provided the basic assumptions of the model (dilute system, spherical nanocrystals and Gaussian size distribution) actually correspond to the real system.

Another average radius, R_O, was determined from the optical spectra plotted in Fig. 1, using the Efros and Efros equation (Efros & Efros, 1982) based on a simple model of spherical nanocrystals and parabolic energy bands for electrons and holes:

$$E - E_b = \frac{\hbar^2\pi^2}{2\mu} \frac{1}{R_o^2} \qquad (6)$$

E_b being the energy gap in the bulk semiconductor, E the energy of the first exciton peak and $\hbar=h/2\pi$, h being the Planck constant. The exciton reduced mass μ is given by

$$\frac{1}{\mu} = \frac{1}{\mu_e} + \frac{1}{\mu_h}$$

with $\mu_e = \mu_h = 0.058$ m (Ishida et al, 1987), m being the electron mass.

The Guinier average R_G obtained from the slopes of the linear portions of the Guinier plots in Fig. 2, the average radius R_A with an error bar +- σ corresponding to the fitting functions plotted in Fig. 3, the Guinier average of the radius R_G' determined using the Gaussian size distribution and the above mentioned R_A and σ values, and the Efros & Efros average radius R_O, obtained from the spectroscopic data (Fig. 1), are plotted in Fig. 4 as functions of the heat treatment time.

We observe in Fig. 4 that the R_G and R_G' values are larger than R_A. Values larger than R_A are expected because the Guinier average of the nanocrystal radii, defined in equation 3, weighs much more the large nanocrystals. However in Fig. 4 a small but noticeable difference between R_G and R_G' is apparent. This indicates that the real structure of the borosilicate glass-PbTe nanocrystal composites deviates slightly from the assumed structural model consisting of a dilute system containing spherical shaped nanocrystals with Gaussian size distribution. We have estimated that the difference between R_G and R_G' is a consequence of slight deviations from the sphericity in nanocrystal shape as was previously observed in electron microscopy studies of CdSe and CdS nanocrystals (Liu & Risbud, 1990a). We then concluded that the PbTe nanocrystals are approximately isodiametric or spheroidal.

As can be seen in Fig. 4, the R_O value calculated from the optical absorption spectra is about twice the average nanocrystal radius, R_A, determined by SAXS. This strong difference between R_O and R_A implies that Efros and Efros equation (equation 6) does not apply to PbTe nanocrystals. The disagreement cannot be explained by the slight deviation of the nanocrystals from the spherical shape but, more probably, by the strong nonparabolicity of the energy bands of the studied semiconductor (Martinez et al, 1987).

In order to characterize the mechanism of nanocrystal formation and growth, we determined the time dependence of the integral of the SAXS intensity I(q) in reciprocal space Q(t) which is related to structural parameters by (Guinier & Fournet, 1955) :

$$Q(t) = \int q^2 I(q,t)dq = (1/4\pi)(\Delta\rho)^2 N(t)\langle v\rangle(t) \qquad (7)$$

$\langle v\rangle$ being the average volume. I(q,t) is the SAXS intensity after subtracting the constant intensity B (equation 4). The integral Q was determined by numerical integration from q_{min}=0.02 Å^{-1} up to q_{max} = 0.25 Å^{-1} and using Guinier and Porod laws (Guinier & Fournet, 1955), respectively, for $q < q_{min}$ and $q > q_{max}$. The fraction of Q corresponding to the q-ranges below q_{min} and above q_{max} is small: it amounts to less than 3 % of the total value.

In the case of spherical particles equations 2 and 7 yield

$$I(0) \propto (\Delta\rho)^2 N \langle R^6\rangle \quad \text{and} \quad Q \propto (\Delta\rho)^2 N \langle R^3\rangle \qquad (8)$$

The quotient $I(0)/(QR^3)$ is expected to be invariant when the growing spherical nanocrystals are identical. This approximately occurs for the quotient $I(0)/(QR_G^3)$ determined from our experimental results plotted in Fig. 5. This result is a complementary evidence of the narrowness of the nanocrystal size distribution in the studied material.

The monotonic increase in the experimental function Q(t), defined in equation 7, for increasing periods of time (Fig. 5) indicates that the volume fraction occupied by the nanocrystals $N\langle v\rangle$ progressively increases. This proves that the structure evolution of the nanocrystal formation is not governed by a pure coarsening or coalescence mechanism. The increase of the integral Q(t) can be due to a progressive increase in the number N and/or in the average volume $\langle v\rangle$ of the nanocrystals.

The experimental SAXS results indicate that nanocrystals nucleate and grow as a consequence of the diffusion of isolated Pb and Te elements through the glass matrix. Under this assumption, the average crystal radius, R_A, is expected to have the simple time dependence given by (Liu & Risbud, 1990b):

$$R^2 = K\,t + R(0)^2 \qquad (9)$$

where K is a constant and R(0) is the initial nanocrystal radius.

The experimental values of R_G for increasing periods of time obey the potential law of equation 9 as can be seen in Fig. 6. This result, together with the time dependence of the integral Q (Fig. 5), are consistent with the proposed mechanism of nanocrystal growth by pure atomic diffusion up to about 1 hour of heat treatment. As the concentration of Pb and Te approaches the solubility limit, coarsening becomes the predominant mechanism responsible for nanocrystal growth and the time dependence of the radius is not longer given by equation 9 and become $R \propto t^{1/3}$ (Lifhshitz and Slezov, 1959). This explains the deviation, observed in Fig. 6, of the R^2 versus t plot from the linear behavior predicted by equation 9.

These results indicate that nuclei having an appreciable critical size (with an average radius of about 16 Å) are initially formed. The growth of the nanocrystals is governed by the classical atomic diffusion mechanism in the first stages and by coarsening in advanced stages of isothermal heat treatment.

5. Conclusion

The conclusions regarding the structural evolution of Pb and Te-doped borosilicate glass materials, quenched from 1350 °C and isothermally treated at 650 °C from 0 to 120 min, are:

- nearly spherical PbTe nanocrystals having an average radius of 16 Å are initially formed,
- during the isothermal treatment the average nanocrystal radius grows up to 33 Å,
- the relative standard deviation of the size distribution function is about 8 %,
- the predominant mechanism for nanocrystal growth is classical atomic diffusion, and
- Efros and Efros equation does not yield a precise estimate of nanocrystal radii probably because of the strong nonparabolicity electron and hole energy bands.

This study shows that SAXS associated with a synchrotron X-ray source is a useful technique for accurate *in situ* characterization of relevant time-dependent structural properties of semiconductor nanocrystals.

Acknowledgment

The authors acknowledge C. L. Cesar for his useful comments on the determination of the average nanocrystal radius from the optical absorption spectra.

References

Borrelli, N. F., Hall, D. W., Holland, H. J. & Smith, R. W. (1987). J. Appl. Phys. 61, 5399-5409

Craievich, A. F., Alves O. L., Barbosa, L. C. (1994) Rev. Sci. Instrum. 66, 1338-1341

Efros, Al. L. & Efros, A. L. (1982). Soviet Phys. Semicond. 16, 772-775

Guinier, A. & Fournet, G. (1955). Small-Angle Scattering of X-rays. New York, Wiley

Ishida, A., Matsuura, S., Mizuno, M.Fujiyasu, H. (1987) Appl. Phys. Lett.,51, 478-480

Liu, B. C. & Risbud, S. H. (1990a). Phil. Mag. Lett. 61, 327-332

Liu, B. C. & Risbud, S. H. (1990b). J. Appl. Phys. 68, 28-32

Martinez, G., Schluter, M. and Cohen (1987) M. Phys Rev B 11, 651-658

Medeiros Neto, J. A., Barbosa, L. C., Cesar, C. L., Alves, O. L. & F. Galembeck, (1991). Appl. Phys. Lett. 59, 2715-2717

Potter, B. C. & Simmons, J. H. (1988). Phys. Rev. B37, 10838-10845

Reynoso, V. C. S., de Paula, A. M., Cuevas, R. F., Medeiros Neto, J. A., Alves, O. L., C. L., Cesar & Barbosa, L. C. (1995). Electr. Lett. 31, 1013- 1015.

Figure Captions

Figure 1 : Coefficient of optical absorption of the glass-PbTe composites for *ex-situ* isothermal treatment during the indicated time.

Figure 2 : Guinier plots of SAXS intensity from the glass-PbTe composite during *in-situ* isothermal treatment. The weakest intensity curve corresponds to 10 min and the strongest to 2 hours at 650 °C.

Figure 3 : Plots of the SAXS intensity for different periods of time. The continuous lines are the theoretical functions for a set of spherical nanocrystals having a radius distribution with a relative standard deviation of 8 % and the following average radii: 21.0 Å (19 min), 24.0 Å (38 min), 27.0 Å (56 min), 29.0 Å (78 min), 31.0 Å (98 min), 32.5 Å (119 min). The curve corresponding to the shortest time is on the bottom, the others were vertically displaced for clarity.

Figure 4 : Average nanocrystal radius R_A (o) with bars corresponding to $\pm \sigma$, Guinier average radii R_G (⊞) and R_G (♦), and Efros and Efros radius R_O (■) as functions of time.

Figure 5 : Time dependence of the integral $Q(t) = \int q^2 I(q,t)dq$ and of the quotient $I(0)/(Q\ R_G^3)$.

Figure 6 : Square of the Guinier average nanocrystal radius (R_G^2) as a function of time.

Fig. 1

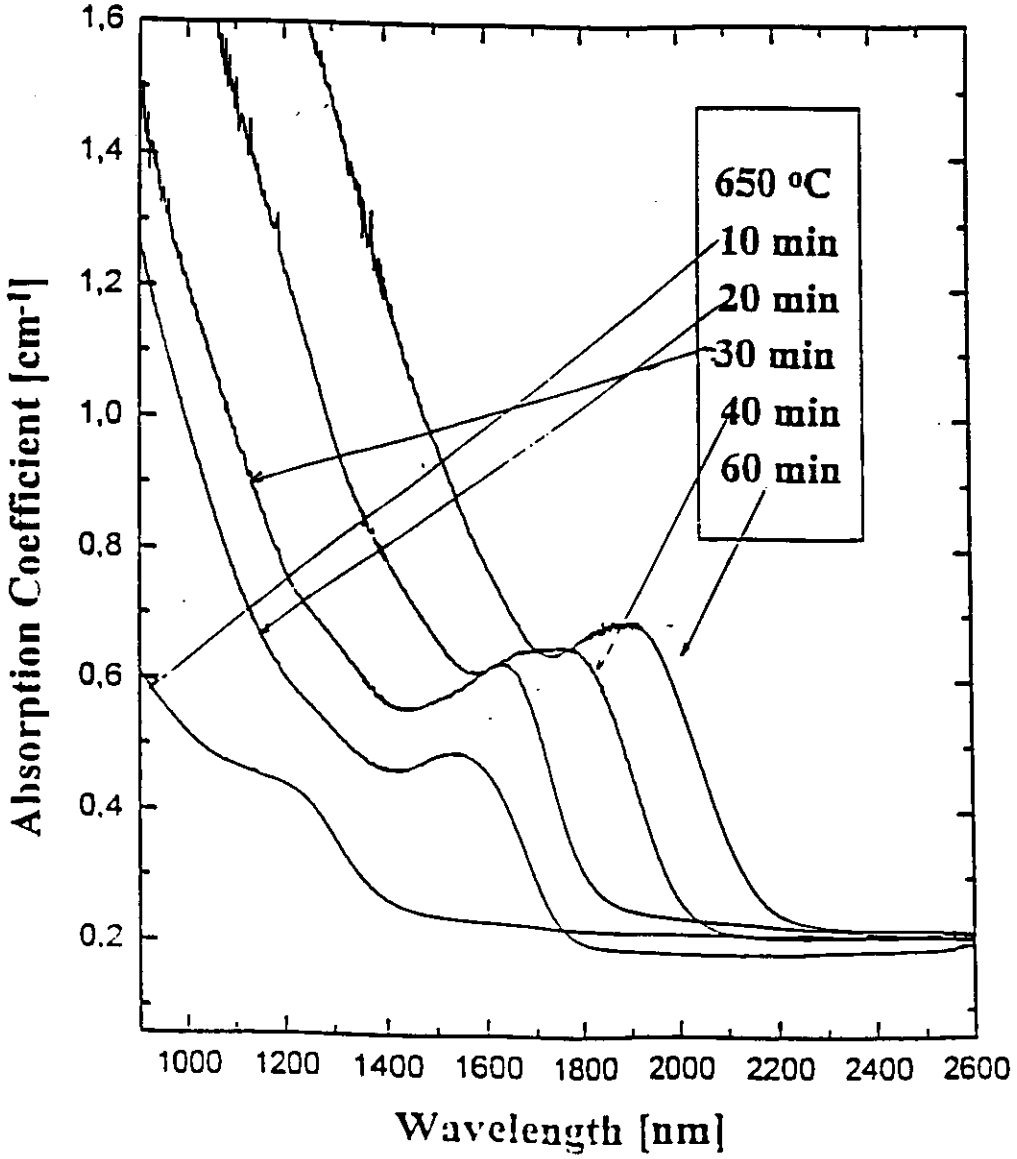
Absorption Coefficient [cm-1]
1,6
1,4
1,2
1,0
0,8
0,6
0,4
0,2
650 °C
10 min
20 min
30 min
40 min
60 min
1000
1200
1400
1600
1800
2000
2200
2400
2600
Wavelength [nm]

-0.02
-0.01
0.00
0.01
0.02
$q^2(A^{-2})$
2
4
6
8
Log Intensity (a. u.)

Fig. 3

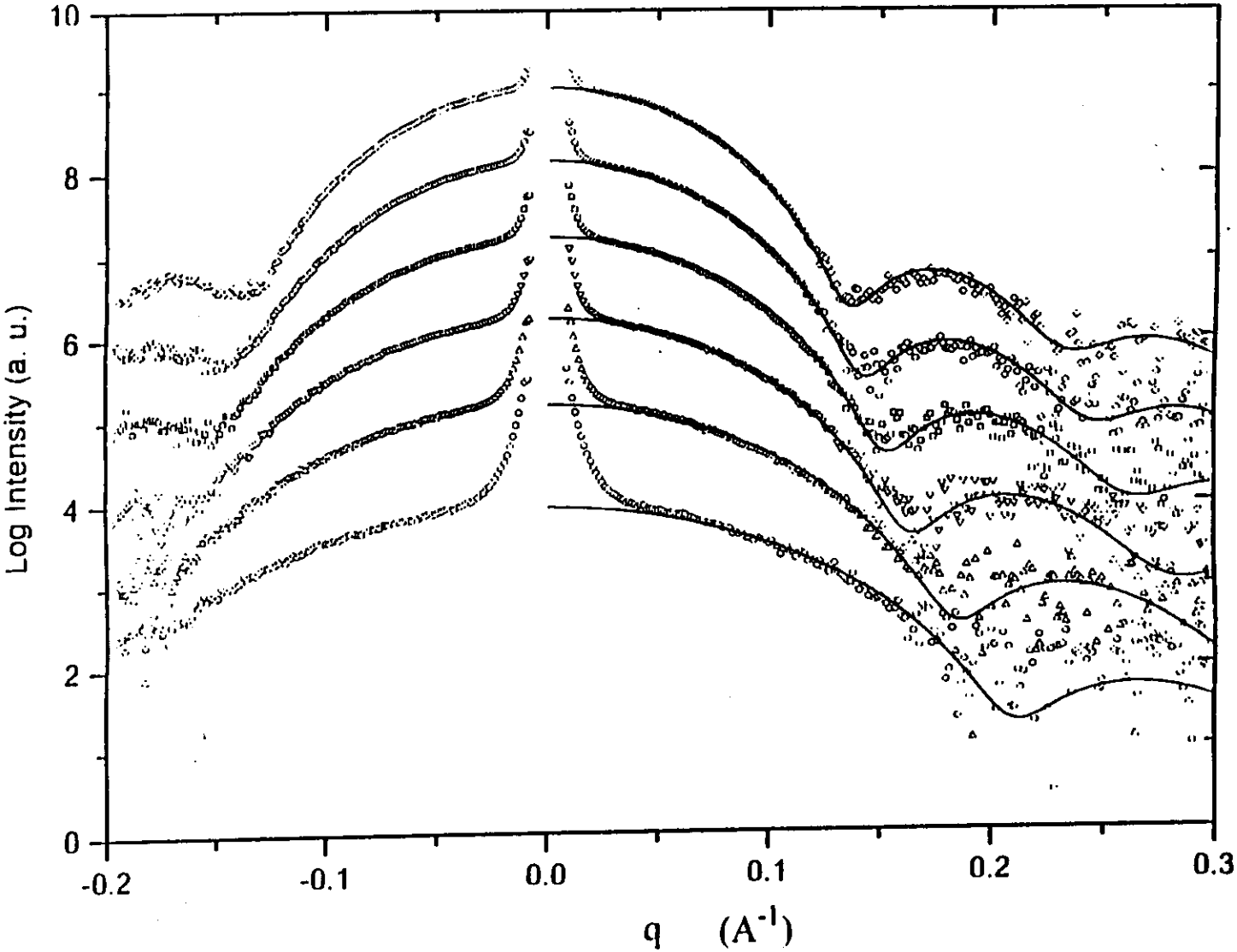

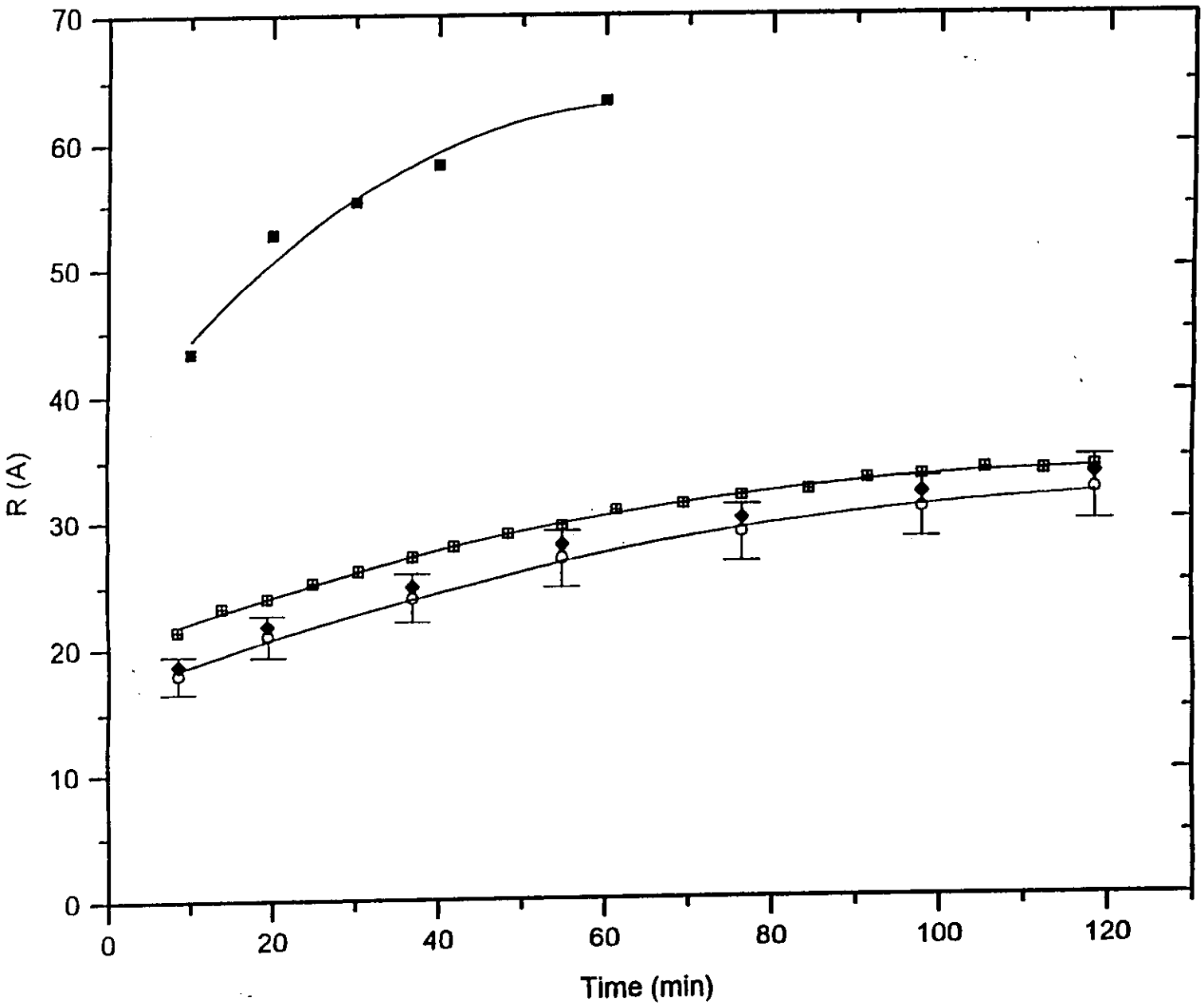
70
60
50
40
30
20
10
0
R (A)
0
20
40
60
80
100
120
Time (min)

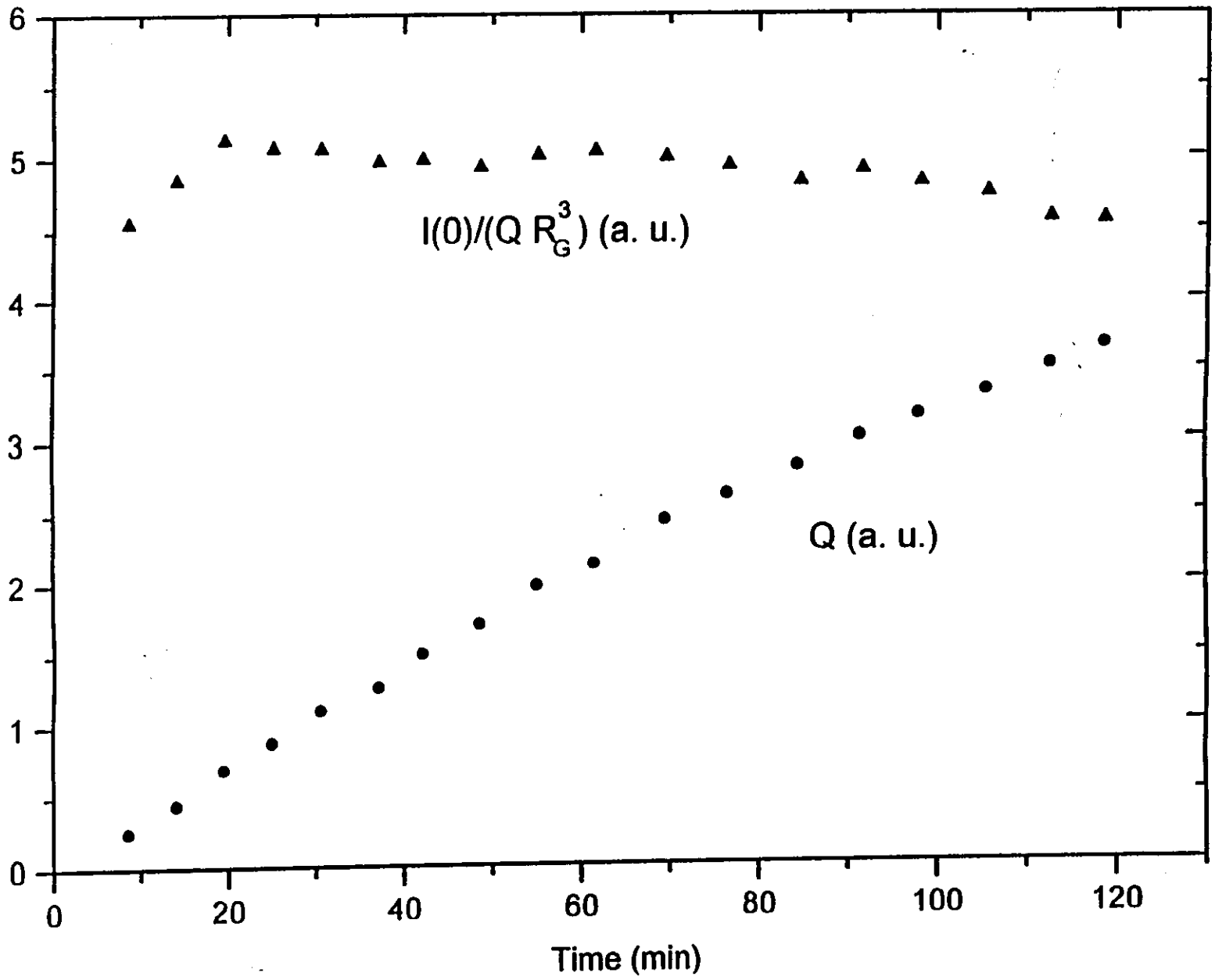
6
5
4
3
2
1
0
0
20
40
60
80
100
120
Time (min)
I(0)/(Q R$_G^3$) (a. u.)
Q (a. u.)

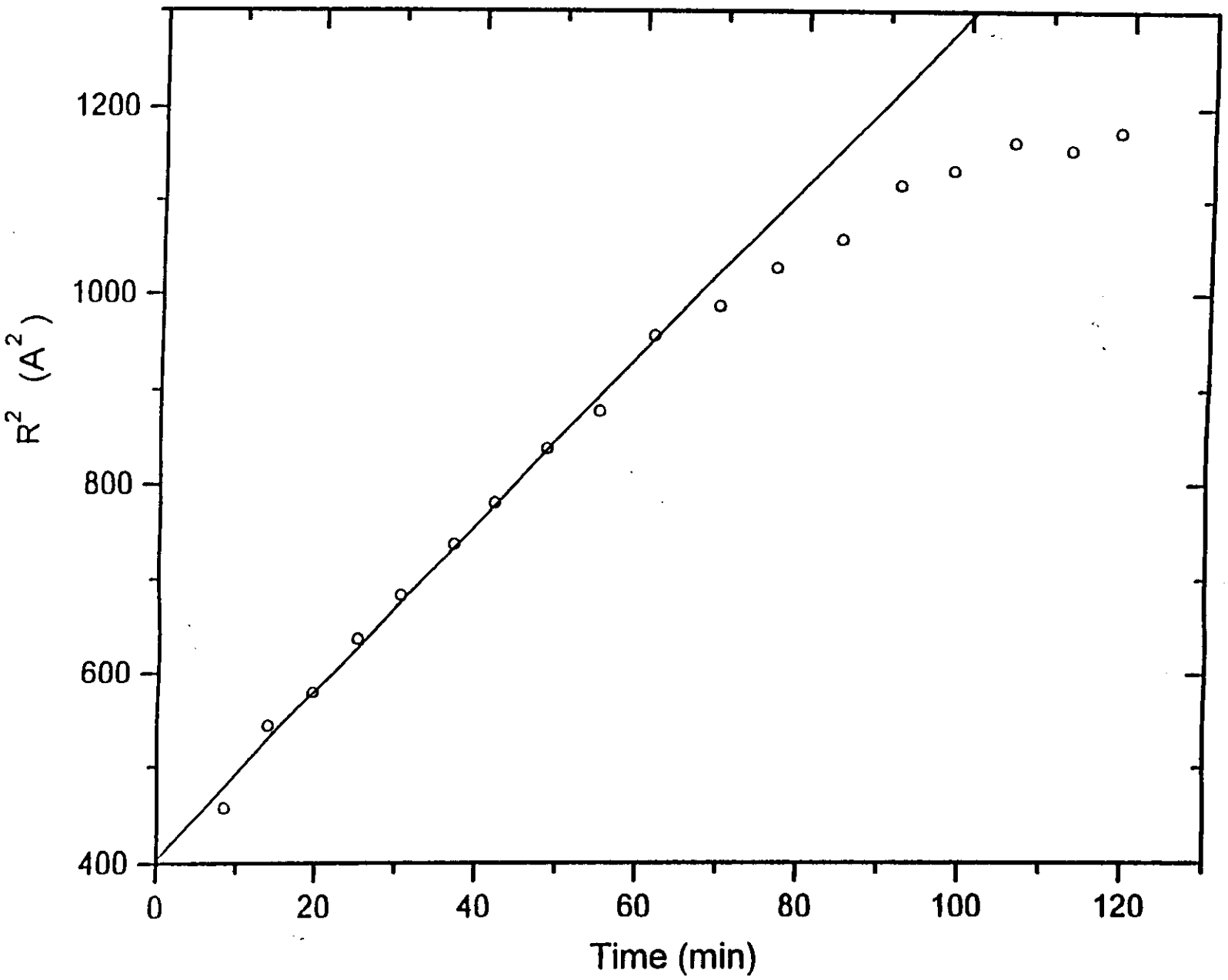
1200
1000
800
600
400
R^2 (A^2)
0
20
40
60
80
100
120
Time (min)